# Exploiting Seismic Waveforms of Ambient Noise and Earthquakes

Thesis by

Zhongwen Zhan

In Partial Fulfillment of the Requirements

for the Degree of

Doctor of Philosophy

California Institute of Technology

Pasadena, California

2014

(Defended September 16, 2013)

© 2014

Zhongwen Zhan

All Rights Reserved

*To my parents.*

# Acknowledgments

My graduate study in Seismolab has been a very pleasant journey. My advisor Don Helmberger has been extremely open and supportive about whatever I want to study and, most importantly, teaches me how to enjoy waveforms as a seismologist. Hiroo Kanamori is always available from Monday to Saturday (even Sunday) to discuss my latest results and shows me the big picture before I get lost in details. Mark Simons and Rob Clayton offer me a lot of insights in inverse problem and data processing. Victor Tsai has been fun to talk with on any topics, great to collaborate with, and is a good friend outside research. Jennifer Jackson has been a great academic advisor and extends my seismological view to other planets.

I owe special thanks to Sidao Ni, who brought me into the field of seismology, encouraged me to join seismolab to pursue my PhD, and gives constant support over the years.

I will definitely miss the coffee hour every morning joined by Hiroo, Tom, Mark, Rob, Mike, Pablo, Joann and many others. The coffee hour supplies not only a significant part of my breakfasts, but also a lot of new ideas and critical thinking. Over the years, I probably have learned more from the coffee hour than in classes.

Shixiong is a special concept for Chinese students. Daoyuan, Shengji, Risheng and Lijun (with his wife Yun) are great examples of shixiong for helping me in many aspects literally from the first day I arrived at Caltech. I also thank Dongzhou, Yihe (with her husband Peng), Xiangyan, Ting, Junle, Dunzhu, Yiran and Yingdi for fun activities in weekends and holidays.

South Mudd 358 has been a great office because of the wonderful officemates over the years. Ravi, Michelle, Dan have been really helpful, especially in my stressful first year. Dongzhou (also classmates and roommates), Yingdi, Chris, Rachel and Natalia are all very friendly and make the office a nice place to work in. I also thank members of the lunch group: Fan-chi, Victor, Yihe, Wenzheng, Wei, Bin, Tao, Wenbo, Zach, Asaf, Florent and many others. It is fun to chat about everyone's most preliminary results and many other interesting topics. The lunch group largely compensates the lack of variability in Chandler's food. I also would like to thank Seismolab staff members, who make the lab run well and our lives easier.

Finally, my deep thanks to my dear Qiong for her unselfish love and support, especially during the busy and stressful times. To my uncle Jie, for his encouragement over the years. To my warm and strong family, my father, mother and brother for their enduring love and support, and their persistence through the tough times.

# Abstract

In this thesis, I apply detailed waveform modeling to study noise correlations in different environments, and earthquake waveforms for source parameters and velocity structure.

Green's functions from ambient noise correlations have primarily been used for travel-time measurement. In Part I of this thesis, by detailed waveform modeling of noise correlation functions, I retrieve both surface waves and crustal body waves from noise, and use them in improving earthquake centroid locations and regional crustal structures. I also present examples in which the noise correlations do not yield Green's functions, yet the results are still interesting and useful after case-by-case analyses, including non-uniform distribution of noise sources, spurious velocity changes, and noise correlations on the Amery Ice Shelf.

In Part II of this thesis, I study teleseismic body waves of earthquakes for source parameters or near-source structure. With the dense modern global network and improved methodologies, I obtain high-resolution earthquake locations, focal mechanisms and rupture processes, which provide critical insights to earthquake faulting processes in shallow and deep parts of subduction zones. Waveform modeling of relatively simple subduction zone events also displays new constraints on the structure of subducted slabs.

In summary, behind my approaches to the relatively independent problems, the philosophy is to bring observational insights from seismic waveforms in critical and simple ways.

# Contents

# List of Figures

# List of Tables

# Chapter 1

# Introduction

THE DATA "MUST BE GREATLY AMPLIFIED AND STRENGTHENED."

—*Beno Gutenberg, Physics of the Earth's Interior, 1959*

Seismology is an observational science, based on data called seismograms. By reading seismograms, seismologists have obtained the most high-resolution pictures of the Earth interior and earthquakes. Availability of better data has always been the fundamental stimulator or driver of progresses in seismology. For example, in the early 1900's, seismograms (mostly travel times) from regional to global scales led to the discoveries of the Earth's primary structures, the Mohorovičić discontinuity, the liquid outer core, and the solid inner core. In 1960, newly-invented long-period seismometers by Hugo Benioff recorded the Great Chilean earthquake and provided the first definitive observation of the Earth's free oscillations.

From the 1960's, a series of progresses in computing theoretical seismograms made interpretation of detailed waveform shapes (wiggles) possible. After that, rapidly growing high-quality seismic waveforms have revealed complex structures of different scales (e.g. D'', ULVZ, ICB, transition zone, sharp super-plume), and kinematic ruptures of large earthquakes. Seismologists today are still working toward more effective and efficient use of seismic waveforms. In the meanwhile, just like many other science disciplines, seismology evolves into many high-specialized sub-disciplines. Even within the observational seismology, it becomes difficult to study different kinds of problems to fully appreciate the wide spectrum of seismic data.

Fortunately, the free atmosphere and great research resources in Caltech seismolab allow students like me to get involved in many different aspects of observational seismology, from local to global scales, from earthquake waveforms to ambient noise, from seismic structure to earthquake rupture. Through this process, I become more and more enthusiastic about seismic waveforms. I realize that every waveform is unique, and contains incredible amounts of information about the Earth. In this thesis, out of many interesting projects I have been involved in, I summarize seven different projects in which I have been the leading contributor. These seven studies are largely independent, but can be classified roughly by two groups: Part I, ambient noise correlations; and Part II, earthquake waveforms.

The idea of retrieving the Green's functions between stations by correlating ambient noise has been widely applied to studying Earth structure, earthquake locations, and monitoring velocity changes. Part I of this thesis includes four studies on ambient seismic noise.

(1) I relocate earthquake centroid by calibrating surface-wave path effects with noise cross-correlation functions. Test with the 2008 Chino Hills earthquake shows significant improvement in the centroid location and potential application for quick estimate of rupture directivity.

(2) While only fundamental mode surface waves emerge in most previous studies, I retrieve the Moho-reflected shear wave ($SmS$) and its multiples from noise cross-correlations at regional scales. I also demonstrate how an uneven distribution of noise sources can mask weaker body-wave phases.

(3) Ambient noise cross-correlations are now being used to detect temporal variations of seismic velocity, which are typically on the order of 0.1%. At this small level, temporal variations in the properties of noise sources can cause apparent velocity changes. I demonstrate that temporal variability of noise frequency content can

cause spurious velocity changes when noise correlations are used to monitor velocity changes.

(4) I apply the noise cross- and auto-correlation methods to the Amery Ice Shelf. I find that the noise field on the ice shelf is dominated by energy trapped in a low velocity waveguide caused by the water layer below the ice. Within this interpretation, I obtain independent estimates of the water-column thickness and the structure of the firn layer.

Part II of this thesis presents three studies on earthquake waveforms.

(1) The 2011 Mw 9.1 Tohoku-Oki earthquake had unusually large slip concentrated in a relatively small region. Detailed analysis of earthquakes in the Tohoku-Oki region reveals steeper earthquake dip angles than the previously imaged plate interface. I explain this discrepancy as evidence for a complex plate interface.

(2) The physical mechanism of deep earthquakes remains enigmatic. I develop and apply a full-waveform sub-event method to the two largest deep earthquakes, the recent Great 2013 Sea of Okhotsk earthquake (M8.3) and the Great 1994 Bolivia earthquake (M8.3). Both earthquakes display complex rupture histories, and significantly different rupture speeds, possibly related to the slab thermal states.

(3) I observe and model teleseismic waveforms from earthquakes in the Kuril subduction zone with strong broadening caused by the subducted slab. I obtain a ~5% velocity perturbation in the slab, significantly higher than most tomographic models.

# Part I

# Ambient Seismic Noise

# Chapter 2

# Earthquake Centroid Locations Using Calibration from Ambient Seismic Noise

This chapter has been published as:

Zhan, Z., Wei, S., Ni, S., and Helmberger, D. (2011), Earthquake centroid locations using calibration from ambient seismic noise, Bulletin of the Seismological Society of America, Volume 101, Number 3, Pages 1438-1445.

## 2.1 Abstract

Earthquakes occur in complex geology, making it difficult to determine their source parameters and locations because of uncertainty in path effects. We can avoid some of these problems by applying the cut-and-paste (CAP) method, which allows for timing shifts between phases, assuming a 1D model, and determines source parameters. If the travel times or lags of the phases due to path effects are known relative to a reference model, we can locate the events' centroid with surface waves without knowledge of the 3D velocity structure. Here, we use ambient seismic noise for such a calibration. We cross correlate the seismic stations near the earthquake with stations 100–300 km away to obtain the 10–100-s surface wave Green's functions. The new method is tested in Southern California to locate the 2008 Chino Hills earthquake, which proves

consistent with the epicenter location from $P$ waves. It appears possible to use the location offset between the high-frequency $P$-wave onset relative to the centroid to provide a fast estimate of directivity.

## 2.2 Introduction

The characterization of earthquakes in near real time is one of the major themes in the seismic monitoring community. Another is addressing events with sparse data that commonly occur in remote areas or historical events that occurred before dense instrumentation. All of these issues can benefit from using more of the regional records beyond the initial $P$ waves. The objective of this report is to explore the use of surface waves to aid in source estimation, which requires crustal velocity models. Several new methods have been developed to retrieve such structures based on the cross correlation of ambient seismic noise (station-to-station) and conventional (source-to-station) inversions (Tape et al., 2010). The latter approach provides the most broadband results, containing both body-wave phases and surface waves. Generally, the travel times of $P$ waves are used to locate events because the arrivals display little dispersion, and velocity models can be calibrated in timing by artificial sources with known location and origin time. Surface waves are more difficult to calibrate in that they involve earthquakes. In this case, one must separate the source excitation from the propagation or path effects.

The first approach, station-to-station, does not have this problem because we generally know where the stations are located, and ambient seismic noise (ASN) can be used to calibrate the timing of the surface waves (Shapiro et al., 2005; Ma et al., 2008). Thus, we propose locating earthquakes with the help of surface waves where the trade-offs issue just mentioned has been eliminated. Because locating earthquakes in near real time is the most useful, we will apply the cut-and-paste (CAP) method

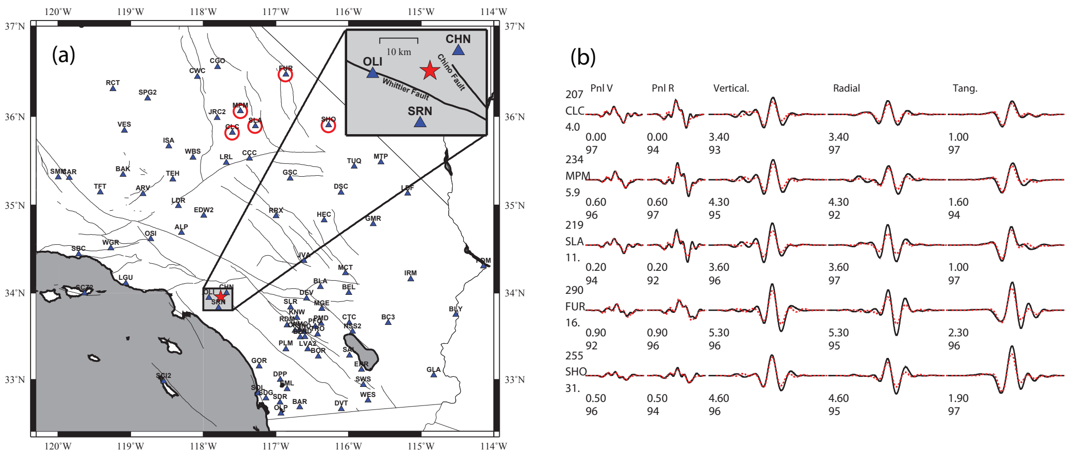


Figure 2.1: (a) Locations of the 29, July 2008 Chino Hills earthquake (star) and stations (triangles) used in this study, along with (b) a sample of CAP inversions. The five stations used in this sample CAP inversion are highlighted by circles in (a). In (b), the station names are expressed in three letters with their distances in kilometers above the letters. The numbers below the letters state the azimuth in degrees. Results in matching *Pnl* and surface waves are given on the right with data in solid lines and fits in dashed lines. The numbers below the segments state the timing shifts and the cross correlations. Positive time shifts indicate that the synthetic needs to be shifted back or that the data arrives late. Note that the Rayleigh wave is 4.6 s late, while the Love wave is 1.9 s for station SHO.

to estimate the depth and mechanism. This method fits the Rayleigh and Love wave segments by allowing travel-time shifts relative to a reference model. If these shifts can be determined by previous events, the surface waves can be used in combination with body waves to locate events with sparse networks (Zhu et al., 2006; Tan et al., 2006). Here, we will use ASN for the surface-wave calibration, and the well-calibrated TriNet array for testing, see Figure 2.1. In particular, we will readdress the well-studied Chino Hills event (Hauksson et al., 2008). In short, we will use ASN to calibrate paths connecting the Chino Hills event with the TriNet array as a proof-of-concept test.

## 2.3 Data Processing and Analysis

This earthquake was widely felt and reported by Hauksson et al. (2008). The CAP technique has been used to estimate the focal mechanism and depth (Zhu and Helmberger, 1996). The method fits the Rayleigh and Love wave segments by allowing travel-time shifts relative to a 1D reference model with some example waveform fits given in Figure 2.1b. The delays of the surface waves displayed here can be predicted from prior events to within a second (Tan et al., 2010) if they have high cross correlations (cc>0.85). A small number of stations can then be used to produce a relatively good mechanism and location using complete records, as demonstrated in Tan et al. (2006). Thus, the Program for Array Seismic Studies of the Continental Lithosphere (PASSCAL) deployments can be used to calibrate permanent stations and maintain accuracy (Tan et al., 2006). In short, the key information is how well we can predict these path corrections with ASN. The 5–100-s period surface waves are well recorded by the TriNet array. To calibrate the travel times of these surface waves, the three closest stations (CHN, OLI, and SRN) were chosen as the virtual sources in noise cross correlation (Figure 2.1).

These three stations are cross correlated with the TriNet stations with epicentral distances from 100 km to 350 km, which recorded clear 5–100-s period surface waves. The 5–100-s surface wave empirical Green's functions have been regularly retrieved using ambient seismic noise cross correlation across the United States (Bensen et al., 2008). Our cross-correlation procedure is similar to that given by Bensen et al. (2007) and Lin et al. (2008). Twelve months of continuous long-period records (LHE, LHN, LHZ) in 2006 are downloaded from Southern California Earthquake Center's (SCEC) Seismogram Transfer Program (STP) and cut into daily segments. After removal of mean, trend, and instrumental response, the seismograms are bandpass filtered between 5 s and 100 s. To remove the effect of earthquakes, we first filter the original seismograms between 15 s and 50 s to emphasize the surface waves of earthquakes, and then calculate their envelope functions. The inverse of these smoothed envelope functions are used to weight the corresponding seismograms between 5 s and 100 s trace by trace. This procedure has been proven to be effective in suppressing earthquake signals (Bensen et al., 2007). Cross correlations between all three components (east, north, and vertical, ENZ-ENZ) are then computed over daily intervals and stacked. To separate the Rayleigh and Love waves, the ENZ-ENZ noise cross-correlation functions (NCFs) are rotated to give the radial-transverse-vertical (RTZ-RTZ) components (Lin et al., 2008). We also test rotating seismograms to RTZ components before cross correlation and find that the NCFs look almost identical. The positive and negative sides of the rotated NCFs are folded and summed to give the final NCFs. The resulting vertical-vertical (Z-Z) and transverse-transverse (T-T) NCFs are used for Rayleigh and Love waves, respectively.

The 10–100-s passband proved the most useful, so we will begin with an example of Rayleigh wave and Love wave comparison, Figure 2.2a. As the focal mechanism and depth affect phases of surface waves, it is not appropriate to compare earthquake surface waves and NCFs directly. Instead, the time differences are measured by cross correlating the earthquake records or the NCFs (Figure 2.2a, solid lines) with 1D synthetics (Figure 2.2a, dashed lines) in time windows of 60 s around the predicted surface wave travel times. We use the SCEC epicenter location of the earthquake and focal mechanism and depth from Hauksson et al. (2008) to calculate the 1D synthetics, assuming the standard SoCal model (Dreger and Helmberger, 1993). For NCFs, a vertical/tangential point force is placed at the virtual sources on the free surface to calculate the Rayleigh/Love wave synthetics. The numbers above and below the seismograms are the time shifts in seconds and cross-correlation coefficients. Figure 2.2b is a schematic to show the meaning and relations of these time shifts. The true centroid location of the earthquake is the star A, initial estimation of the location

(SCEC epicenter in this example) is A', and the seismograms are recorded at station C (SHO in this example). The time shifts from the earthquake are attributed to two factors: (1) error in epicentral distance AC-A'C due to location error and (2) the velocity anomaly between the earthquake A and station C. To obtain a better centroid location, we need to calibrate the path effect. Station B (CHN in this example) is close to the earthquake, and the NCFs between B and C are the empirical Green's functions between B and C with B as a virtual source. Because BC is close to AC, the NCFs will sample a similar velocity anomaly as AC; hence, this provides a calibration of the path effect.

The results for the full network are presented in Figure 2.8 for Rayleigh waves and Figure 2.9 for Love waves (both figures are available in supplementary material). The corresponding (5–10 s) results are given in Figures 2.10 and Figure 2.11. To be useful in locating, these figures require a high degree of fit, maximum cross correlation between data/NCF and synthetic cc>0.8. We summarize these fits in a bar diagram, Figure 2.12. The percentages of NCFs with cc>0.8 at 10–100 s is 88% for both Rayleigh and Love waves, whereas they drop to 47% and 36% in the 5–10-s band. Apparently, the surface geology is too complex at these shorter wavelengths to obtain accurate delays. A more complete comparison of matching the earthquake data is presented in Figure 2.13.

A particularly convenient way to view the delays and cc's is in the form of spider diagrams as presented in Figure 2.3 and Figure 2.4. The overall high similarity among the spider diagrams of the three virtual sources, especially for the stations with high cross-correlation coefficients, indicates that the NCFs with the three different virtual sources are sampling similar velocity structures and hence provide a stable calibration of the path effect. The similarity between earthquake and noise spider diagrams indicates that the SCEC epicenter is quite close to the true centroid location and that the time shifts for the earthquake are dominated by the path effects. The adjustment

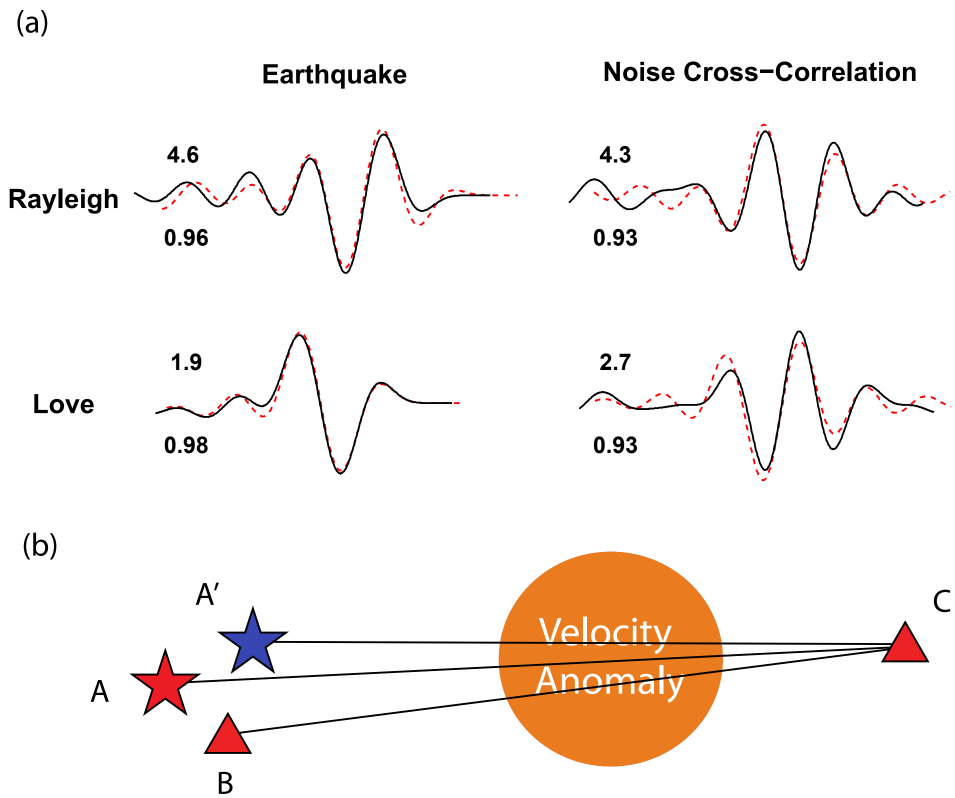


Figure 2.2: Illustration of locating an earthquake with noise cross correlation as path calibration. (a) Observed travel time differences with respect to the 1D SoCal model for both Rayleigh waves (upper row) and Love waves (lower row) of the Chino Hills earthquake recorded at SHO (left column) and the noise cross-correlation functions (NCFs) between CHN and SHO (right column). Dash lines are the synthetic seismograms from 1D SoCal model. The numbers above and below the seismograms are the time shifts in seconds and cross-correlation coefficients. The durations of all the seismograms are 60 s. (b) The earthquake location is given by the star A with an estimate at the star A'. Station B (CHN in this example) is close to the earthquake, and the NCFs between B and C are the empirical Green's functions between B and C with B as a virtual source. Because BC is close to AC, the NCFs will sample the same velocity anomaly as AC, hence providing a calibration of the path effect.

of the centroid location with respect to the SCEC epicenter will be based on the small differences between earthquake and noise spider diagrams.

Before relocating the earthquake, we test the true accuracy of the method by locating a virtual source station, SRN, as displayed in Figure 2.5. When locating with the 1D SoCal model, time shifts from SRN (Figure 2.5, open squares in the left column, upper and lower rows for Rayleigh and Love waves, respectively) will be entirely attributed to the error of the source location used in calculating the 1D synthetics, i.e., the true location of SRN. An iterative least-square algorithm is used to solve the inverse problem. The result converges quickly after one or two iterations. The residual time shifts are shown as open circles in the left column of Figure 2.5. The resulting location is shown in Figure 2.6 with a 95% confidence limit, offset approximately 6 km to the south-southeast (SSE) of the true location. If the calibration from OLI is used, a large part of the time shifts due to path effect is removed, as shown in the right column of Figure 2.5 as open squares. The greatly reduced variance of the time shifts indicates that the location used in calculating 1D synthetics (true SRN location) is a good estimation. This is confirmed by the resulting location shown in Figure 2.6, which is only approximately 1 km to the southeast of the true location. Replacement of the L2 norm in the inverse algorithm with an L1 norm, which is less sensitive to outlier measurements (e.g., Shearer, 1997), does not make any obvious difference in this example. A similar analysis for the other stations is given in Figures 2.14 and Figure 2.15 and is summarized in Figure 2.6 with all the results. The 1D model locations are systematically offset to the south by about 6 km due to overall slower velocity structure to the north relative to the 1D SoCal model. The large 95% confidence limits of 1D locations are caused by the complicated velocity heterogeneities. After the noise calibration, the path effect is largely removed, and the resulting locations are much closer to the true locations with much smaller 95% confidence limits.

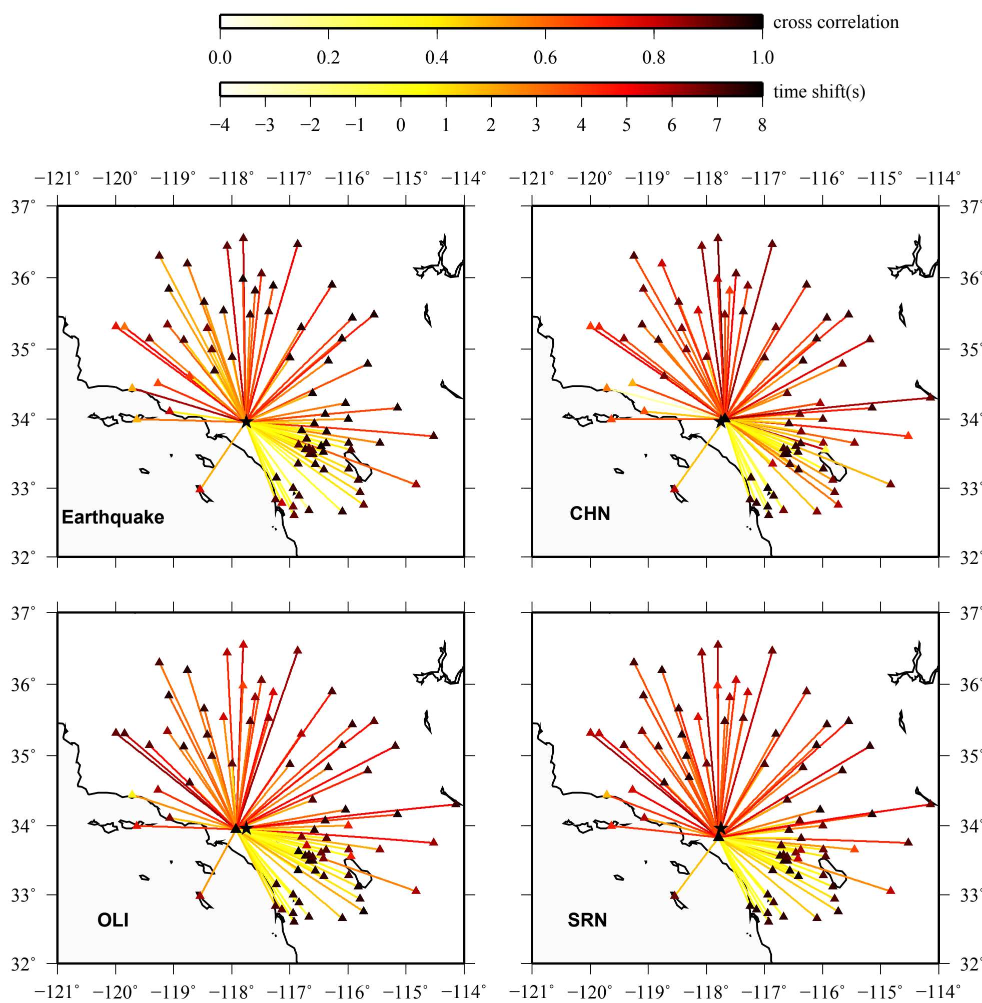


Figure 2.3: Spider diagrams of the Rayleigh wave time shifts with respect to the 1D SoCal model for the Chino Hills earthquake (star in the center) and three closest stations CHN, OLI, and SRN (triangles) as virtual sources. The colors of the paths indicate the time shifts, and the station colors indicate the cross-correlation coefficients.

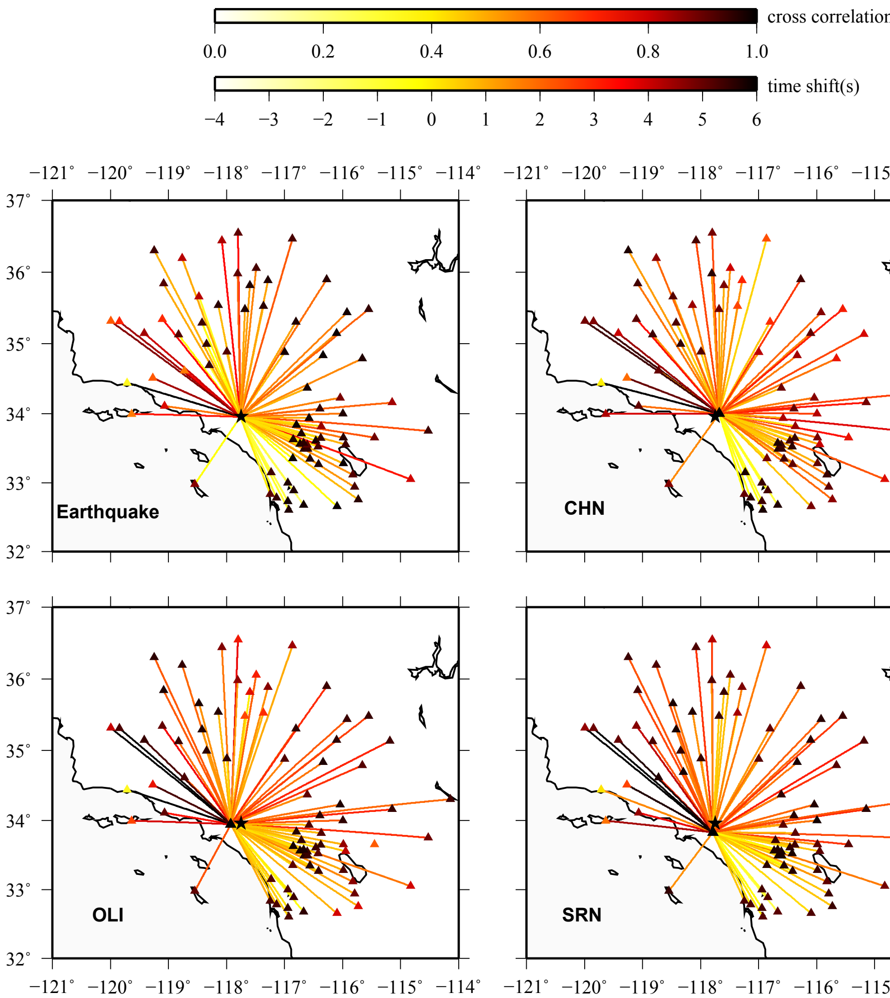


Figure 2.4: Similar to Figure 2.3, but for Love waves.

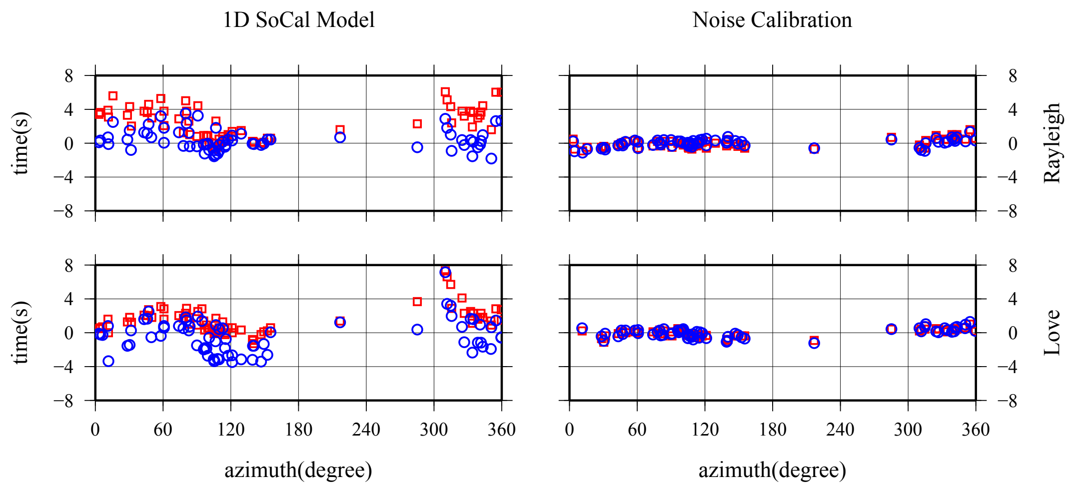


Figure 2.5: Location of virtual source station SRN based on the 1D SoCal model (left) compared to using station corrections (calibration) from OLI (right). The squares refer to the delays (timing offsets) measured from the cross correlations of NCFs taken from Figure 2.3 and Figure 2.4 with the 1D Green's functions, Rayleigh (top) with Love (bottom). The circles are residual time shifts after least-square relocation. The plots on the right use corrections obtained from station OLI. The resulting locations for virtual source SRN are shown in Figure 2.6.

The two large stars in Figure 2.6 are the epicenters of the earthquake from the SCEC catalog and the earthquake given by Hauksson et al. (2008), labeled EH. Small stars with ellipses are the relocated earthquake centroid locations with the 1D model or noise calibrations and their 95% confidence limits. Similar to the 1D locations of virtual sources, the 1D location of the earthquake is also largely offset to the south and has a large confidence limit. After the noise calibrations from three virtual sources (CHN, OLI, and SRN) as displayed in Figure 2.7, the resulting centroid locations are offset 1–3 km to the west of the estimated epicenters, which appear to be well resolved. Thus, the difference between the epicenter location and centroid location suggests rupture towards the west. This type of analysis is expected to show larger source location differences with larger magnitudes and can be used to provide quick estimates of directivity. The two arrows perpendicular to the Whittier fault and the Chino fault show the fault dips, although these dips are not well known (Hauksson

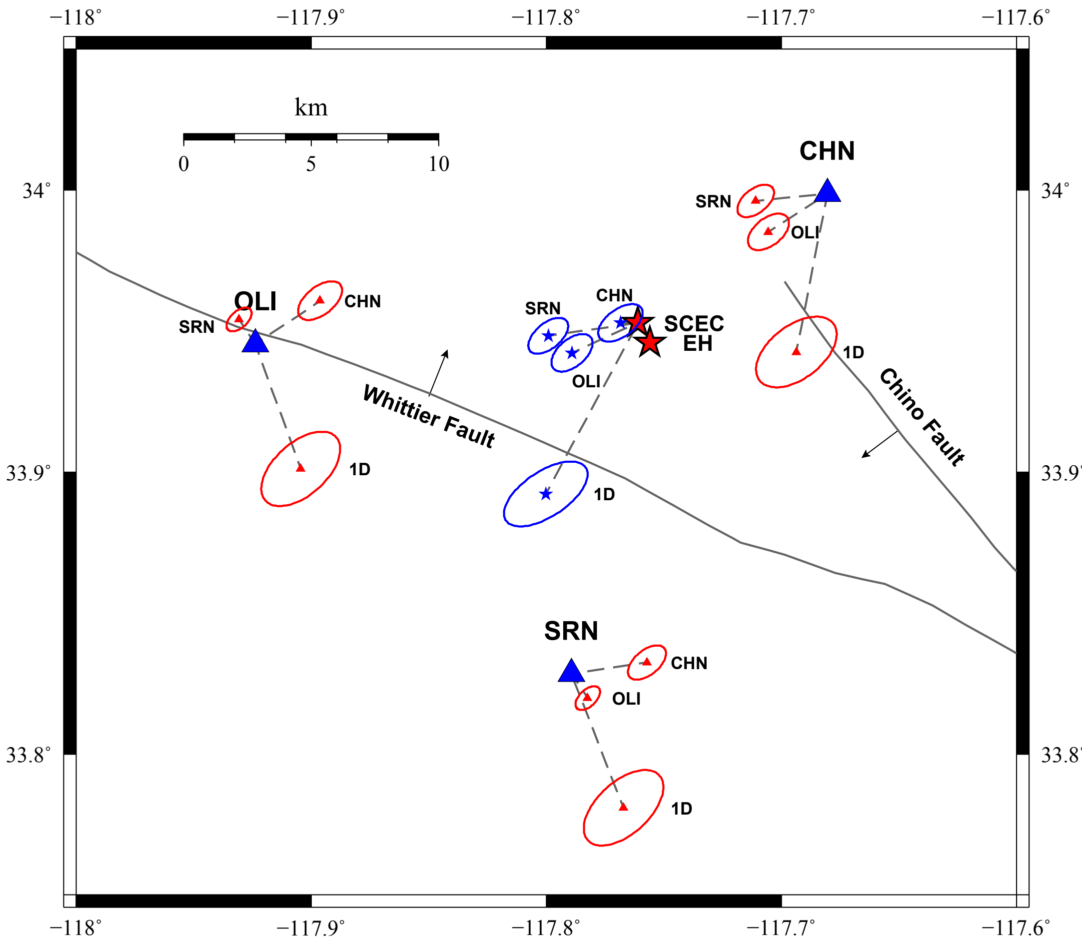


Figure 2.6: Estimated locations of the virtual sources and the earthquake with 1D SoCal model or noise calibrations. Large triangles are the true locations of the three virtual source stations CHN, OLI, and SRN. The dashed lines connecting small triangles with ellipses are the relocated virtual sources with their 95% confidence limits. Two large stars, labeled as SCEC and EH, are epicenter locations from the SCEC catalog and Egill Hauksson's catalog (Hauksson et al., 2008). The dashed lines connecting small stars with ellipses are the relocated earthquake centroid locations with their 95% confidence limits, using the 1D model, or noise calibrations from CHN, OLI, and SRN, respectively.

et al., 2008).

## 2.4 Discussion and Conclusions

Passive imaging with earthquake coda waves and ambient seismic noise has been primarily used to study structure, but more recently has been used for many other applications. A common use is to measure dispersion between two points as done with earthquake data (Campillo and Paul, 2003), or this technique can be used in combination with the earthquake surface wave technique (Lin et al., 2008). Here, we are interested in shorter paths where surface waves are less dispersive and dominated by the Airy phase. Its overall period is controlled by the surface layering and its timing by the $S$ velocity in the source layer (Song et al., 1996). Thus, they become useful for locating events at local and near-regional distances. However, they have disadvantages relative to the $P$ wave in that they are at longer periods and are influenced by the radiation pattern. Because $P$ waves can be observed at high frequencies, they are easy to measure and also easily calibrated from explosion data. Numerous calibration explosions have been conducted globally for this purpose, and thus, this is a well-developed method for refining source locations.

In contrast, local surface waves must be addressed in terms of mechanism and location together because small changes in mechanism can change delay times (Wei et al., 2012), and thereby influence location. However, the NCFs have well-known source terms and locations and, therefore, are independent of $P$-wave calibration and provide unique information about travel times.

Because the source mechanism and surface wave delays are closely related, it becomes particularly advantageous to use this information together by coupling the CAP method and the location as discussed in the previous paragraph. However, it does require a local 1D model or regional model that is compatible with observed

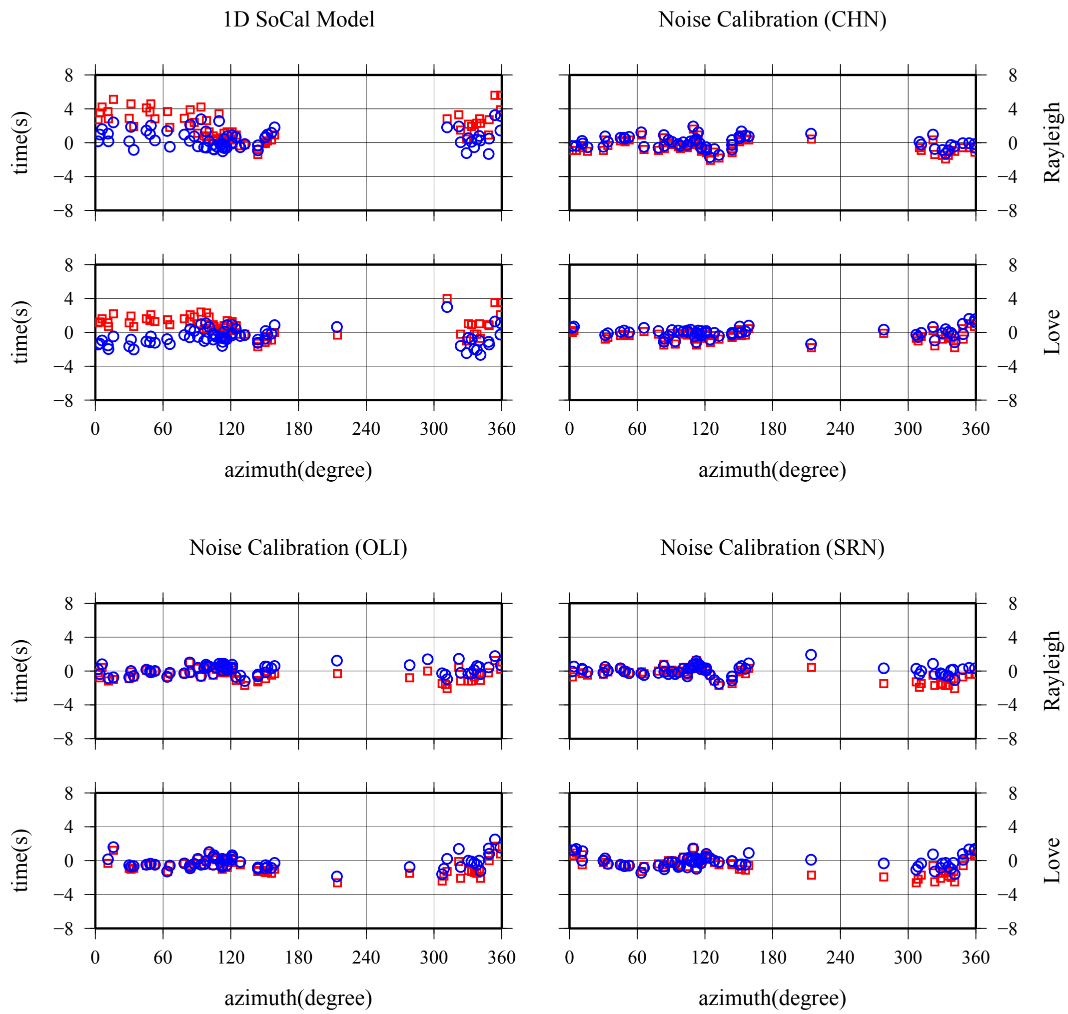


Figure 2.7: This figure is similar to Figure 2.5, but locates the Chino Hills earthquake with the 1D SoCal model or noise calibration from three virtual sources CHN, OLI, and SRN. In the upper left panel, squares refer to time delays measured by cross correlating earthquake records with synthetic seismograms from the 1D SoCal model (earthquake cases in Figure 2.3 and Figure 2.4). Circles are the residual time delays after least-square relocation of the earthquake centroid. The other three panels are similar, except that travel-time calibrations from the three virtual sources, CHN, OLI, and SRN are used, respectively, in each of the three panels. The resulting centroid locations with confidence limits are displayed in Figure 2.6 (small stars with ellipses).

airy phases. Fortunately, at 10 s, this restriction is not great in that simple models consisting of a soft surface layer, 2–4 km, and a uniform crust prove effective (e.g., Tan et al. (2010) for Southern California, Zhu et al. (2006) for Tibet, and Ni and Helmberger (2010) for Korea).

In summary, we have introduced a new method for locating earthquakes by extending the CAP methodology using path calibrations from ambient seismic noise. Because the CAP method proves effective in determining mechanisms without a detailed crustal structure, it is particularly useful in combination with NCFs in studying local seismicity from PASSCAL experiments and USArray. Such applications will be addressed in future efforts.

## Acknowledgments

Continuous seismic record and earthquake seismograms used in this study were obtained from the IRIS Data Management Center or Southern California Earthquake Center. Some plots were made using the Generic Mapping Tools version 4.2.0. Two anonymous reviewers and the editor provided helpful comments to improve the article. This work was supported by USGS NEHRP grant G10AP00048, NSFC 40821160549, CAS KZCX2-YW-116-1, and CEA program 200808078, 200708035.

## References

Bensen, G. D., Ritzwoller, M. H., Barmin, M. P., Levshin, A. L., Lin, F., Moschetti, M. P., Shapiro, N. M., and Yang, Y. (2007). Processing seismic ambient noise data to obtain reliable broad-band surface wave dispersion measurements, Geophys. J. Int. 169, 1239-1260.

Bensen, G. D., Ritzwoller, M. H., and Shapiro, N. M. (2008). Broad-band ambient noise surface wave tomography across the United States, J. Geophys. Res. 113, B05306.

Campillo, M., and Paul, A. (2003). Long range correlations in the seismic coda, Science 299, 547-549.

Dreger, D. S., and Helmberger, D. V. (1993). Determination of source parameters at regional distances with three-component sparse network data, J. Geophys. Res. 98, no. B5, 8107-8125.

Hauksson, E., Felzer, K., Given, D., Giveon, M., Hough, S., Hutton, K., Kanamori, H., Sevilgen, V., Wei, S., and Yong, A. (2008). Preliminary report on the 29 July 2008 Mw 5.4 Chino Hills, eastern Los Angeles basin, California, earthquake sequence, Seismol. Res. Lett. 79, 838-849.

Lin, F. C., Moschetti, M. P., and Ritzwoller, M. H. (2008). Surface wave tomography of the western United States from ambient seismic noise: Rayleigh and Love wave phase velocity maps, Geophys. J. Int. 173, 281-298.

Ma, S., Prieto, G. A., and Beroza, G. C. (2008). Testing community velocity models for southern California using the ambient seismic field, Bull. Seismol. Soc. Am. 98, 2694-2714.

Ni, S., Helmberger, D. V., and Pitarka, A. (2010). Rapid source estimation from global calibrated paths, Seismol. Res. Lett., 81, no. 3, 498-504.

Shapiro, N. M., Campillo, M., Stehly, L., and Ritzwoller, M. H. (2005). High-resolution surface-wave tomography from ambient seismic noise, Science 307, 1615-1618.

Shearer, P. M. (1997). Improving local earthquake locations using the L1 norm and waveform cross correlation: Application to the Whittier Narrows, California, aftershock sequence, J. Geophys. Res. 102, B4, 8269-8283.

Song, X. J., Helmberger, D. V., and Zhao, L. (1996). Broadband modeling of regional seismograms: The Basin and Range crustal structure, Geophys. J. Int. 125, 15-29.

Tan, Y., Song, A., Wei, S., and Helmberger, D. V. (2010). Surface wave path corrections and source inversions in southern California, Bull. Seismol. Soc. Am. 100, no. 6, 2891-2904.

Tan, Y., Zhu, L., Helmberger, D. V., and Saikia, C. (2006). Locating and modeling regional earthquakes with two stations, J. Geophys. Res. 111, B1, 1306-1320.

Tape, C., Liu, Q., Maggi, A., and Tromp, J. (2010). Seismic tomography of the southern California crust based on spectral-element and adjoint methods, Geophys. J. Int. 180, 433-462.

Wei, S., Z. Zhan, Y. Tan, S. Ni, and D. Helmberger (2012), Locating earthquakes with surface waves and centroid moment tensor estimation, J. Geophys. Res., 117, B04309.

Zhu, L., Tan, Y., Helmberger, D. V., and Saikia, C. (2006). Calibration of the Tibetan Plateau using regional seismic waveforms, Pure Appl. Geophys. doi: 10.1007/s00024-006-0073-7, 1193-1213.

## Supplementary figures: Cross-correlation, waveform comparisons, and source locations with 1D model and noise calibration

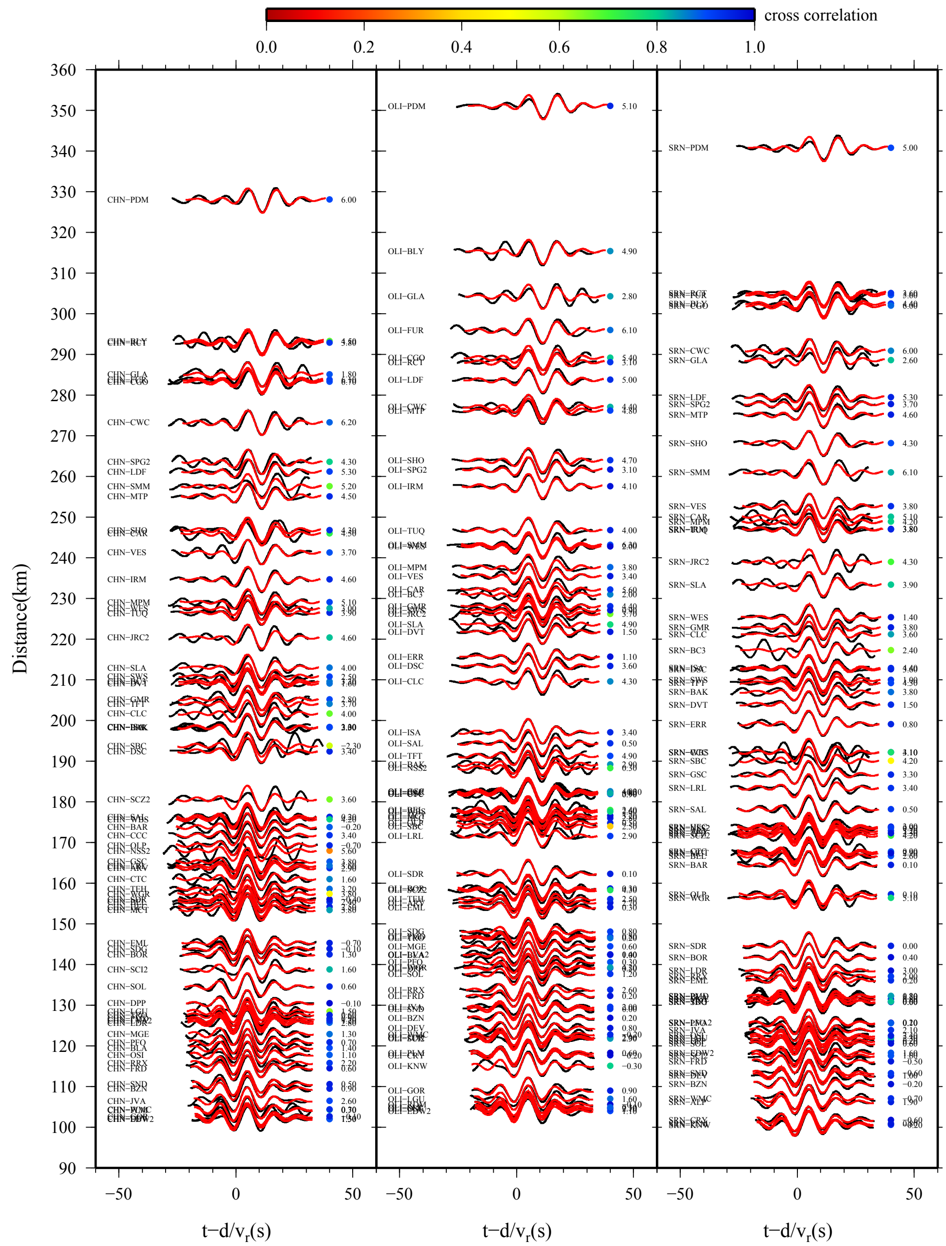


Figure 2.8: Measurement of time shifts between 10-100s Z-Z NCFs (Rayleigh waves, black lines) and 1D synthetic seismograms (red lines) by cross-correlation. The station pairs are classified by their source stations (CHN, OLI or SRN) and displayed in three columns. The names of stations for each NCF are shown to the left of the seismograms. The maximum cross-correlation coefficient (colored dot) and the corresponding time shift are shown on the right. A reduction velocity of Vr=3.44km/s is used that best aligns the synthetics.

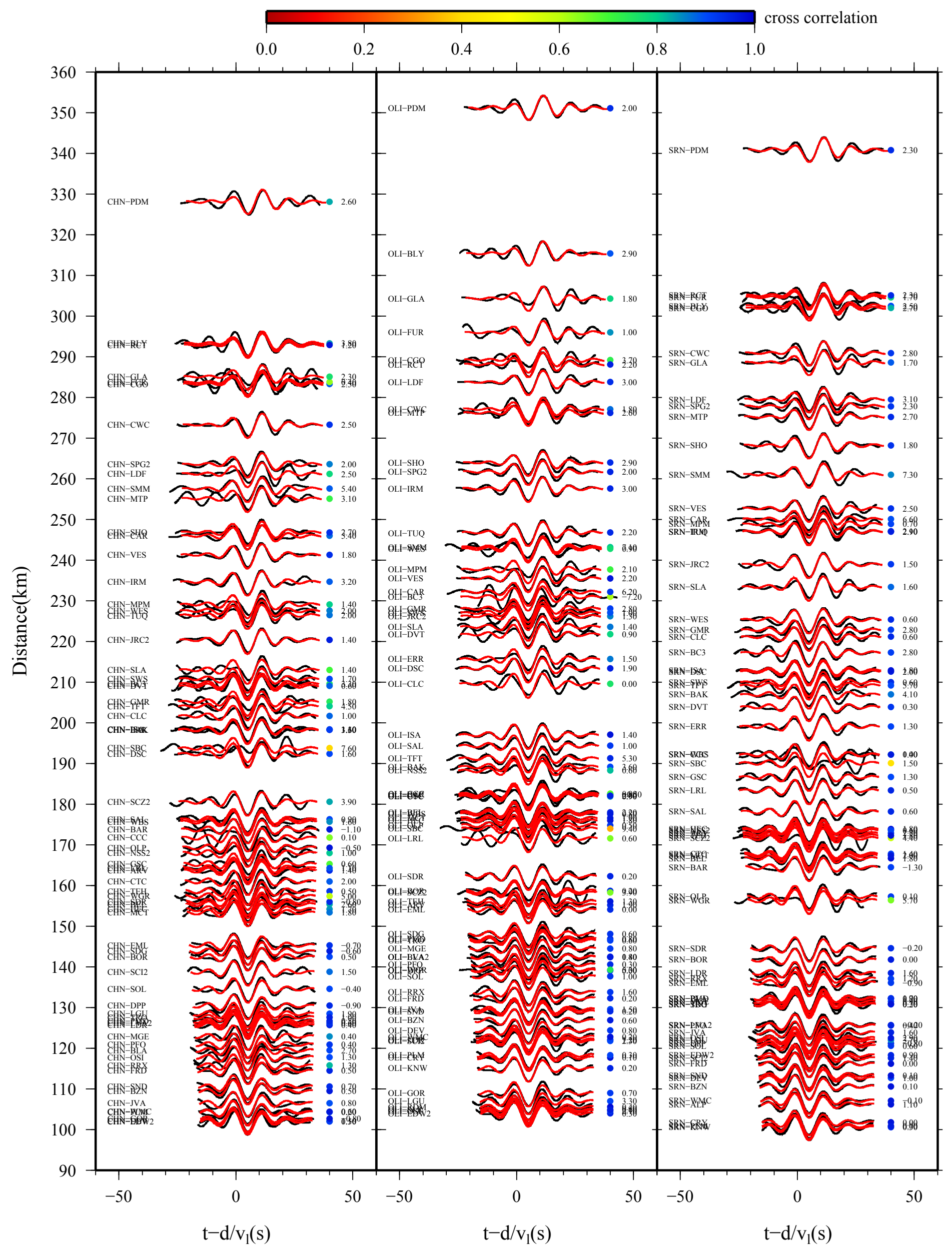


Figure 2.9: The same as Figure 2.8, but for 10-100s T-T NCFs (Love waves). A reduction velocity of Vl=3.73km/s is used.

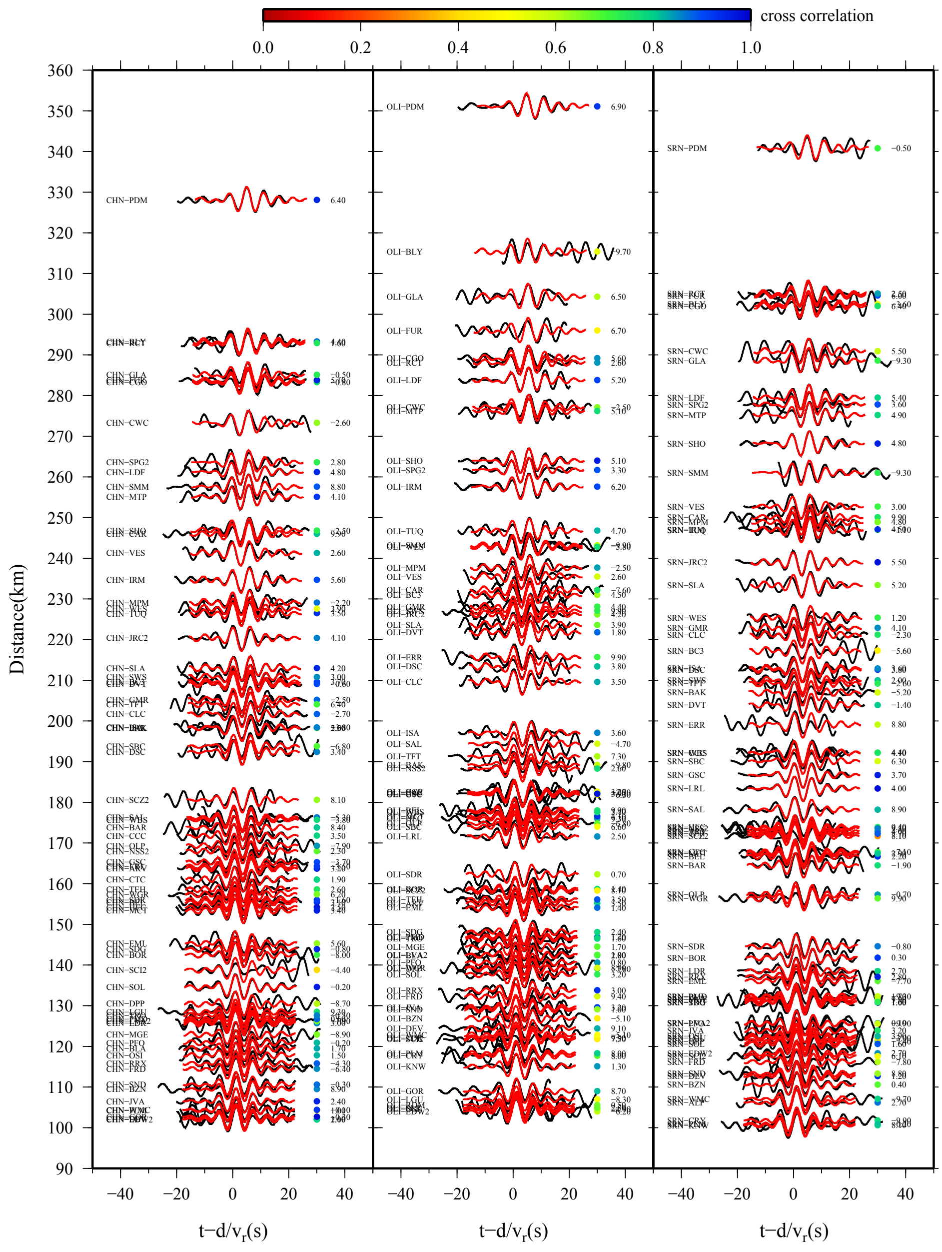


Figure 2.10: The same as Figure 2.8, but for 5-10s Z-Z NCFs (Rayleigh waves). A reduction velocity of Vr=3.1km/s is used since the shallower crust is involved.

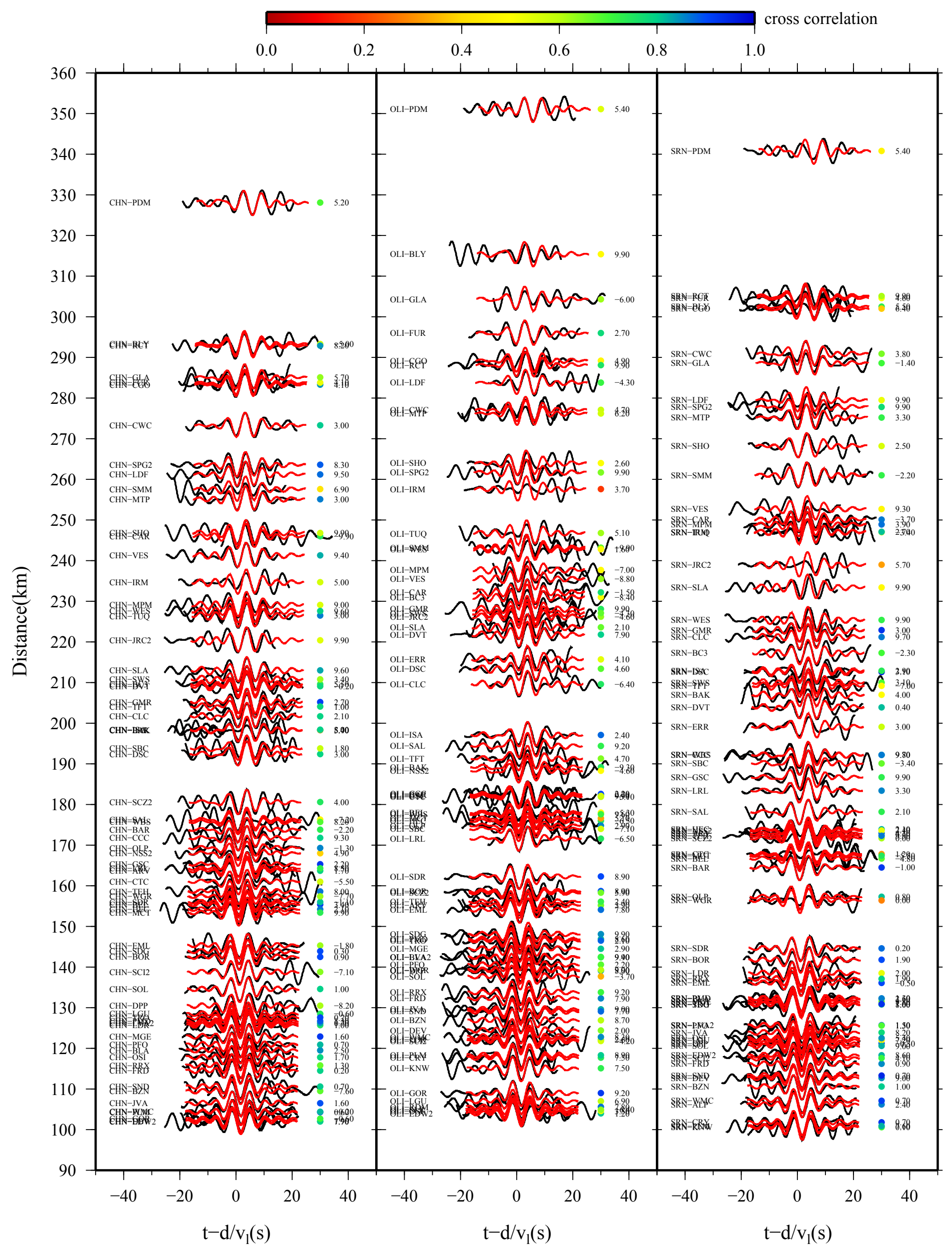


Figure 2.11: The same as Figure 2.8, but for 5-10s T-T NCFs (Love waves). A reduction velocity of Vl=3.4km/s was used in the case.

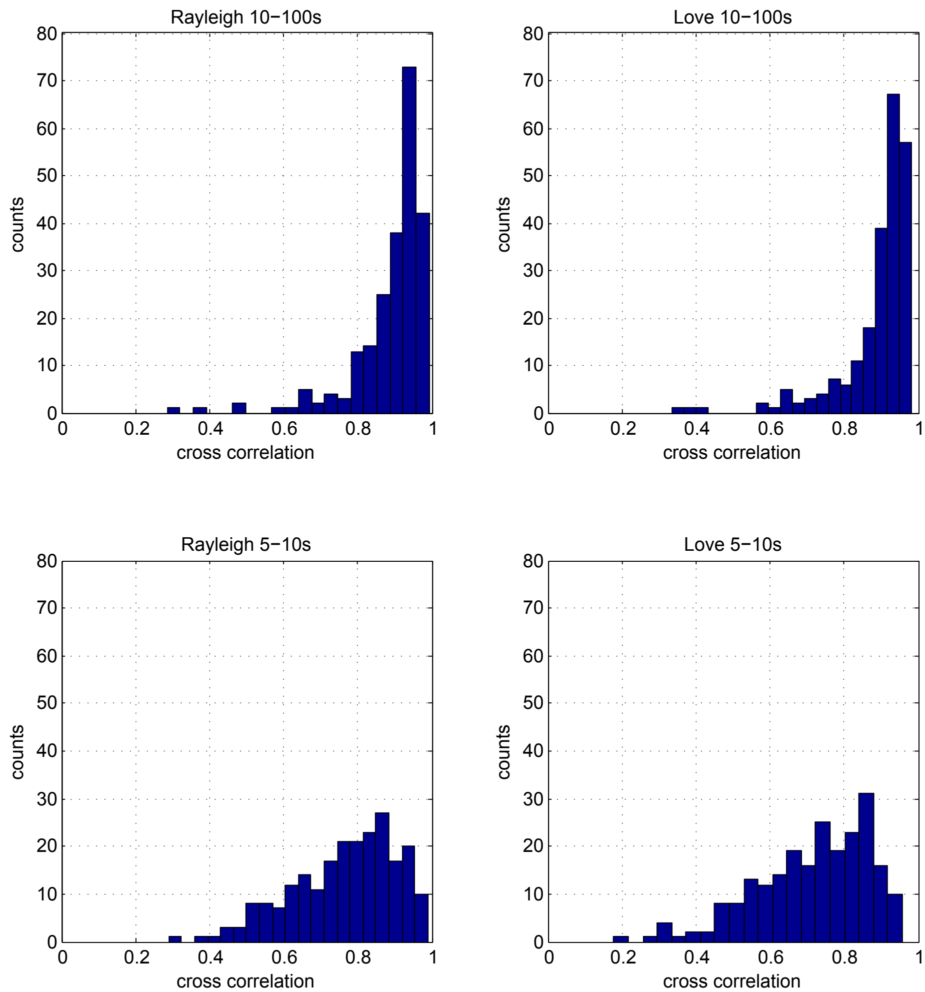


Figure 2.12: Histograms of the cross correlation coefficients between NCFs and 1D synthetic seismograms, for 5-10s, 10-100s Rayleigh and Love waves. The percentages of NCFs with cross correlation coefficients larger than 0.8 are 88% for 10-100s Rayleigh and Love waves, but 47% and 36% for 5-10s Rayleigh and Love waves, respectively.

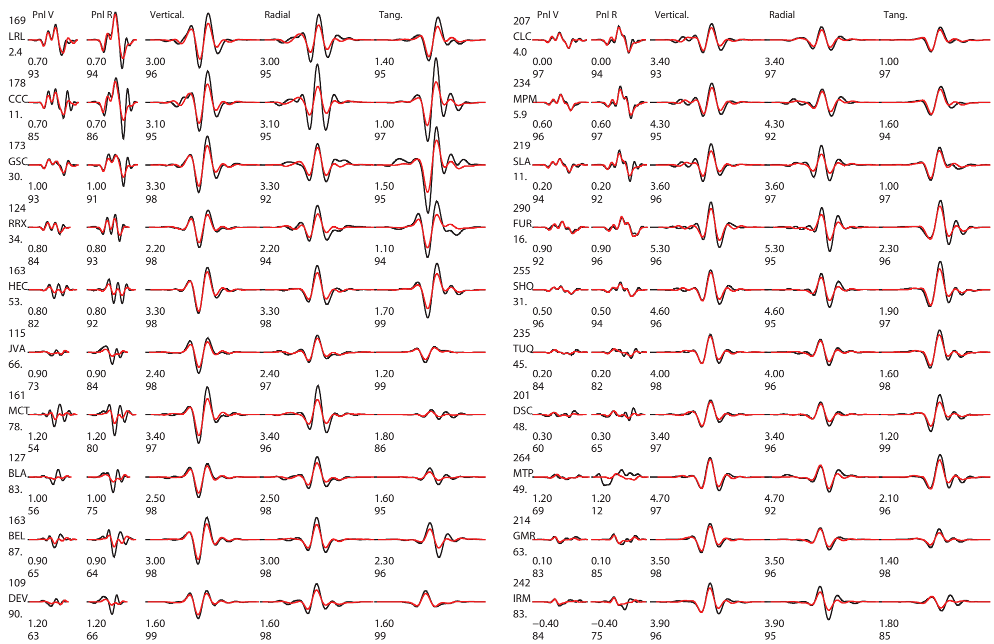


Figure 2.13: Example comparison of synthetic (red) and data (black) for the Chino Hills event at stations in the northeastern direction. The name of station is at the left of each seismogram, the number above the station name is epicenter distance in kilometer and below is azimuth. The number on the lower left of the seismograms are the time shifts (upper) and cross-correlation coefficients in percent (lower). Positive time shifts indicate slow paths. Pnl waves are filtered with bandpass (0.02~0.2 Hz) and surface waves are filtered with (0.01~0.1 Hz), a Standard South California Model (SoCal) is used.

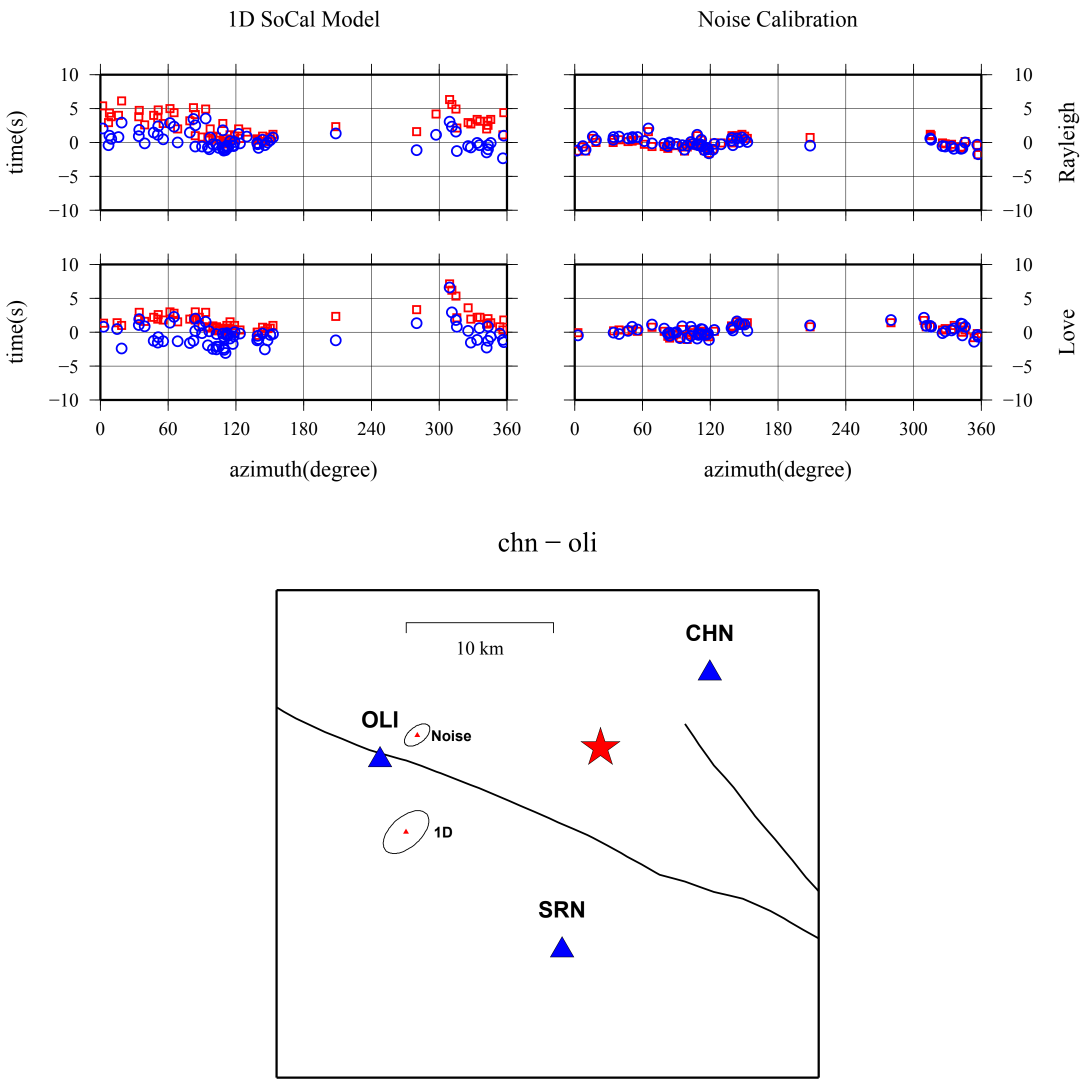


Figure 2.14: Locate virtual source OLI with 1D SoCal model (upper left column) and noise calibration from virtual source CHN (upper right column). Red squares and blue circles are time shifts before and after the relocation respectively. Results are shown in map view as red triangles with 95% confidence limits (black ellipses). Black lines are the Whittier Fault and Chino Fault.

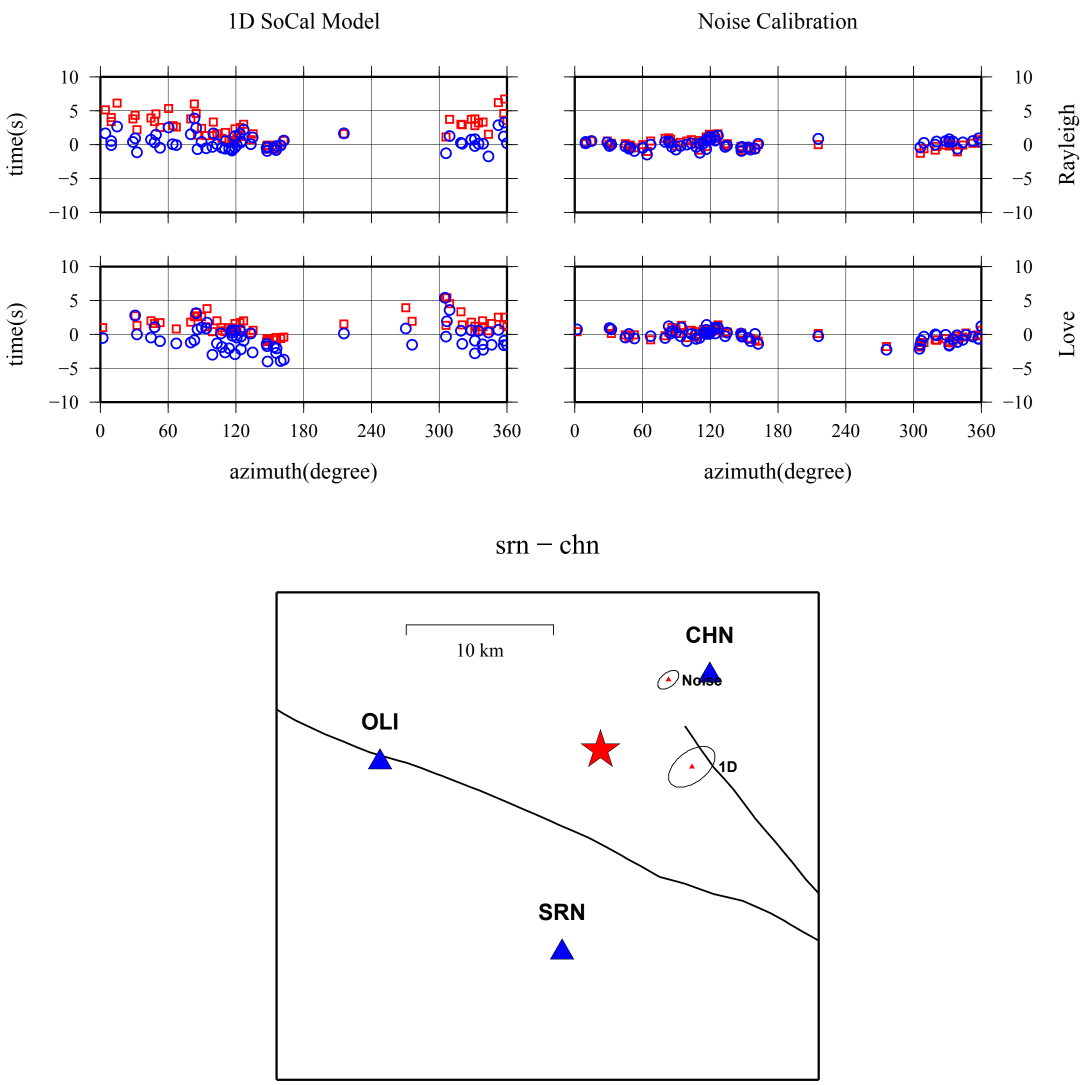


Figure 2.15: The same as Figure 2.14, but for locating CHN with 1D SoCal model and calibration from SRN.

# Chapter 3

# Retrieval of Moho-reflected shear wave arrivals from ambient seismic noise

This chapter has been published as:

Zhan, Z., Ni, S., Helmberger, D. V. and Clayton, R. W. (2010), Retrieval of Moho-reflected shear wave arrivals from ambient seismic noise. Geophysical Journal International, 182: 408–420.

## 3.1 Abstract

Theoretical studies on ambient seismic noise (ASN) predict that complete Green's function between seismic stations can be retrieved from cross correlation. However, only fundamental mode surface waves emerge in most studies involving real data. Here we show that Moho-reflected body wave (*SmS*) and its multiples can be identified with ASN for station pairs near their critical distances in the short period band (1–5 s). We also show that an uneven distribution of noise sources, such as mining activity and wind-topography interaction, can cause surface wave precursors, which mask weaker body wave phases.

## 3.2 Introduction

The Green's function between two stations can be retrieved by cross-correlating extensive periods of ambient noise recordings from seismic stations (Weaver & Lobkis 2001; Snieder 2004; Wapenaar 2004). To date, geophysical studies focused on the surface wave portions of the Green's functions in the period band 5–100 s (Shapiro et al. 2005; Yao et al. 2006; Yang et al. 2007; Bensen et al. 2008; Lin et al. 2008; Zheng et al. 2008; Stehly et al. 2009). These surface waves are then used to study crustal structure (Shapiro et al. 2005; Yao et al. 2006; Yang et al. 2007; Bensen et al. 2008; Lin et al. 2008; Zheng et al. 2008; Stehly et al. 2009), site amplification factors (Ma et al. 2008; Prieto & Beroza 2008) and seismic noise source characteristics (Stehly et al. 2006; Gerstoft et al. 2008; Yang & Ritzwoller 2008). However, the body wave part of the Green's function seems to be more challenging and has rarely been reported from ASN. In the field of exploration seismology, some effort has been made to obtain reflections from ASN. Draganov et al. (2007, 2009) identified P-wave reflections from shallow reflectors (~1 km) with field data. Roux et al. (2005) reports P-wave energy in the noise cross-correlation functions (NCFs) between stations separated by 2–10 km at Parkfield, California, and Zhang et al. (2009) show that the noise is strongly correlated with ocean winds. By analysing the short period seismic noise recorded at Yellowknife array, Koper et al. (2009) show that strong energy propagates as body waves. The difficulty in retrieving body wave phases could be caused by two reasons. First, theoretical studies by Wapenaar (2004, 2006) indicate that to retrieve body wave Green's functions at the free surface requires a distribution of noise sources in depth. However, almost all the seismic noise sources are distributed on the free surface. Although the discontinuities and scatterers below the surface may help to create mirror sources or secondary sources, it is still not clear whether the body wave Green's function is retrievable under this condition. Secondly, as stations are on the free surface, we expect the Green's functions between stations to be similar to the solution to Lamb's problem, in which the surface wave is an order of magnitude stronger than body waves. This effect will be further enhanced by geometric spreading and attenuation. For example, Zhu & Helmberger (1996) show that Rayleigh waves (5–10 s) decay slower than do body waves for a large population of events recorded by a broadband regional network. However, under certain conditions such as post-critical reflections, the amplitude of body waves becomes comparable to that of surface waves at short periods (1–5 s). An example of this is the shear wave reflection from the crust-mantle transition (*SmS*) commonly observed from earthquakes. The strong amplification of this phase near the critical distance in Southern California has been suggested as the cause of particularly strong motions at large distances (Mori & Helmberger 1996).

A strong *SmS* phase requires a laterally coherent crust (Mori & Helmberger 1996) such as the Kaapvaal craton, near Kimberley, South Africa (James et al. 2003) and the Great Slave Lake region in north Canada (Viejo & Clowes 2003; Clowes et al. 2005). The presence of dense seismic arrays in these two regions makes them ideal locations to verify that we can obtain *SmS* from the NCFs. In the Great Slave Lake example, the presence of two dense arrays shows that some of the precursory arrivals are due to uneven noise source distribution, specifically noise voids caused by wind shadows.

## 3.3 Body waves from ambient seismic noise; Southern Africa

We used more than 30 broad-band stations in the Kaapvaal array and the Kimberley array (in Southern Africa Seismic Experiment) under the Kaapvaal Project (James et al. 2003) and BOSA station in global telemetered seismograph network (Figure

3.1) to look for *SmS* arrivals. The red star (Welkom) indicates the location of a mine earthquake (1999 Matjhabeng event) that was well recorded by the Kimberley Array. The broad-band array has been used to derive a detailed 1-D crustal model using the receiver function method (James et al. 2003). The model has a sharp Moho with *P* and *S* velocities jumping from 6.73 and 3.89 km/s to 8.20 and 4.79 km/s in less than 1 km. They used this model to compare synthetic waveforms against those produced by the earthquake with remarkable success. Not only were they able to identify *PmP* and *SmS,* but also their multiples which implies a simple Moho structure and consistent crustal thickness over long distances. A vertical velocity profile of the earthquake data is displayed in the upper half of Figure 3.2 (red). At long-periods, the Rayleigh waves are dominant, although the *Pnl* phases (in the 30–40 s window) can still be observed. These two wavetrains are commonly observed for earthquakes and modelled to determine source parameters (Zhu & Helmberger 1996). Generally, the *SmS* phase is unstable in tectonic regions, which makes the strong *SmS* arrival in craton shown in Figure 3.2 an ideal target to compare the NCFs with earthquake seismograms.

The station pairs are chosen to make SA14, SA26 and SA30 as 'pseudo-source stations' (shown as grey lines in Figure 3.1). Our procedure to compute daily NCFs is similar to that described by Bensen et al. (2007). Continuous vertical velocity records from 1999 January to 1999 June are downloaded from IRIS and cut into daily segments. After removal of mean, trend and instrumental response, the seismograms are bandpass filtered between 1 and 10 s. To remove the effect of earthquakes, we first filter the original seismograms between 15 and 50 s to emphasize the surface waves of earthquakes, and then calculate their envelope functions. The inverse of these smoothed envelope functions are used to weight the corresponding seismograms between 1 and 10 s. This procedure has been proven to be effective to suppress earthquake signals (Bensen et al. 2007). To make the cross-correlation result in 1–5 s

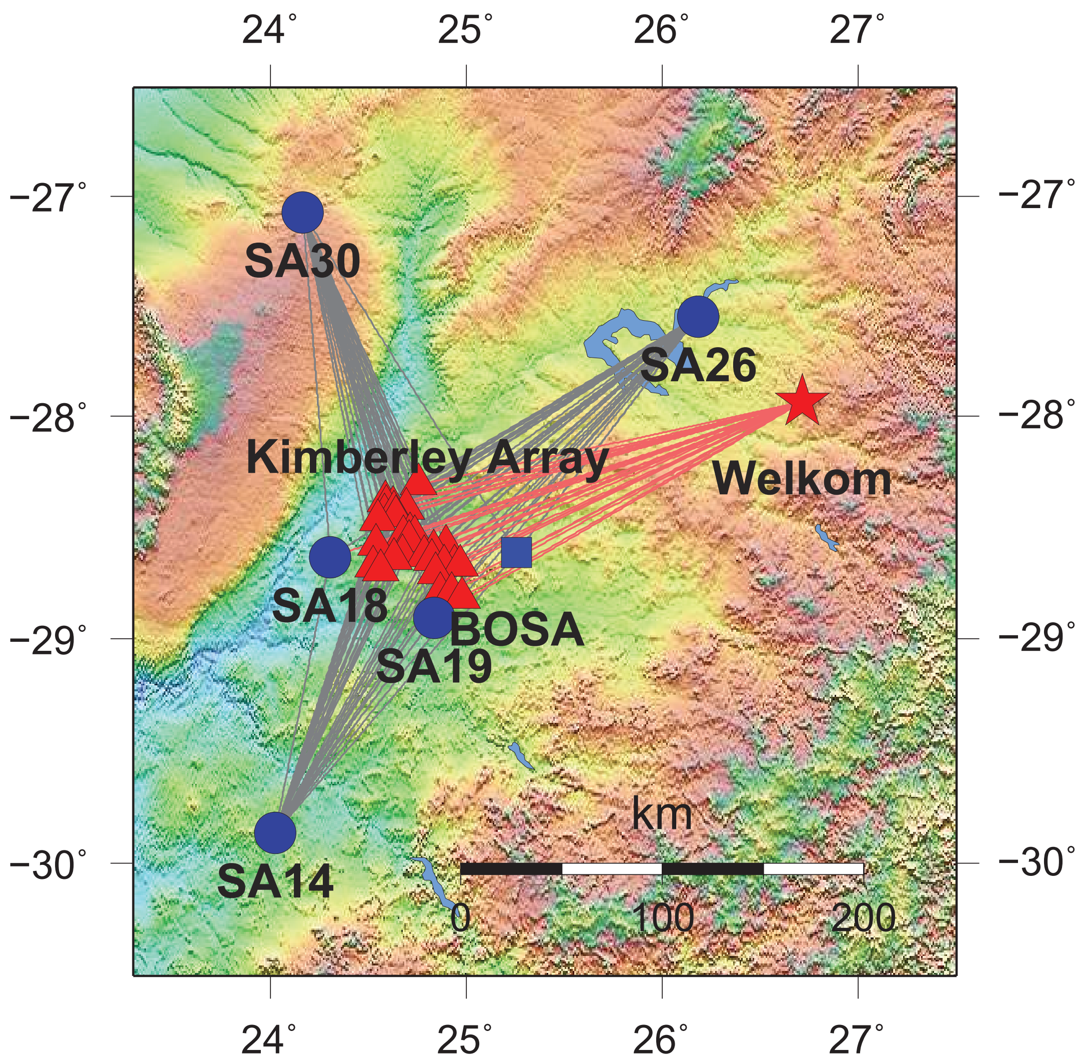


Figure 3.1: Stations used in the Kimberley region and the 1999 Matjhabeng earthquake (Welkom, red star). The red triangles indicate the Kimberley array stations. The blue dots indicate the Kaapvaal array stations and the blue square is an IRIS/GSN station. NCFs are computed along station pairs shown as grey lines, with SA14, SA26 and SA30 as 'pseudo-source stations'. The red lines indicate the paths from the earthquake to the various array stations displaying some overlap with paths from SA26.

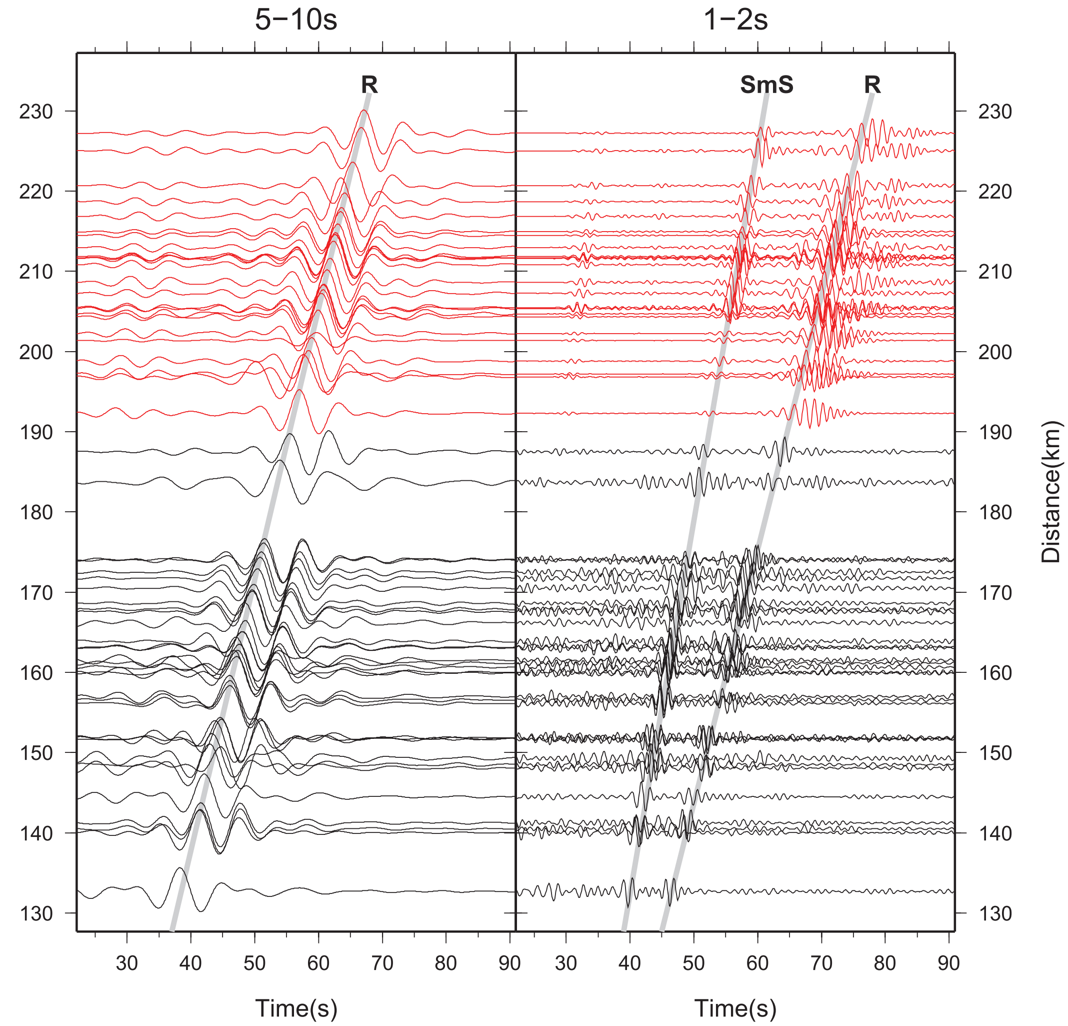


Figure 3.2: Record sections of earthquake broadband vertical velocity records (red lines) and NCFs using SA14 as the source station (black lines). The left and right panels are for 5–10 s and 1–2 s period bands, respectively. In the 5–10 s period band, Rayleigh waves for both earthquake data and NCFs are very clear. The earthquake data has been shifted 4s forward to account for the depth difference between deeper earthquake and pseudo-source station. The same time shift is then applied to the 1–2 s period band. In the 1–2 s period band, the *SmS* of NCFs are well aligned with *SmS* of the earthquake records (James et al. 2003), as well as Rayleigh waves. *SmS* is also present in NCFs with SA26 and SA30 as source stations as addressed later.

more visible, we apply a spectral whitening between 1 and 10 s because the energy in the 5–10 s period band is much stronger than in the 1–5 s band. Cross-correlation is then computed over daily intervals and stacked. All the daily NCFs are normalized to their maximum amplitude before stacking, to avoid erratic data and residual effects of earthquakes. The positive and negative sides of the stacked NCFs are folded and summed to give the final NCFs.

The lower portion of Figure 3.2 shows the NCFs with SA14 as pseudo-source station, filtered in the period bands 5–10 s and 1–2 s. As expected, in the 5–10 s period band, we can see coherent Rayleigh waves in the NCFs and the earthquake records. In the NCFs of 1–2 s, we see clear signals that are coincident with the *SmS* phase in the earthquake seismograms. This identification is confirmed by the similarity of spectrograms of the NCF and earthquake records. Figure 3.3a displays one typical NCF and its spectrogram computed with the multiple filter technique (Dziewonski et al. 1969; Levshin & Ritzwoller 2001). There are two separate wave packets in the NCF. The latter wave packet is of longer period and with an apparent dispersion typical of surface waves. The earlier wave packet in the short-period band (from about 1 to 2 s) displays no dispersion and has a group velocity of about 3.5 km/s. These features are very similar to those in the spectrogram of the seismogram recorded at one station in the Kimberley array generated by the Matjhabeng earthquake (Figure 3.3b). The *SmS* phase can also be observed at station pairs in different azimuth directions with SA14, SA26 and SA30 as source stations (Figure 3.4) and they are all travelling with approximately the same apparent velocity (3.5 km/s). As the group velocity of surface wave is about 3.0 km/s, the angle between the noise directivity and station pair needs to be very close to 31° to make a 3.5 km/s apparent velocity. For example, if the angle is 15 or 45°, the apparent velocity will be 3.11 or 4.24 km/s, which can be easily distinguished from 3.5 km/s. The azimuth range from any station of SA14, SA26 and SA30 to the Kimberley array covers more than 15°. This means

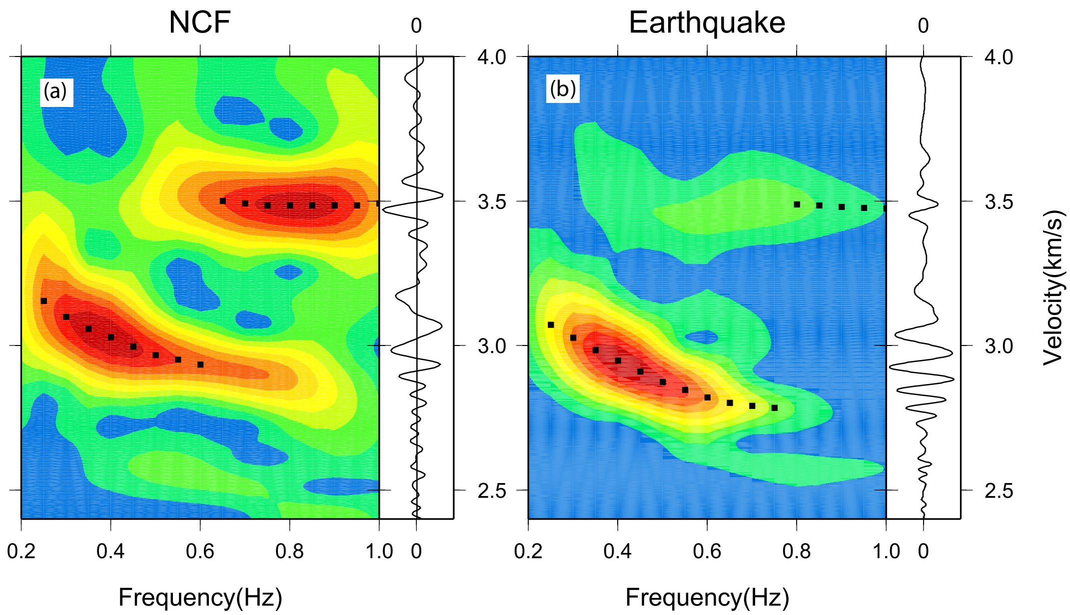


Figure 3.3: (a) One example of NCF and its spectrogram, displaying a dispersive Rayleigh wave, and a non-dispersive short period (1–2 s) signal (*SmS*) with constant group velocity (3.5 km/s). For comparison, (b) shows a seismogram due to the Matjhabeng earthquake, and its spectrogram, which has a very similar pattern of Rayleigh and body waves, thus validating the *SmS* identification.

that the *SmS* is not caused by uneven distribution of the surface wave seismic noise. The NCFs can also detect the first multiple of *SmS* ($SmS^2$) when this phase reaches the critical distance as displayed in Figure 3.5. In this case, we extended the distance to capture the strongest expected $SmS^2$, which is about two times the distance for *SmS*. Here, we see some small differences in the relative waveform packets which are to be expected at these short-periods due to the small-scale variations of Moho topography and crustal structure (Mori & Helmberger 1996).

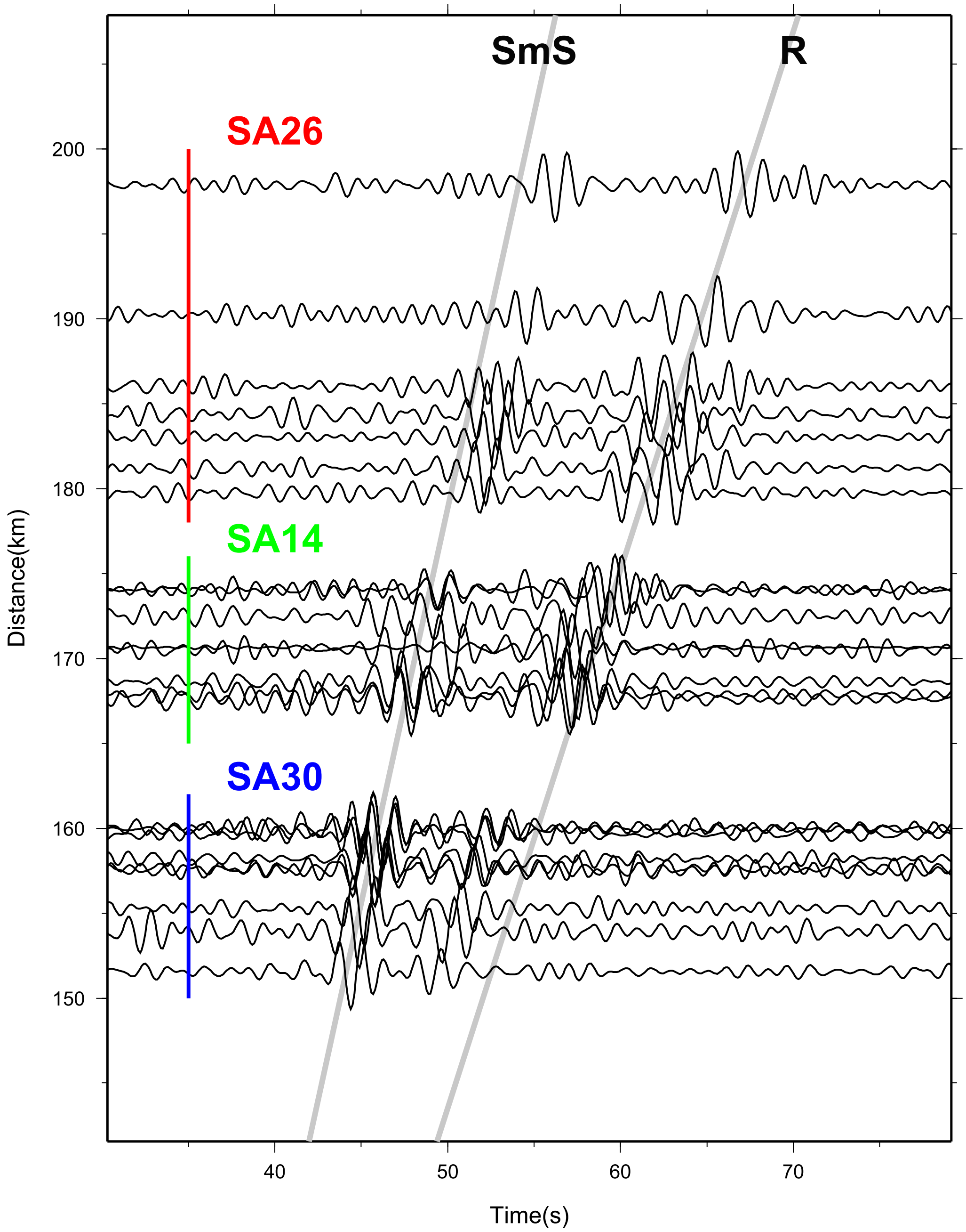


Figure 3.4: Record section generated from a composite set of paths displaying the azimuth independence of *SmS* observations. Clear *SmS* and Rayleigh waves can be seen in NCFs (bandpassed 1–2 s) with SA14, SA26 and SA30 as source stations, which sample a wide range of azimuths. It indicates that the observation of *SmS* in NCFs is independent of station pair azimuths and cannot be due to directivity of noise, which could be a problem in other regions. Not all the NCFs are shown to avoid overlapping of seismic traces.

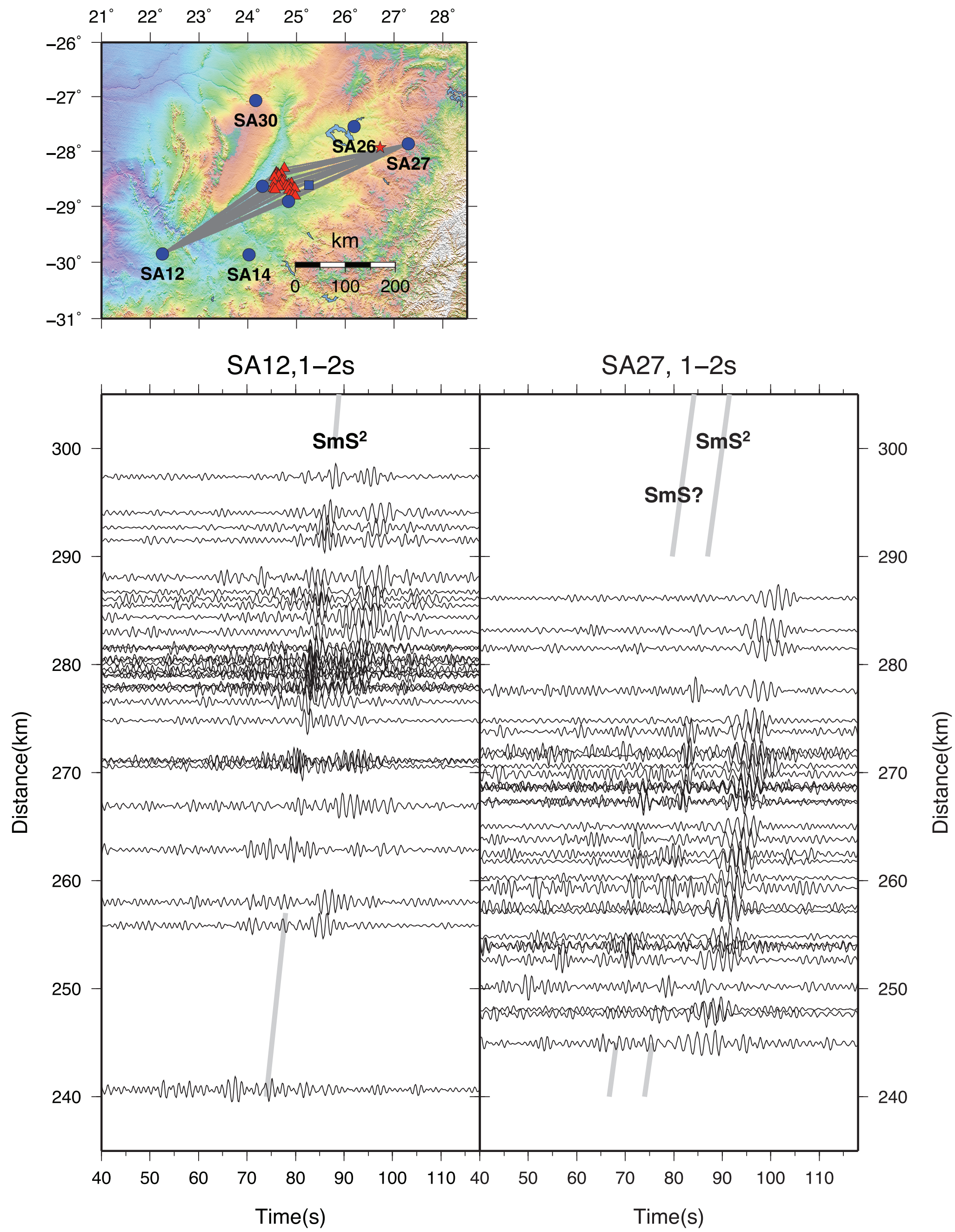


Figure 3.5: Observation of $SmS^2$ in NCFs of station pairs at larger distances with two additional pseudo source stations SA12, SA27 denoted in grey lines. The lower panel displays the NCFs at 1–2 s. At these distances, $SmS$ becomes weak and $SmS^2$ becomes the strongest body wave phase as predicted by heavy grey lines.

## 3.4 Body waves from ambient seismic noise; Northern Canada

The Great Slave Lake region of Northern Canada (Figure 3.6) is another location with simple crustal structure, that has been well determined by the LITHOPROBE seismic reflection and refraction studies (Viejo & Clowes 2003; Clowes et al. 2005). The LITHOPROBE transect covers 2000 km from the Archean Slave craton to the Pacific. A total of 37 shots were detonated and recorded by 600 instruments with average spacing of 1 km. The line starts at Yellowknife at the edge of the Great Slave Lake and crosses the CANOE array as displayed in Figure 3.6. The wide-angle reflection profile for this line shows a remarkably strong *PmP* between 100 and 200 km offset along with synthetic seismograms. As discussed in their paper, the Moho is remarkably flat with variations between 33 and 36 km, and is relatively sharp as in the above example beneath Southern Africa. The crustal model is displayed in Figure 7 where the P and S velocity jump from 6.6 and 3.8 km/s to 8.0 and 4.6 km/s at the Moho. Detailed receiver function analysis at Yellowknife array also shows a similar result (Bostock 1998). In short, this location is ideal for searching for *SmS* body waves from noise cross correlation.

Two dense arrays were deployed in the region as shown in Figure 3.6. One is the permanent Yellowknife array (YKA), and the other is the temporary CANOE array (Mercier et al. 2008). We will use these two arrays to interrogate the directional properties of the noise field and NCFs. Continuous data from May 2004 to July 2005 are downloaded from IRIS. The procedures to compute the NCFs are the same as those used in South Africa. The NCFs (bandpassed at 2–10 s) along the paths shown as grey lines in Figure 3.6 are given in Figure 3.8. Because the crustal model is known from the above study, we attempted to compare these NCFs directly with synthetic 1-D Green's functions. After some minor adjustments in the shallow velocities as

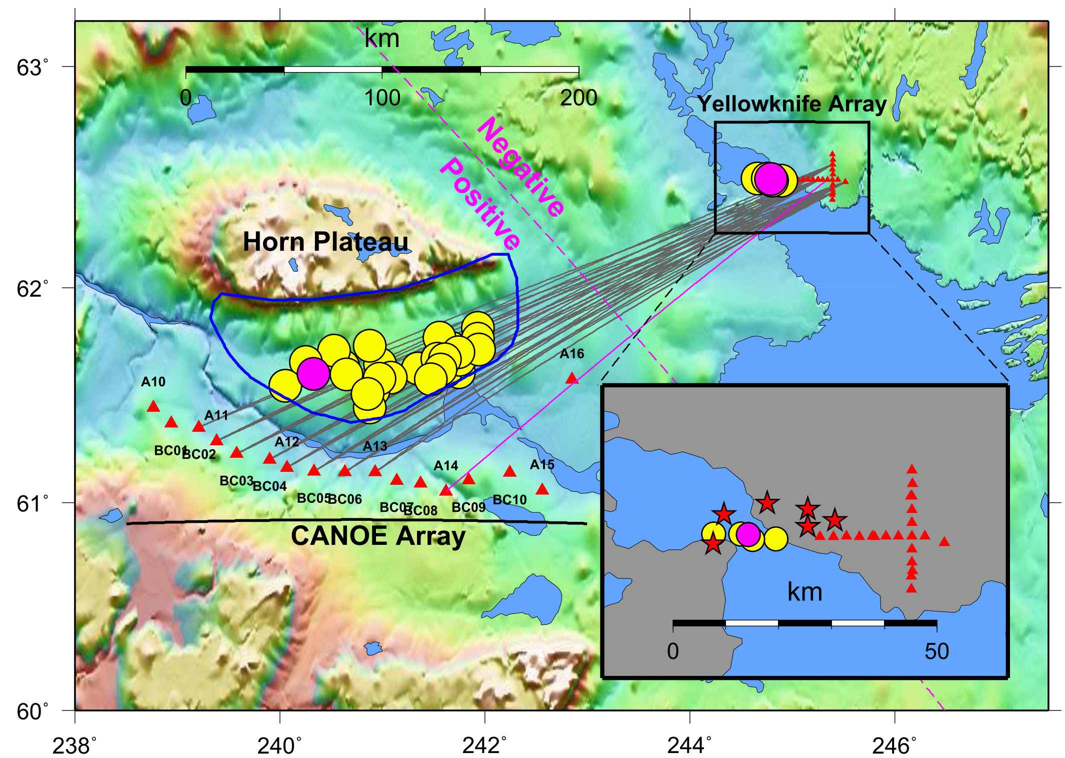


Figure 3.6: Geometry of a second ASN test involving stations (red triangles) in two arrays, a closely spaced array (Yellowknife), and a broadband array (CANOE). The grey and purple lines are the paths where NCFs have been studied. The purple dash line, which is the perpendicular bisector of the purple line (A14 to YKA), separates the noise sources contributing to the positive or the negative side of the NCF with A14 as the pseudo-source. The purple and yellow dots indicate the locations of identified noise source anomalies (NSAs). The left group of dots to the south of large topographical feature Horn Plateau lie in the approximate area with much lower annual average wind speed than surrounding area (blue curve, data from Canada Environment 2009). The right group of dots coincides with known mining blasts in 2004 and 2005 reported by Earthquakes Canada (red stars in the inset).

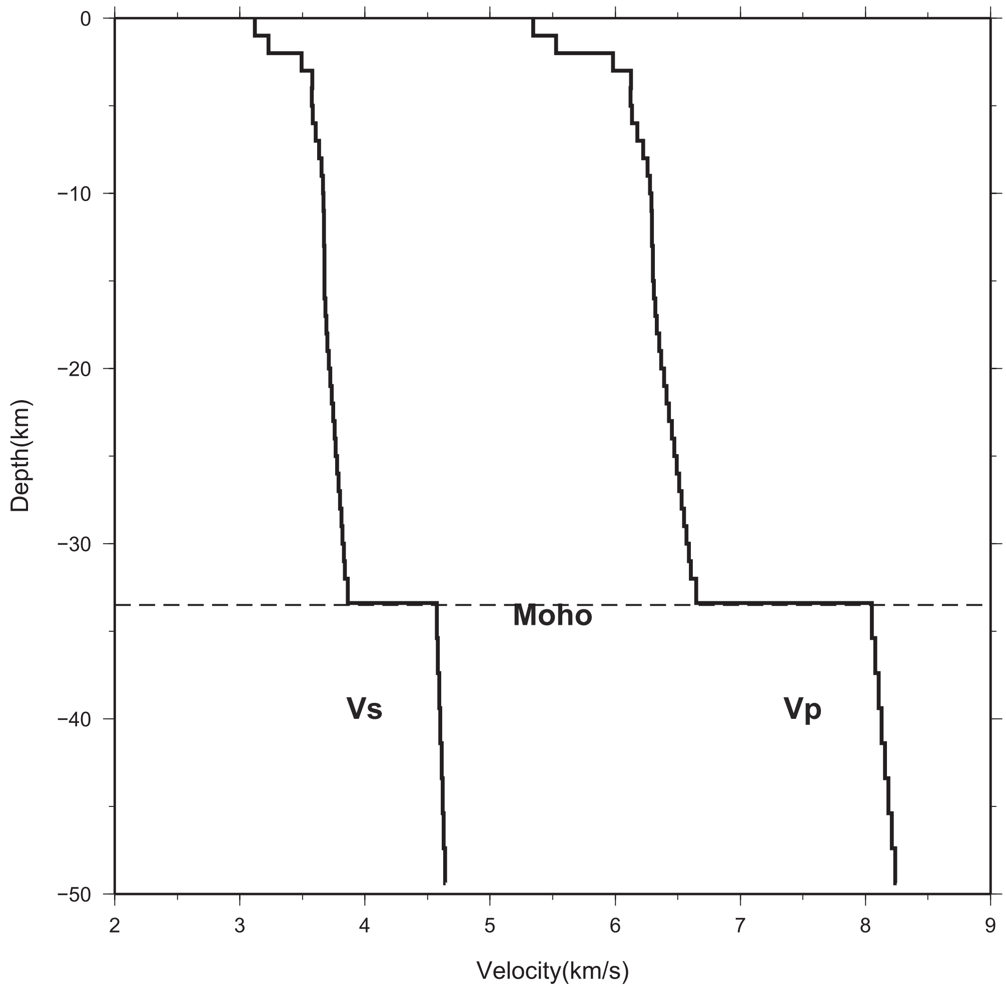


Figure 3.7: 1-D Vp and Vs model used to calculate the synthetic seismograms. This model is averaged from SNORE' 97 (Viejo & Clowes 2003; Clowes et al. 2005) and then modified for the top 5 km (where the wide-angle reflection experiment has little resolution) to fit short period surface waves.

given in Figure 3.7, we obtained the match displayed in Figure 3.8. These synthetics were generated with a frequency–wavenumber (w-k) synthetic seismogram package (Zhu & Rivera 2002) assuming the source station is replaced by a vertical point force. The distances between stations here are from 280 to 350 km, which is beyond the critical distance range of *SmS*, but falls in the critical distance range of $SmS^2$. The synthetic Green's functions match both surface waves and $SmS^2$ body waves very well. Figure 3.9 shows the comparison of NCFs and synthetic Green's functions over the paths with shorter distances (150–180 km) where SmS is in the critical reflection range. Station A16 is the only station at this distance range to YKA. The synthetics (red) are computed with the same 1-D crustal model and w-k code as in Figure 3.8. The fit to the *SmS* is again excellent confirming our identification of body waves retrieval from noise analysis. The fit to the surface waves in this case is disturbed by the slightly shorter period (2–5 s, rather than 2–10 s to avoid the interference between Rayleigh waves and *SmS*) and possible lateral heterogeneity of shallow structure. Note that the *SmS* is not sensitive to the shallow structure as the nearly vertical path through it is only a very small fraction of the entire path.

These two examples in South Africa and Northern Canada demonstrate definitive observations of *SmS* and $SmS^2$ from ASN when they have large amplitudes near their critical distances. This means that although almost all the noise sources are distributed on the free surface, there seems to be no difficulties in retrieving body waves from ASN when they are supposed to have large amplitudes in the Green's functions. In the next section, we will discuss problems in obtaining other weaker body wave phases, which may be masked by the waves in NCFs which are neither surface wave nor body wave phases.

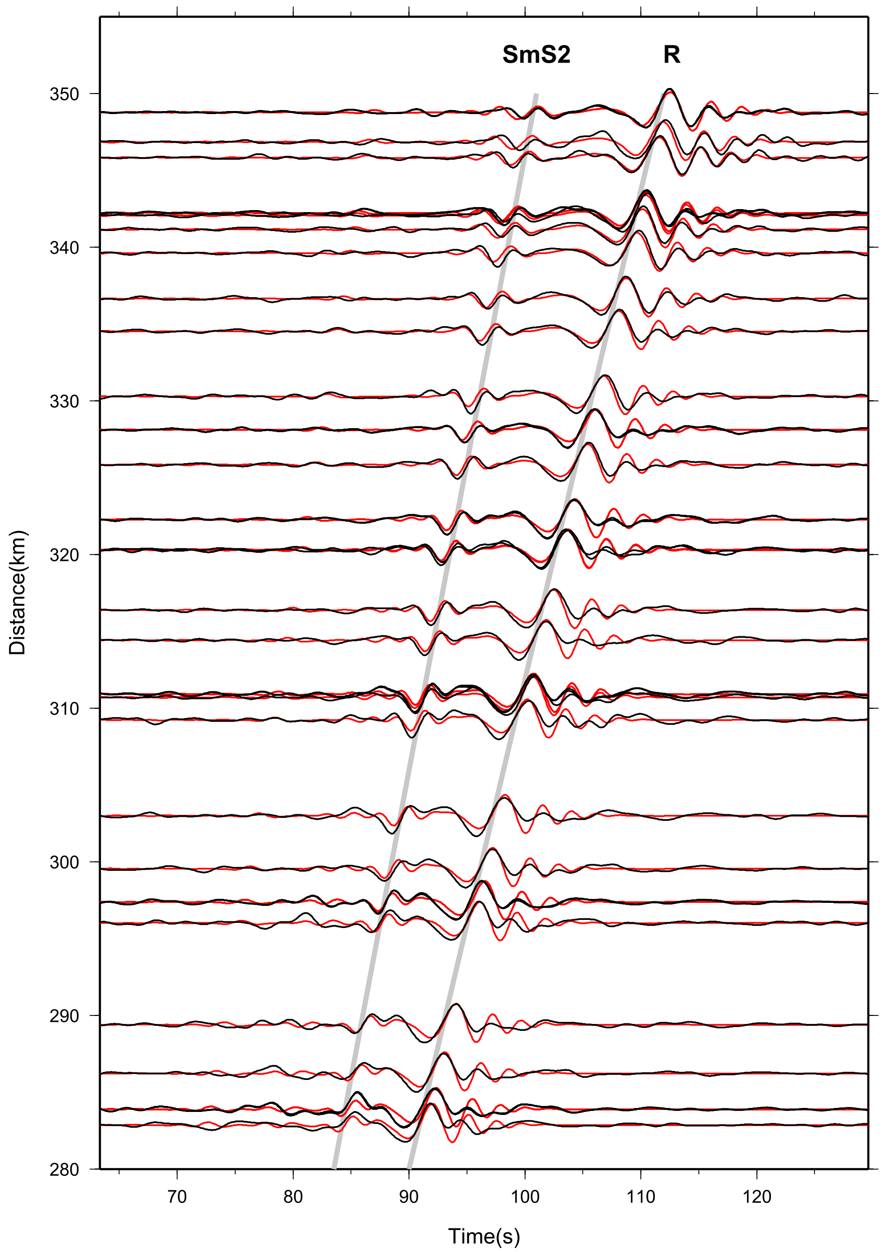


Figure 3.8: Comparison of synthetic Green's functions from a known structure with noise cross-correlation functions (NCFs) near Great Slave Lake. The black lines are NCFs of station pairs shown as gray lines in Figure 3.6 with distance range from 280 to 350 km. More complete NCFs (with NCFs between all station pairs) are addressed later. The red lines are synthetic seismograms with a single vertical force at one station, recorded at the other station. The seismic 1-D model is taken from Viejo & Clowes (2003) and Clowes et al. (2005), shown in Figure 3.7. At this distance range, the two most visible phases are $SmS^2$ and Rayleigh waves. The great agreements between NCFs and synthetics indicate definitive identification of $SmS^2$.

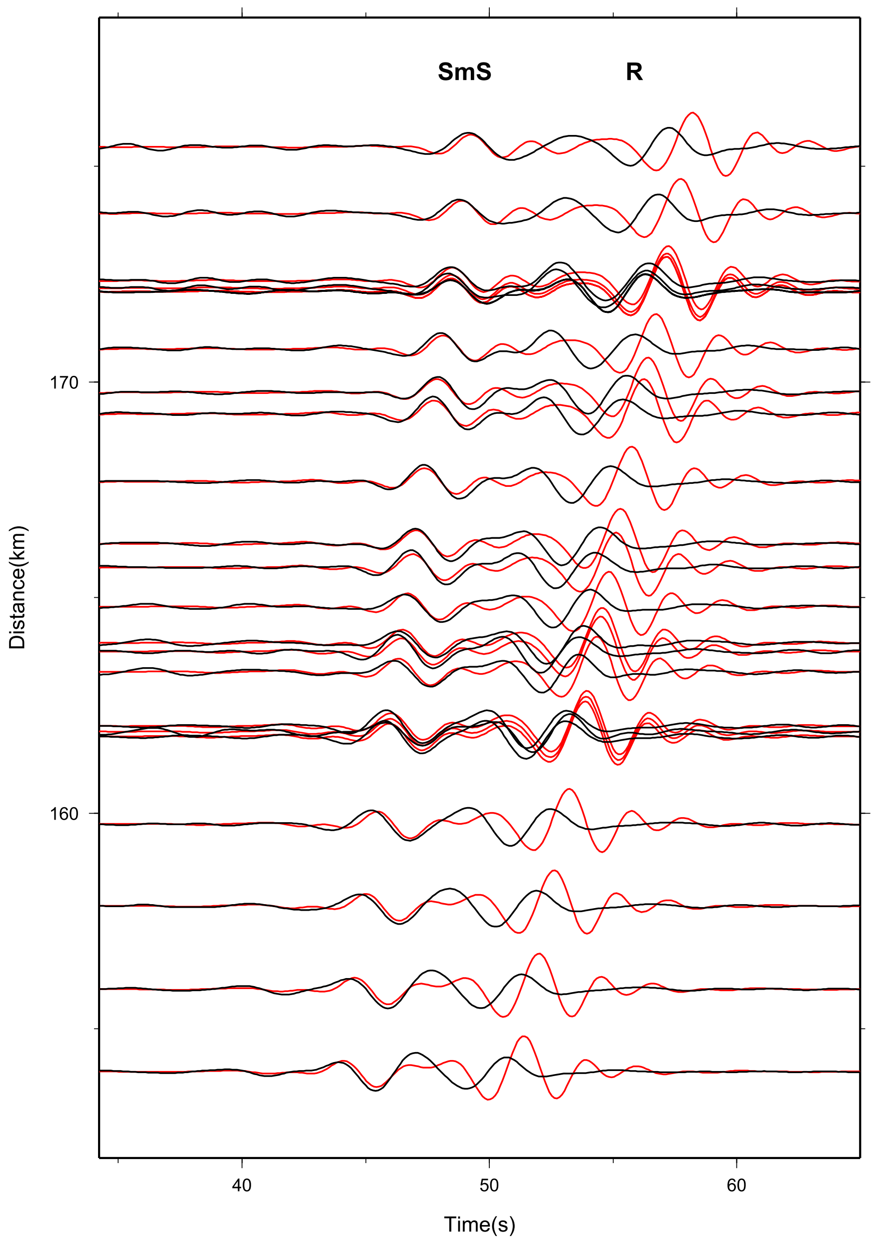


Figure 3.9: Observation of *SmS* in NCFs (bandpassed 2–5 s) of station pairs with A16 as pseudo source station. A16 is the closest CANOE station to YKA used in this study (150–180 km). At this distance range, the *SmS*[2] has not reached the critical reflection distance, and SmS is the strongest body wave phase. The black and red lines are the NCFs and synthetic seismograms computed with the 1-D model in Figure 3.7, respectively. The disagreement of Rayleigh waves is probably due to the lateral change of shallow structure.

## 3.5 Surface wave precursors caused by local noise anomaly

The density of stations in the Great Slave region allows a detailed record section to be constructed with over 400 NCFs (as displayed in Figure 3.10 at period bands 2–10 s and 1–2 s). The positive side and negative side have been folded and summed. For 1–2 s period band, the body wave arrivals have the same travel times as in 2–10 s period band while the Rayleigh waves are delayed due to dispersion. This increases the $SmS$ and $SmS^2$ separation from the Rayleigh waves in the 1–2 s period band, hence easier to identify. On the other hand, the stronger attenuation due to the increase of frequency content decreases the coherence between stations, which makes the NCFs much noisier. Consequently, in the following, we will concentrate on the 2–10 s period band. As expected for typical triplication behaviour, the record section shows that $SmS$ is strong in the distance range 150–180 km, while $SmS^2$ emerges beyond 280 km. Hence, the window near 250 km should be relatively free of strong body waves (Figure 3.10). The station pairs between A14 and YKA (solid purple line in Figure 3.6) are in this window. Figure 3.11 shows their stacked NCFs for November and December of 2004 with both positive and negative sides present. The NCFs of the summer seasons are not used here because the strong teleseismic $P$-wave energy from storms in the southern hemisphere causes strong artefacts near zero lag time (Gerstoft et al. 2008). As they appear outside the time window in which local body wave phases may be present, they are not discussed here. In Figure 3.11, besides the surface waves shown by the red arrows, clear arrivals persist before the surface waves. The most visible ones are denoted by blue arrows on each side. Note that the precursors on two sides are not symmetric in waveform or travel time. The precursors denoted by blue arrows on the positive side have much longer durations than those on the negative side. Similar precursors can be observed in many previous ASN studies (Shapiro et al. 2005; Yao et al. 2006; Lin et al. 2008), but their source has not been identified.

The dense Yellowknife array enables us to have a closer look at these precursors. They appear to be coherent over the entire array, which means they are probably caused by some physical feature. The YKA consists of two perpendicular legs as shown in Figure 3.6. In Figure 3.11, the NCFs between A14 and Yellowknife stations on the east-west leg are coloured in blue, with the north-south leg in red. The precursors on the negative side have a different moveouts on the east-west leg than on the north-south leg, as denoted by the dash lines. More quantitatively, Figure 3.12 shows a detailed frequency-wavenumber (FK) analysis (Rost & Thomas 2002) for precursors on both the positive and negative sides. Blue arrows are their velocity vectors while red arrows are velocity vectors of corresponding direct surface waves. A comparison between these two FK plots shows that these precursors have surface wave velocity (blue and red arrows have similar length). They are not travelling along the great-circle path as the blue arrows have a different azimuth than the red arrows. Because these arrivals are precursors, they must have originated from anomalous noise sources because scattered surface waves would arrive after the direct Rayleigh wave. In particular, their azimuths as obtained by the FK analysis and absolute travel times which is the difference of travel times from the noise source anomaly (NSA) to the two stations allow these NSAs to be located (see the schematic in Figure 3.13). The two NSAs determined above are shown as purple dots in Figure 3.6.

We can determine additional locations of NSAs by examining more time windows of the NCFs. They are shown as yellow dots in Figure 3.6 and clearly cluster into two groups. One group concentrated near the Yellowknife array, while the other is more dispersed in a region to the south of the large topographic feature called the Horn Plateau. The first group of dots coincide with locations of several mining explosions (inset of Figure 3.6), hence probably indicates a noise anomaly generated by mining processes. Although these explosions have been diminished before cross correlation

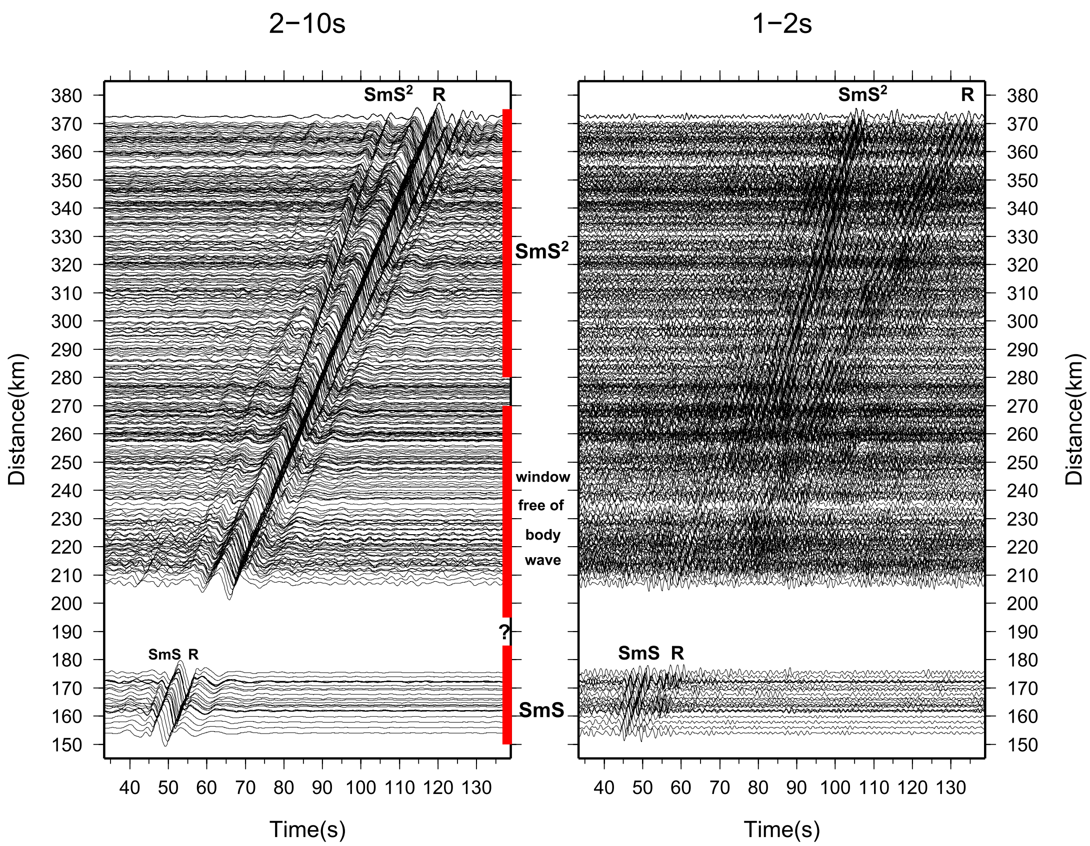


Figure 3.10: (Left panel) Complete record section of over 400 NCFs between CANOE array and Yellowknife array. NCFs have been bandpass filtered between 2 and 10 s. The positive side and the negative side are summed. *SmS* dominates *SmS*$^2$ at shorter distance range but *SmS*$^2$ dominates at larger distances as expected for a typical triplication behaviour. Between these two ranges, there is a window between 200 and 270 km relatively free of body waves. But clear signals still persist before surface waves (surface wave precursors), which are discussed in the text. (Right panel) Complete record section of NCFs for 1–2 s period band. Although much noisier, *SmS*$^2$ and Rayleigh waves can still be recognized. Although *SmS*$^2$ keeps its travel time the same as in 2–10 s period band, the Rayleigh waves are delayed because of dispersion as discussed earlier. SmS is actually cleaner because the amplitude of surface wave becomes much smaller.

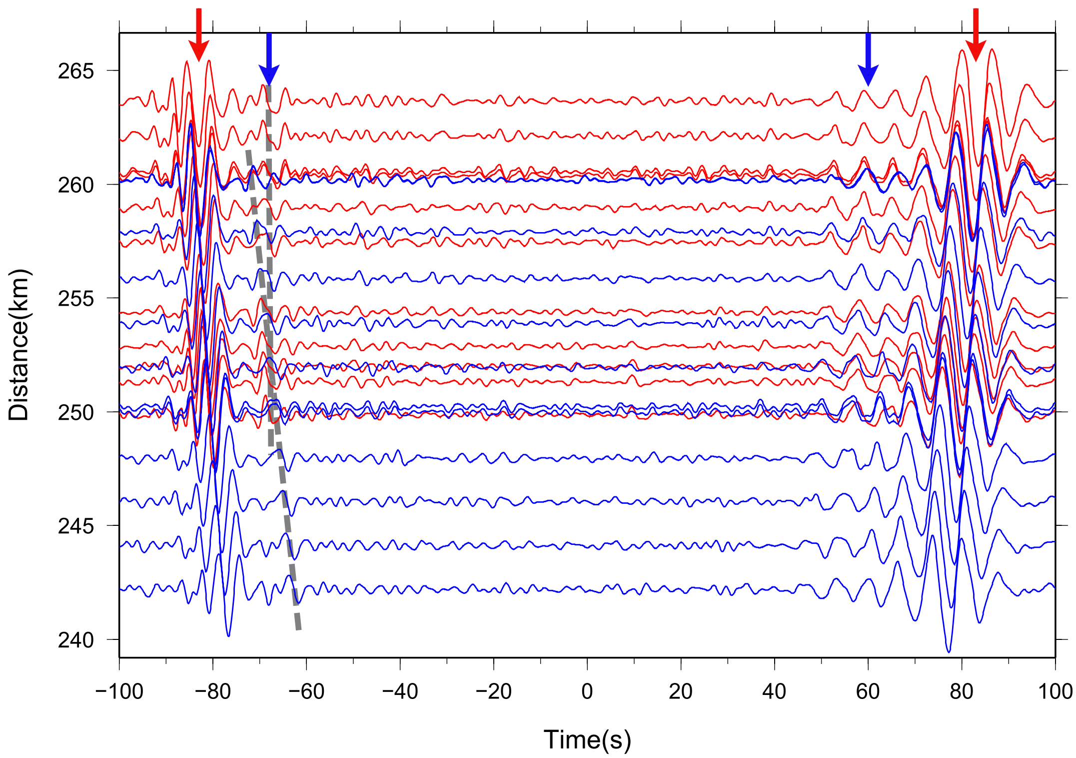


Figure 3.11: Observation of clear and coherent surface wave precursors in NCFs (2–10 s) between A14 and YKA stations for 2004 November and December at a distance of 250 km. At this distance range (about 250 km apart), *SmS* and $SmS^2$ are weak compared with Rayleigh waves (shown by the red arrows). However, we can still observe clear signals arriving before Rayleigh waves (surface wave precursor), for example the signals marked by the blue arrows. These precusors are coherently present in NCFs between A14 and YKA stations. Note that the positive sides and negative sides of NCFs are not symmetric, which is probably because of the difference of noise from Pacific Ocean and Atlantic Ocean.

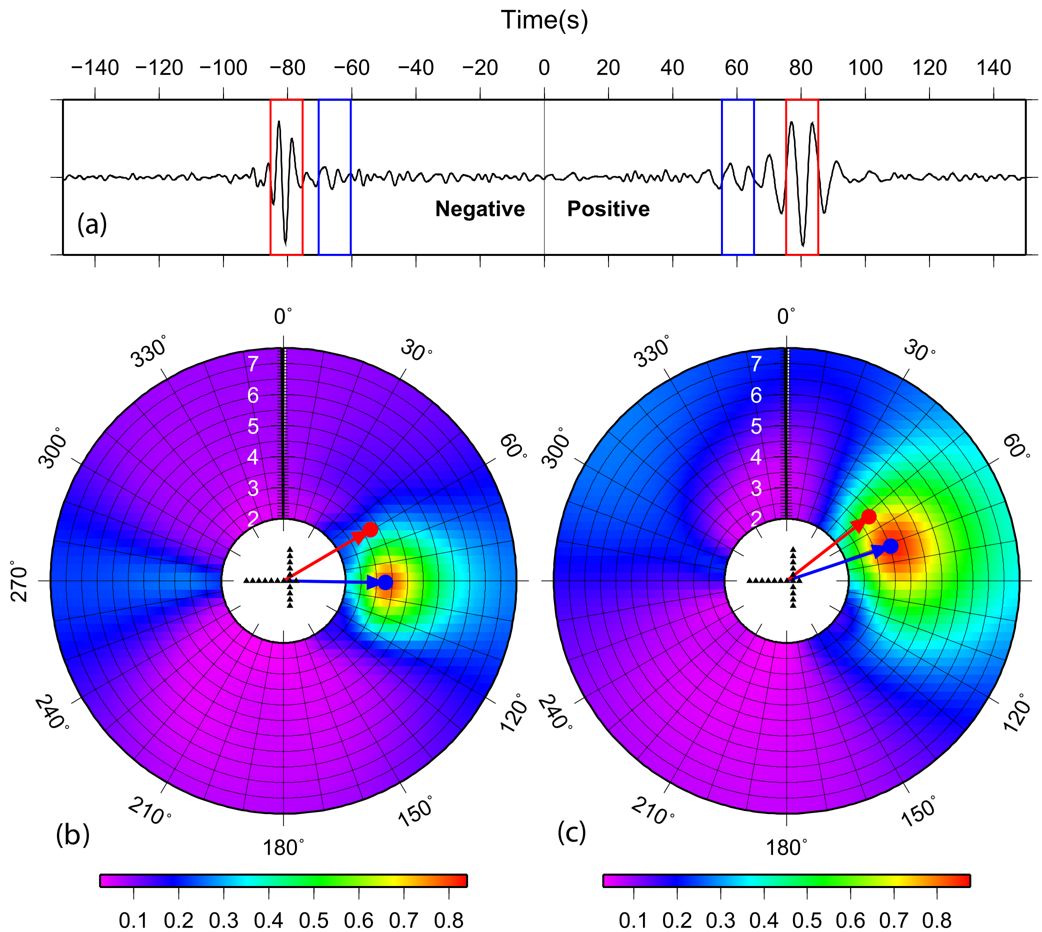


Figure 3.12: Locating NSAs with sliding-window frequency–wavenumber (FK) analysis (Rost & Thomas 2002) of surface wave precursors. (a) Shows one example of NCF between A14 and YKR7. Because of the precursors coherence shown in Figure 3.11, we can measure their apparent velocity vector defined by propagation azimuth and apparent velocity with Sliding-Window FK analysis. Results for the two windows defined by blue boxes are shown in (b) and (c), respectively. The background colour is normalized power of stacked signals (Rost & Thomas 2002). The blue arrows are the optimal apparent velocity vectors and blue dots show the corresponding velocities and azimuths. For comparison, the apparent velocity vectors for Rayleigh waves (red boxes) are also plotted as red arrows and red dots. We can see that the blue arrows have very close velocities (lengths) to red arrows (from Rayleigh waves), but quite different azimuths. This means that the precursors are not body waves, but surface waves travelling off the great circle.

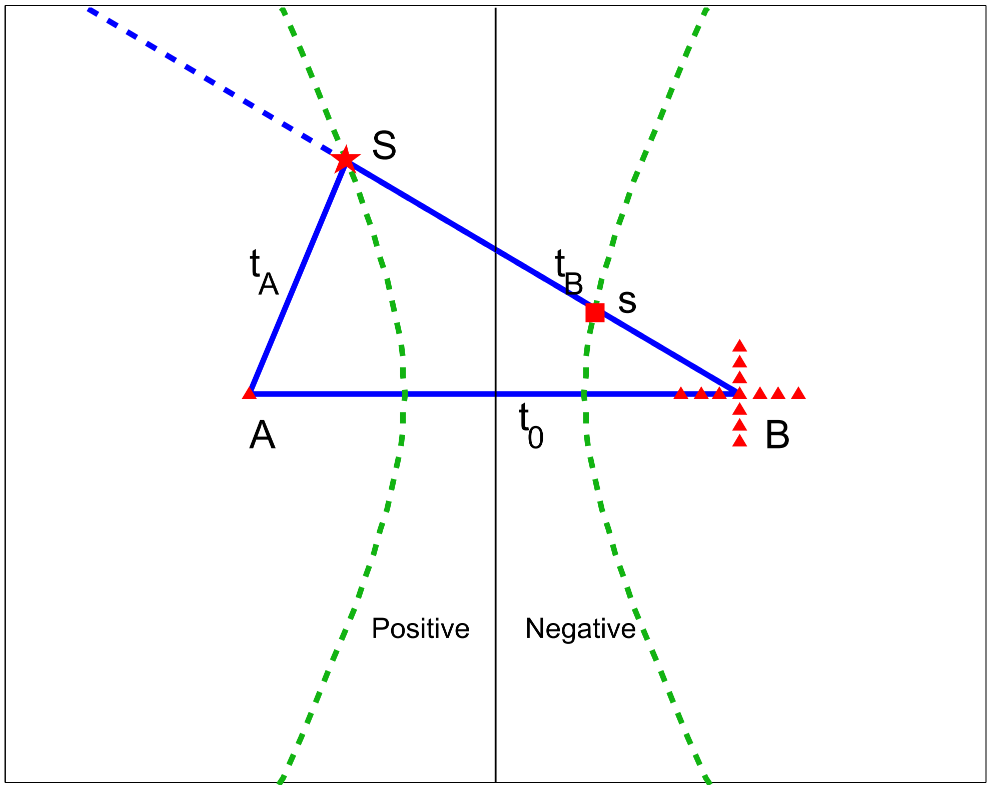


Figure 3.13: Noise source anomaly (NSA) and method to localize an NSA. Suppose we have a scenario shown in this figure, where red triangles are stations. $B$ is an array with stations $B_i$. An NSA at point $S$ (uniform part already subtracted) emits surface wave noise continuously. It will be recorded at station $A$ with a delay $t_A$, array station $B_i$ with a delay $t_{B_i}$. The NCFs between station A and array stations $\mathrm{B_i}$ will have a signal at $t_{B_i} - t_A$. As $t_{B_i} - t_A$ is always smaller than $t_0$, the signal arrives earlier than the surface wave Green's function (surface wave precursor). It should be noticed that the relative travel times of this signal across the $B$ array do not change after cross correlating with station $A$. This enables us to use FK to determine the azimuth of the NSA (dash blue line in the figure). Assuming the similarity of waveforms recorded at station $A$ and the array, the absolute time of maximum cross correlation is $t_{B_i} - t_A$, which requires the NSA on a hyperbola (green dash lines in the figure). These two steps lead to two possible locations of the NSA, shown as $S$ (red star) and s (red squares). They can be distinguished by whether the precursor appears on the positive or negative side of NCFs.

by temporal normalization (Bensen et al. 2007), the continuous noise generated by the mine cannot be removed. The second group of NSAs lies in the wind shadow (with much lower wind speed than surrounding area) of the Horn Plateau (Canada Environment 2009), as the dominant wind direction in this area is from north to south. We suggest that this group of NSAs is generated by an absence of wind-land-interaction (i.e., a void) in the assumed uniformly distributed noise sources. A synthetic to support this is shown in Figure 3.14, where a void of noise sources from azimuth 40° to 50° causes a surface wave precursor in the NCF.

## 3.6 Discussion and Conclusion

As shown by Weaver & Lobkis (2001), the equipartitioning of the Earth's normal modes in noise will allow us to obtain the complete Green's function between two stations. However, as pointed out by Snieder (2004), the fact that almost all of the noise sources are distributed on the Earth surface means fundamental surface wave modes contain most of the energy. Theoretical studies by Wapenaar (2004, 2006), Snieder (2004) and Fan & Snieder (2009) show that to obtain the fundamental mode surface wave part of the Green's function, the distribution of noise source on the free surface is enough. However, for body wave phases, such as reflections, noise sources at depth are necessary. This seems to mean that body wave phases are not retrievable from seismic noise as almost all the noise sources are on the free surface. However, they also pointed out that inhomogeneous structure of the Earth may be helpful to fix this difficulty. For example, Snieder (2004) treat the subsurface discontinuity as a mirror to create mirror-source at depth. Until now, it is still not clear whether we can get the body wave part of the Green's function or even the complete Green's function from this surface-generated seismic noise. The weak amplitude of body wave phases in the Green's function make the problem even harder. As stations are on the

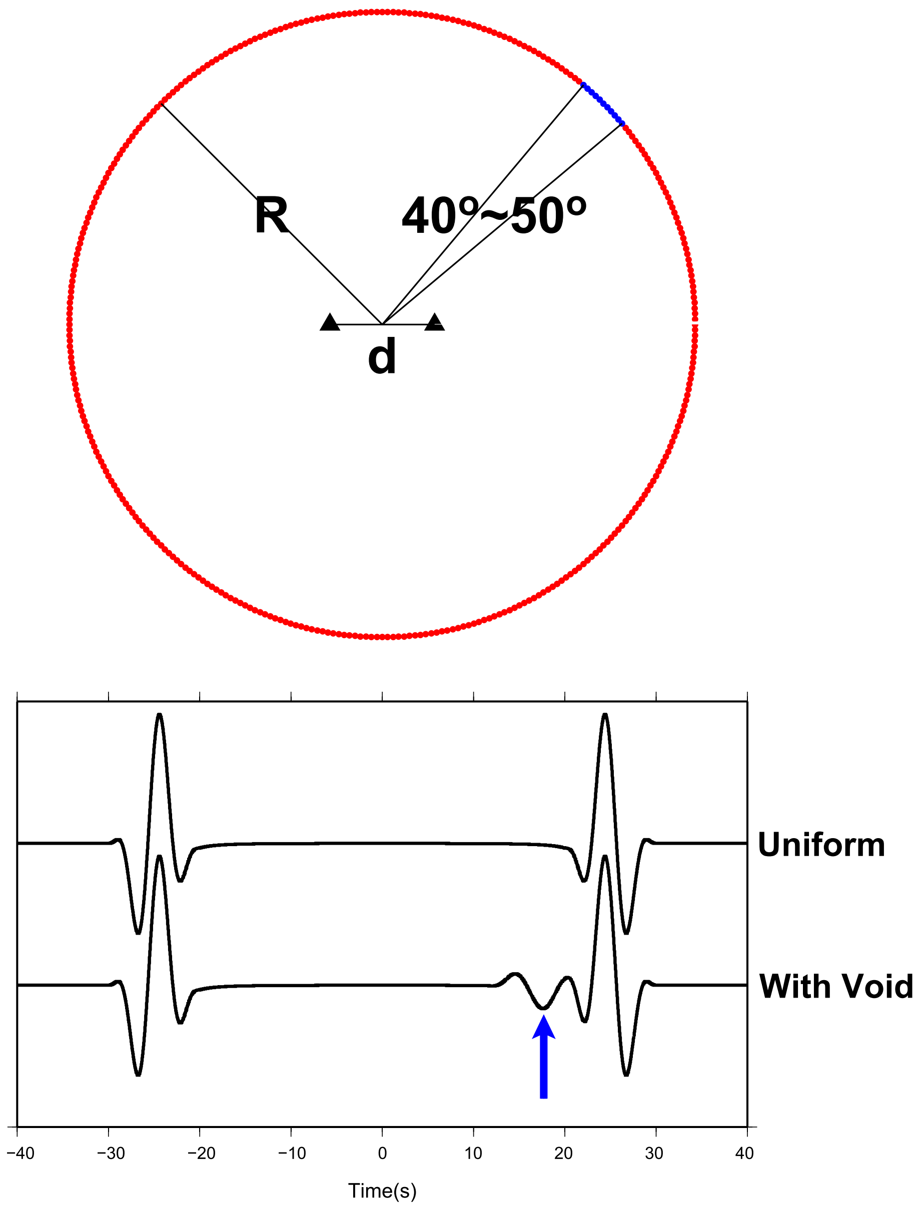


Figure 3.14: Two stations separated by $d$=100 km are surrounded by a circle of noise sources ($R$=300 km). We simulated two cases here: (1) noise sources distribute uniformly on the circle; (2) same as (1) except that the noise sources between 40° and 50° (blue part in figure) are taken off. The corresponding synthetic NCFs at 5 s period are shown in lower panel. The void of noise sources causes a surface wave precursor on the NCF, marked by the blue arrow.

free surface, we expect the Green's function to be similar to the solution to Lamb's problem in which the surface wave is an order of magnitude larger than the body waves.

In this paper, by array analysis of NCFs in cratons with simple crustal structures, we show that the noise cross correlation technique now can detect certain body wave phases when they have comparable strengths in certain conditions ($SmS^n$ near their critical distances in our examples). The reason for strong SmS and its multiples to be observed from ASN could be that noise sources are distributed in the whole crust instead of just being near the free surface. Being the most heterogeneous part of the Earth, crust consists of scatterers at many scales and strongly scatters waves with resonant wavelength. Moreover, because of the lower velocity, crust behaves as a wave guide channel trapping most of the body wave energy inside, which explains dominant *Lg* waves for regional crustal earthquakes and should also be expected for ambient seismic noises (Kennett 1984; Kennett & Mykkeltveit 1984). Indeed array analysis by Koper et al. (2009) supports that strong energy of short period seismic noise propagates as *Lg* waves. Cormier & Anderson (2004) argues that Lg wave is dominated by multiple *SmS* arrivals. This means that there is sufficient energy in the noise field trapped between the surface and the Moho to allow the retrieval of body waves in the short period band.

Scattering due to topography or microbasins (very thin basins) could be another mechanism of converting wave field of dominant surface wave into wave field of both surface wave and body wave, as observed and modelled by Clouser & Langston (1995). In their study, Rayleigh waves are proposed to be generated by teleseismic *P* waves. According to reciprocity, *P* waves can also be expected by Rayleigh waves scattered by topography. Although topographic variation in cratons are fairly weak, microbasins may serve as strong scatterers (Stead & Helmberger 1988).

Other body wave phases are probably present, but masked by the persistent surface wave precursors due to uneven distribution of noise sources. These noise source anomalies could be human activities, wind–topography and other solid–fluid interactions of the Earth, such as storms (Bromirski 2009). By numerical simulation Lin et al. (2008) shows that as long as the strength of the noise source varies smoothly versus azimuth, the bias to the surface wave Green's function is negligible. The broad microseism source area and scattering may contribute to this smooth variation. However, as shown by this paper, nearby noise source anomaly may not have such a smooth variation because of high heterogeneity of distribution and lack of scattering over short distances. Better understanding of the noise sources, especially these local noise source anomalies will help suppress the contaminating surface wave precursors to get the complete Green's functions from the NCFs. Also, as *SmS* can be much stronger than surface waves around 1 s, detailed analysis of NCF in this frequency band can provide a valuable tool for site amplification mapping.

## Acknowledgments

The authors thank the operators of the Southern Africa Seismic Experiment and CANOE array, IRIS, Earthquakes Canada for providing data used in this study. We acknowledge Ronald M. Clowes and Gabriela Fernandez Viejo for providing the velocity model of Great Slave region. The suggestions from two reviewers were very helpful to improving the paper. This work was supported by NSFC 40674027 and CAS fund kzcx2-yw-116-01 and by USGS Award #G09AP0082 at California Institute of Technology.

## References

Bensen, G.D., Ritzwoller, M.H., Barmin, M.P., Levshin, A.L., Lin, F., Moschetti, M.P., Shapiro, N.M. & Yang, Y., 2007. Processing seismic ambient noise data to obtain reliable broad-band surface wave dispersion measurements, Geophys. J. Int., 169(3), 1239–1260.

Bensen, G.D., Ritzwoller, M.H. & Shapiro, N.M., 2008. Broadband ambient noise surface wave tomography across the united states, J. geophys. Res., 113(B5), B05306, doi:10.1029/2007JB005248.

Bostock, M.G., 1998. Mantle stratigraphy and evolution of the Slave province, J. Geophys. Res., 103(B9), 21183–21200, doi:10.1029/98JB01069.

Bromirski, P.D., 2009. Earth vibrations, Science, 324(5930), 1026–1027.

Canada Environment, 2009. Wind atlas of Canada. Available at:http://www.windatlas.ca/, accessed on 2009 December 1.

Clouser, R.H. & Langston, C.A., 1995. Modeling P–Rg conversions from isolated topographic features near the Noress array, Bull. seism. Soc. Am., 85(3), 859–873.

Clowes, R.M., Hammer, P.T.C., Fernandez-Viejo, G. & Welford, J.K., 2005. Lithospheric structure in northwestern Canada from lithoprobe seismic refraction and related studies: a synthesis, Can. J. Earth Sci., 42(6), 1277–1293.

Cormier, V.F. & Anderson, T.S., 2004. Efficiency of Lg propagation from SMS dynamic ray tracing in three-dimensionally varing crustal waveguides, Pure appl. Geophys., 161, 1613–1633.

Draganov, D., Wapenaar, K., Mulder, W., Singer, J. & Verdel, A., 2007. Retrieval of reflections from seismic background-noise measurements, Geophys. Res. Lett., 34(4).

Draganov, D., Campman, X., Thorbecke, J., Verdel, A. & Wapenaar, K., 2009. Reflection images from ambient seismic noise, Geophysics, 74(5), A63–A67.

Dziewonski, A., Bloch, S. & Landisma, M., 1969. A technique for analysis of transient seismic signals, Bull. seism. Soc. Am., 59(1), 427–444.

Fan, Y. & Snieder, R., 2009. Required source distribution for interferometry of waves and diffusive fields, Geophys. J. Int., 179(2), 1232–1244.

Gerstoft, P., Shearer, P.M., Harmon, N. & Zhang, J., 2008. Global P, PP, and PKP wave microseisms observed from distant storms, Geophys. Res. Lett., 35(23), L23306, doi:10.1029/2008GL036111.

James, D.E., Niu, F.L. & Rokosky, J., 2003. Crustal structure of the Kaapvaal craton and its significance for early crustal evolution, Lithosphere, 71(2-4), 413–429.

Kennett, B.L.N., 1984. Guided wave-propagation in laterally varying media. 1. Theoretical development, Geophys. J.R. astr. Soc., 79(1), 235–255.

Kennett, B.L.N. & Mykkeltveit, S., 1984. Guided wave-propagation in laterally varying media. 2. Lg-waves in northwestern Europe, Geophys. J. R. astr. Soc., 79(1), 257–267.

Koper, K.D., De Foy, B. & Benz, H.M., 2009. Composition and variation of noise recorded at the Yellowknife seismic array, 1991–2007, J. geophys. Res., 114, B10310.

Levshin, A.L. & Ritzwoller, M.H., 2001. Automated detection, extraction, and measurement of regional surface waves, Pure appl. Geophys., 158(8), 1531–1545.

Lin, F.C., Moschetti, M.P. & Ritzwoller, M.H., 2008. Surface wave tomography of the western United States from ambient seismic noise: Rayleigh and love wave phase velocity maps, Geophys. J. Int., 173(1), 281–298.

Ma, S., Prieto, G.A. & Beroza, G.C., 2008. Testing community velocity models for southern California using the ambient seismic field, Bull. seism. Soc. Am., 98(6), 2694–2714.

Mercier, J.P., Bostock, M.G., Audet, P., Gaherty, J.B., Garnero, E.J. & Revenaugh, J., 2008. The teleseismic signature of fossil subduction: northwestern Canada, J. geophys. Res., 113(B4), 16, B04308, doi:10.1029/2007JB005127.

Mori, J. & Helmberger, D., 1996. Large-amplitude Moho reflections (SmS) from landers aftershocks, southern California, Bull. seism. Soc. Am., 86(6), 1845–1852.

Prieto, G.A. & Beroza, G.C., 2008. Earthquake ground motion prediction using the ambient seismic field, Geophys. Res. Lett., 35(14).

Rost, S. & Thomas, C., 2002. Array seismology: methods and applications, Rev. Geophys., 40(3), 27, 1008, doi:10.1029/2000RG000100.

Roux, P., Sabra, K.G., Gerstoft, P., Kuperman, W.A. & Fehler, M.C., 2005. P-waves from cross-correlation of seismic noise, Geophys. Res. Lett., 32(19), L19303, doi:10.1029/2005GL023803.

Shapiro, N.M., Campillo, M., Stehly, L. & Ritzwoller, M.H., 2005. High-resolution surface-wave tomography from ambient seismic noise, Science, 307(5715), 1615–1618.

Snieder, R., 2004. Extracting the Green's function from the correlation of coda waves: a derivation based on stationary phase, Phys. Rev. E, 69(4), 046610.

Stead, R.J. & Helmberger, D.V., 1988. Numerical-analytical interfacing in two dimensions with applications to modeling NTS seismograms, Pure appl. Geophys., 128(1–2), 157–193.

Stehly, L., Campillo, M. & Shapiro, N.M., 2006. A study of the seismic noise from its long-range correlation properties, J. Geophys. Res., 111, B10306, doi:10.1029/2005JB004237.

Stehly, L., Fry, B., Campillo, M., Shapiro, N.M., Guilbert, J., Boschi, L. & Giardini, D., 2009. Tomography of the alpine region from observations of seismic ambient noise, Geophys. J. Int., 178(1), 338–350.

Viejo, G.F. & Clowes, R.M., 2003. Lithospheric structure beneath the Archaean slave province and proterozoic Wopmay Orogen, northwestern Canada, from a lithoprobe refraction/wide-angle reflection survey, Geophysical Journal International, 153: 1–19. doi: 10.1046/j.1365-246X.2003.01807.x

Wapenaar, K., 2004. Retrieving the elastodynamic Green's function of an arbitrary inhomogeneous medium by cross correlation, Phys. Rev. Lett., 93(25), 254301.

Wapenaar, K., 2006. Green's function retrieval by cross-correlation in case of one-sided illumination, Geophys. Res. Lett., 33(19), L19304, doi:10.1029/2006GL027747.

Weaver, R.L. & Lobkis, O.I., 2001. Ultrasonics without a source: thermal fluctuation correlations at MHz frequencies, Phys. Rev. Lett., 87(13), 4, 134301.

Yang, Y.J. & Ritzwoller, M.H., 2008. Characteristics of ambient seismic noise as a source for surface wave tomography, Geochem. Geophys. Geosyst., 9, Q02008, doi:10.1029/2007GC001814.

Yang, Y.J., Ritzwoller, M.H., Levshin, A.L. & Shapiro, N.M., 2007. Ambient noise Rayleigh wave tomography across Europe, Geophys. J. Int., 168(1), 259–274.

Yao, H.J., Van Der Hilst, R.D. & De Hoop, M.V., 2006. Surface-wave array tomography in Se Tibet from ambient seismic noise and two-station analysis. I. Phase velocity maps, Geophys. J. Int., 166(2), 732–744.

Zhang, J., Gerstoft, P. & Shearer, P.M., 2009. High-frequency P-wave seismic noise driven by ocean winds, Geophys. Res. Lett., 36, L09302, doi:10.1029/2009GL037761.

Zheng, S.H., Sun, X.L., Song, X.D., Yang, Y.J. & Ritzwoller, M.H., 2008. Surface wave tomography of China from ambient seismic noise correlation, Geochem. Geophys. Geosyst., 9, Q05020, doi:10.1029/2008GC001981.

Zhu, L.P. & Helmberger, D.V., 1996. Advancement in source estimation techniques using broadband regional seismograms, Bull. seism. Soc. Am., 86(5), 1634–1641.

Zhu, L.P. & Rivera, L.A., 2002. A note on the dynamic and static displacements from a point source in multilayered media, Geophys. J. Int., 148(3), 619–627.

# Chapter 4

# Spurious velocity changes caused by temporal variations in ambient noise frequency content

This chapter has been published as:

Zhan, Z., V. C. Tsai, and R. W. Clayton (2013). Spurious velocity changes caused by temporal variations in ambient noise frequency content. Geophys. J. Int., 194 (3): 1574-1581. doi: 10.1093/gji/ggt170

## 4.1 Abstract

Ambient seismic noise cross correlations are now being used to detect temporal variations of seismic velocity, which are typically on the order of 0.1%. At this small level, temporal variations in the properties of noise sources can cause apparent velocity changes. For example, the spatial distribution and frequency content of ambient noise have seasonal variations due to the seasonal hemispherical shift of storms. Here we show that if the stretching method is used to measure time shifts, then the temporal variability of noise frequency content causes apparent velocity changes due to the changes in both amplitude and phase spectra caused by waveform stretching. With realistic seasonal variations of frequency content in the Los Angeles Basin, our numerical tests produce about 0.05% apparent velocity change, comparable to what

Meier et al. (2010) observed in the Los Angeles Basin. We find that the apparent velocity change from waveform stretching depends on time windows and station-pair distances, and hence it is important to test a range of these parameters to diagnose the stretching bias. Better understanding of spatiotemporal noise source properties is critical for more accurate and reliable passive monitoring.

## 4.2 Introduction

Using seismic waves to monitor temporal velocity changes in the Earth provides important information about a variety of geophysical processes, including earthquake stress cycles (e.g., Niu et al., 2008), fault-zone damage and healing (e.g., Li et al., 1998; Vidale and Li, 2003; Peng and Ben-Zion, 2005; Peng and Ben-Zion, 2006), volcanic eruptions (e.g., Grêt et al., 2005), and fluid movement (e.g., Niu et al., 2003). Direct and coda waves from natural and active repeating sources have been used for different problems (e.g., Poupinet et al., 1984; Niu et al., 2003; Rubinstein et al., 2007; Niu et al., 2008; Wang et al., 2008). However, application of these active monitoring approaches is limited by the lack of continuous or frequent high-quality repeating sources. With the rapid progress of noise cross correlation methods in the last decade, a passive monitoring method using ambient seismic noise has become popular. The basic idea is that the noise cross-correlation function (NCF) between two stations converges toward the Green's function between the stations, which is the response at one station if a source is placed at the other station. This allows us to treat seismic stations as continuous virtual repeating sources. The temporal resolution is only limited by the time required to get converged/stable NCFs (Hadziioannou et al., 2009). This passive monitoring method has been widely applied in regions with volcanoes or major earthquakes to detect velocity changes before and after volcanic eruptions (e.g., Sens-Schonfelder and Wegler, 2006; Brenguier et al., 2008b; Duputel et al., 2009), earthquakes (e.g., Brenguier et al., 2008a; Xu and Song, 2009; Zaccarelli et al., 2011; Minato et al., 2012) or slow slip events (Rivet et al., 2011). Using the passive monitoring method, Meier et al. (2010) detect seasonal velocity changes within the Los Angeles Basin (with higher velocities in summer than in winter) and suggest that two possible reasons are hydrological and/or thermoelastic variations. However, Tsai (2011) shows that neither of the two models is likely to explain the observed velocity variations.

The observed temporal velocity changes by passive monitoring are typically small, of the order of 0.1% (e.g., Brenguier et al., 2008a; Meier et al., 2010). Many technical factors including convergence and quality of the NCFs, spatiotemporal variability of noise sources, and method to compare waveforms can introduce potentially comparable bias. Clarke et al. (2011) show that a certain NCF signal-to-noise (SNR) threshold is required to make reliable measurements with <0.1% accuracy. Using laboratory experiments, Hadziioannou et al. (2009) demonstrate that passive monitoring does not require accurate reconstruction of the Green's functions, but instead only requires the relative stability of the background noise structure. Despite this relaxed constraint, passive monitoring can have problems because in real geophysical problems, the noise structure is usually highly variable. For example, due to the seasonal shift of storm activity between the northern and southern hemispheres, the spatial distribution of noise sources is also seasonal. Before and after major earthquakes or volcanic eruptions, there are usually significantly different levels of seismic activity (e.g., aftershocks and volcanic tremor), whose signals are hard to remove completely from ambient seismic noise before cross correlation. In past studies, their effects were usually evaluated by examining consistency between the positive and negative sides of the NCFs (e.g., Brenguier et al., 2008a) or over station pairs with different azimuths (e.g., Meier et al., 2010). In this paper, we concentrate on another largely ignored factor, the temporal variability of noise frequency content, which occurs at different time scales. For example, seasonal or even multi-decadal variations in storm activity cause long-term variations in noise frequency content at a global scale (e.g., McNamara and Buland, 2004; Aster et al., 2008). Increased earthquake or volcanic/non-volcanic tremor activity can cause changes in frequency content at shorter time scales. For example, Duputel et al. (2009) report a drift of dominant frequency around periods of volcanic eruption due to increased volcanic tremor. However, the effect of variable frequency content on passive monitoring is still not well quantified.

The sensitivity of NCFs to seismic velocity is from travel time information contained in their phase spectra. Therefore methods that mix amplitude and phase spectra potentially cause biases in velocity due to variations in the amplitude spectrum. Since the passive monitoring method is the same as the active monitoring method after preparing the NCFs, most passive studies adopt the same waveform comparison methods such as the doublet method (also known as moving window cross spectral method, MWCS, Poupinet et al., 1984). The doublet method measures the travel time difference between two waveforms in each time window by fitting the phase differences in the frequency domain. Theoretically, as long as appropriate windowing functions are used, this approach separates the amplitude spectrum and phase spectrum before making the measurements, hence is likely less affected by the change of frequency content. In another recently proposed method, called the stretching method, the time axis on one waveform is stretched to achieve the best cross correlation with another waveform. The best-fitting stretching ratio is then taken as an estimate of the relative velocity change. Theoretical and laboratory work show that the stretching method is more stable to fluctuations in noise compared to the traditional doublet method (Hadziioannou et al. 2009), and it has started to be widely used in passive monitoring applications (e.g., Sens-Schonfelder and Wegler, 2006; Duputel et al., 2009; Meier et al., 2010; Minato et al., 2012). In this paper we concentrate on this methodology's bias due to changes in frequency content. In section 4.3 we will first theoretically illustrate the stretching method's problem of mixing amplitude and phase information during waveform comparison. Then in section 4.4, as an example, we will show that realistic changes in NCF frequency content within the Los Angeles Basin could cause changes comparable to those observed by Meier et al. (2010). Lastly, we will discuss how to diagnose this bias.

## 4.3 The stretching method and the effect of variable NCF amplitude spectrum

### 4.3.1 Summary of the stretching method in time and frequency domains

The stretching method builds on the fact that the relative time shift between two waveforms due to a small uniform velocity change is proportional to the travel time. Suppose we have two NCFs, a reference NCF $u_r(t)$ and a current NCF $u_c(t)$, and we use the stretching method to measure the relative velocity change $\varepsilon_v = \delta v/v$. The stretching method will first stretch the current NCF assuming a relative velocity change of $\varepsilon$,

$$u_c(t;\varepsilon) \equiv u_c(t(1-\varepsilon)) \tag{4.1}$$

Then the stretched waveform $u_c(t;\varepsilon)$ is correlated with the reference waveform $u_r(t)$ in the time domain:

$$C(\varepsilon) = \frac{\int_{t_1}^{t_2} u_r(t)u_c(t;\varepsilon)\mathrm{d}t}{\sqrt{\int_{t_1}^{t_2} u_r^2(t)\mathrm{d}t \int_{t_1}^{t_2} u_c^2(t;\varepsilon)\mathrm{d}t}} \tag{4.2}$$

where $t_1$ and $t_2$ define the time window. The stretching method grid-searches over $\varepsilon$ to find the apparent velocity change $\varepsilon_{max}$ that maximizes $C(\varepsilon)$ as an estimate of the relative velocity change $\varepsilon_v$.

The above waveform stretching and correlation are usually conducted entirely in the time domain. However, to show how different amplitude spectra affect the measurement, here we restate the method in the frequency domain. Letting $U_r(\omega)$ and $U_c(\omega)$ to be the Fourier transforms of $u_r(t)$ and $u_c(t)$, respectively, then

$$U_r(\omega) = F\{u_r(t)\} = A_r(\omega)e^{i\varphi_r(\omega)} \tag{4.3}$$

$$U_c(\omega) = F\{u_c(t)\} = A_c(\omega)e^{i\varphi_c(\omega)} \tag{4.4}$$

where $A_r(\omega)$ and $A_c(\omega)$ are the amplitude spectra, $\varphi_r(\omega)$ and $\varphi_c(\omega)$ are the phase spectra. Taking the Fourier transform of Eq. (4.1), then waveform stretching in the frequency domain can be written as

$$U_c(\omega;\varepsilon) = \frac{1}{1-\varepsilon}U_c(\frac{\omega}{1-\varepsilon}) \approx (1+\varepsilon)U_c(\omega(1+\varepsilon)) = (1+\varepsilon)A_c(\omega(1+\varepsilon))e^{i\varphi_c(\omega(1+\varepsilon))} \tag{4.5}$$

where the approximation applies to $\varepsilon \ll 1$. Note that both the amplitude and phase spectra get stretched. For general dispersive waves with wavenumer $k$ and propagation distance of $x$, we can further simplify the form of the phase spectrum:

$$\varphi(\omega(1+\varepsilon)) = k(\omega(1+\varepsilon)) \cdot x \approx kx + \frac{\partial k}{\partial \omega}\omega\varepsilon x = kx(1+\frac{\omega\varepsilon}{kv_g}) = \varphi(\omega)(1+\frac{c}{v_g}\varepsilon) \tag{4.6}$$

where $c$ is phase velocity and $v_g$ is group velocity. For non-dispersive waves $c = v_g$, and Eq. (4.6) simplifies to $\varphi(\omega(1+\varepsilon)) = \varphi(\omega)(1+\varepsilon)$. With the simplifications of Eq. (4.5) and (4.6) above, Eq. (4.2) showing the correlation of the reference waveform and stretched current waveform can be rewritten as:

$$
\begin{aligned}
C(\varepsilon) &= \frac{\int_{-\infty}^{+\infty} U_r(\omega) U_c(\omega;\varepsilon) \mathrm{d}\omega}{\sqrt{\int_{-\infty}^{+\infty} U_r^2(\omega)\mathrm{d}\omega \int_{-\infty}^{+\infty} U_c^2(\omega;\varepsilon)\mathrm{d}\omega}} \\
&= \frac{\int_{-\infty}^{+\infty} A_r(\omega) A_c(\omega(1+\varepsilon)) e^{i[\varphi_c(\omega(1+\varepsilon))-\varphi_r(\omega)]}\mathrm{d}\omega}{\sqrt{\int_{-\infty}^{+\infty} A_r^2(\omega)\mathrm{d}\omega \int_{-\infty}^{+\infty} A_c^2(\omega(1+\varepsilon))\mathrm{d}\omega}}
\end{aligned} \tag{4.7}
$$

$C(\varepsilon)$and $\varepsilon_{max}$ depend on the forms of both the amplitude spectra $A_r(\omega)$, $A_c(\omega)$, and wave dispersions in the form of phase spectra $\varphi_r(\omega)$ and $\varphi_c(\omega)$.

### 4.3.2 Bias of the stretching method due to changes in the amplitude spectra

Since we are interested in the bias effect caused only by a variable amplitude spectrum, here we simplify $C(\varepsilon)$ by considering a special case that $u_r(t)$ and $u_c(t)$ have the same phase spectrum $\varphi(\omega)$ (i.e., no velocity variation). A stable measurement method should recover $\varepsilon_v = 0$ in this case. For this assumption, Equation (4.7) simplifies to

$$
C(\varepsilon) = \frac{\int_{-\infty}^{+\infty} A_r(\omega) A_c(\omega(1+\varepsilon)) e^{i\frac{c}{v_g}\varepsilon\varphi(\omega)}\mathrm{d}\omega}{\sqrt{\int_{-\infty}^{+\infty} A_r^2(\omega)\mathrm{d}\omega \int_{-\infty}^{+\infty} A_c^2(\omega(1+\varepsilon))\mathrm{d}\omega}} \tag{4.8}
$$

To decompose the effects of the amplitude and phase spectra, we first look at the result of the simplest non-dispersive case $\varphi(\omega) = 0$ so that $C(\varepsilon)$ is only controlled by the amplitude spectra $A_r(\omega)$ and $A_c(\omega)$:

$$
C(\varepsilon) = \frac{\int_{-\infty}^{+\infty} A_r(\omega) A_c(\omega(1+\varepsilon))\mathrm{d}\omega}{\sqrt{\int_{-\infty}^{+\infty} A_r^2(\omega)\mathrm{d}\omega \int_{-\infty}^{+\infty} A_c^2(\omega(1+\varepsilon))\mathrm{d}\omega}} \tag{4.9}
$$

It is clear that the $C(\varepsilon)$ in this case is just the correlation function between the amplitude spectra $A_r(\omega)$ and stretched $A_c(\omega)$ in the frequency domain, which in general does not have $\varepsilon_{max} = 0$ under our assumption of variable frequency content, i.e. $A_r(\omega) \neq A(\omega)$. More generally, for the non-dispersive case, $\varphi(\omega) = \omega t_0$, we calculate $\varepsilon_{max}(t_0)$ numerically, where $t_0$ is travel time of the wavelet. As an example, we assume that the reference $A_r(\omega)$ has a bell-shaped amplitude spectrum centered at 0.15 Hz and the current $A_c(\omega)$ has a stretched form of $A_r(\omega)$, and hence more high frequency energy, as shown in Figure 4.1A such that

$$A_c(\omega) = A_r(\frac{\omega}{1+\varepsilon_0}) \tag{4.10}$$

where $\varepsilon_0 = 20\%$ and the resulting $\varepsilon_{max}(t_0)$ is displayed in Figure 4.1B. As discussed above, when $t_0 = 0$s , $\varphi(\omega) = 0$, and $\varepsilon_{max}$ is the same as the optimal stretching ratio of the amplitude spectra so $\varepsilon_{max} = \varepsilon_0 = 20\%$. $\varepsilon_{max}(t_0)$ decays rapidly when $t_0$ increases from 0 s due to the extra $i\frac{c}{v_g}\varepsilon\varphi(\omega)$ term in the integrand of $C(\varepsilon)$. However, up to $t_0 = 30$s, the estimated $\varepsilon_{max}$ is still of the order of 0.1%, comparable to the observed relative velocity changes in most real-data applications of the passive monitoring technique. Figure 4.1B also shows that the maximum cross-correlation coefficients $C(\varepsilon_{max})$ are all larger than 0.9, a general threshold for most real-data applications. This means that high cross correlation values do not guarantee reliable measurements. Figure 4.1C displays example reference and current waveforms for $t_0$=20s, for which there is an apparent velocity increase of about 0.2%.

In this section, we have demonstrated that the stretching method changes the phase spectrum as well as the amplitude spectrum during measurements, and the amplitude spectrum contributes to the waveform correlation. This causes a bias in the estimate of the relative velocity change. In our simple synthetic tests where only the amplitude spectrum changes, the stretching method does not recover $\varepsilon_v = 0$, but instead produces systematic bias.

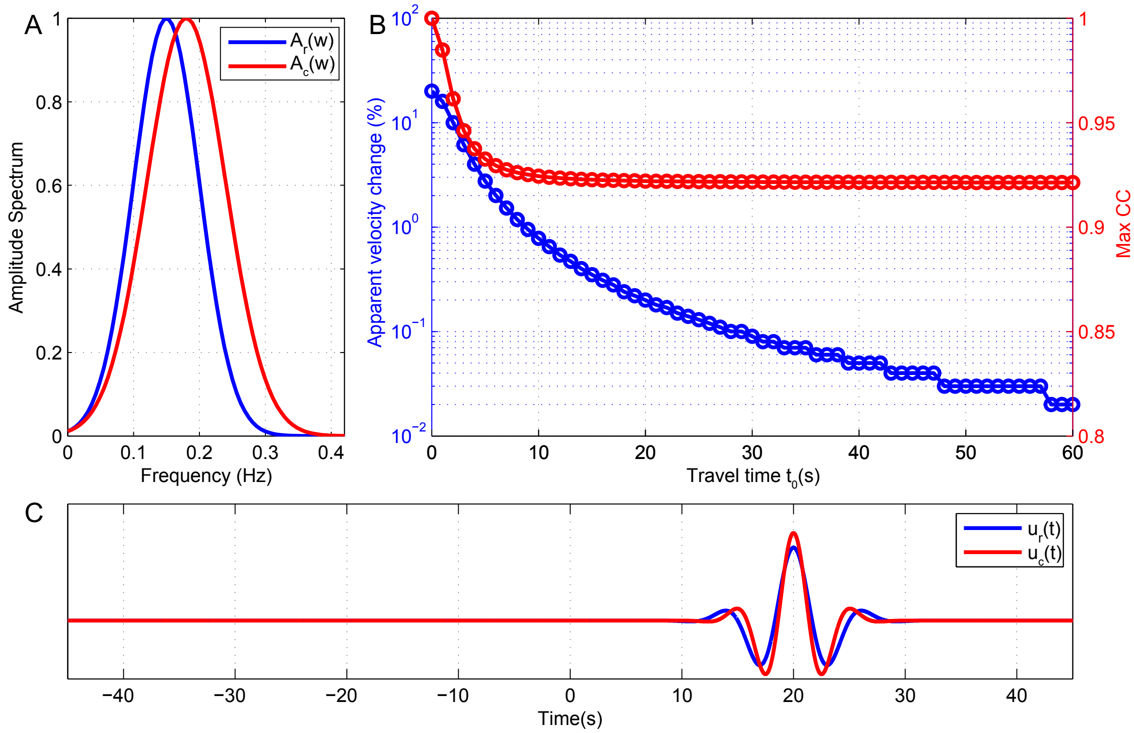


Figure 4.1: Numerical test of apparent velocity change $\varepsilon_{max}(t_0)$ caused by stretching of the NCF amplitude spectrum. (A) The reference NCF amplitude spectrum $A_r(\omega)$ has a Gaussian functional form with a center frequency of 0.15 Hz and $\sigma = 0.5$ Hz. The current NCF amplitude spectrum $A_c(\omega)$ is stretched from $A_r(\omega)$ by 20% to have more high frequency energy. (B) The blue line indicates the apparent velocity change $\varepsilon_{max}(t_0)$ calculated numerically using the stretching method. The red line shows the corresponding maximum cross correlation coefficients between the reference and current waveforms. Note that at $t_0 = 0$ s, the relative velocity change is 20%, the same as the stretching ratio between the input NCF amplitude spectra, and the maximum correlation value is 1.0. (C) Example waveforms of the reference NCF and current NCF at $t_0 = 20$ s, corresponding to a relative velocity change of about 0.2%.

## 4.4 Bias due to seasonal variation of noise frequency content in the Los Angeles Basin

Real ambient seismic noise and NCFs have more complicated temporal variations of frequency content than that discussed in section 4.3.2. In this section, we will use more realistic examples with data from the Los Angeles Basin to evaluate the bias caused by the frequency content change in the stretching method.

The frequency content of ambient noise at stations within USArray is now routinely calculated by IRIS for quality control of data. Raw noise spectra are calculated using the method of McNamara and Buland (2004) for overlapping half-hour windows throughout the day and presented as probability density functions (PDFs). Each day's power spectrum is the mode of the spectral values of the half-hour windows. Taking DEC, a broadband station at the edge of the LA basin as an example, we display its daily noise PDF between 2004 and 2011 in Figure 4.2A. The most obvious temporal variation in Figure 4.2A is the seasonal pattern, with stronger noise in winter and weaker noise in summer, probably caused by the seasonal hemispherical shift of storms (e.g., Stehly et al., 2006; Aster et al., 2008). Figure 4.2B shows the averaged power spectra for a whole year, winter only (December, January and February) and summer only (June, July and August), respectively. In addition to the absolute noise level changes, the shape of the spectrum also changes. For example, the differences between winter and summer in the power spectrum at $T<4$ s are much less than those at $T\approx 8$ s.

In addition to being affected by the raw ambient noise levels, NCFs are also affected by a number of pre-processing steps. Here we follow common procedures (e.g., Bensen et al., 2007; Meier et al., 2010; Zhan et al., 2011) to calculate the NCF for station pair WTT-LCG inside the Los Angeles Basin as an example. We use continuous broadband vertical-component data from 2003 to 2011, remove instrumental

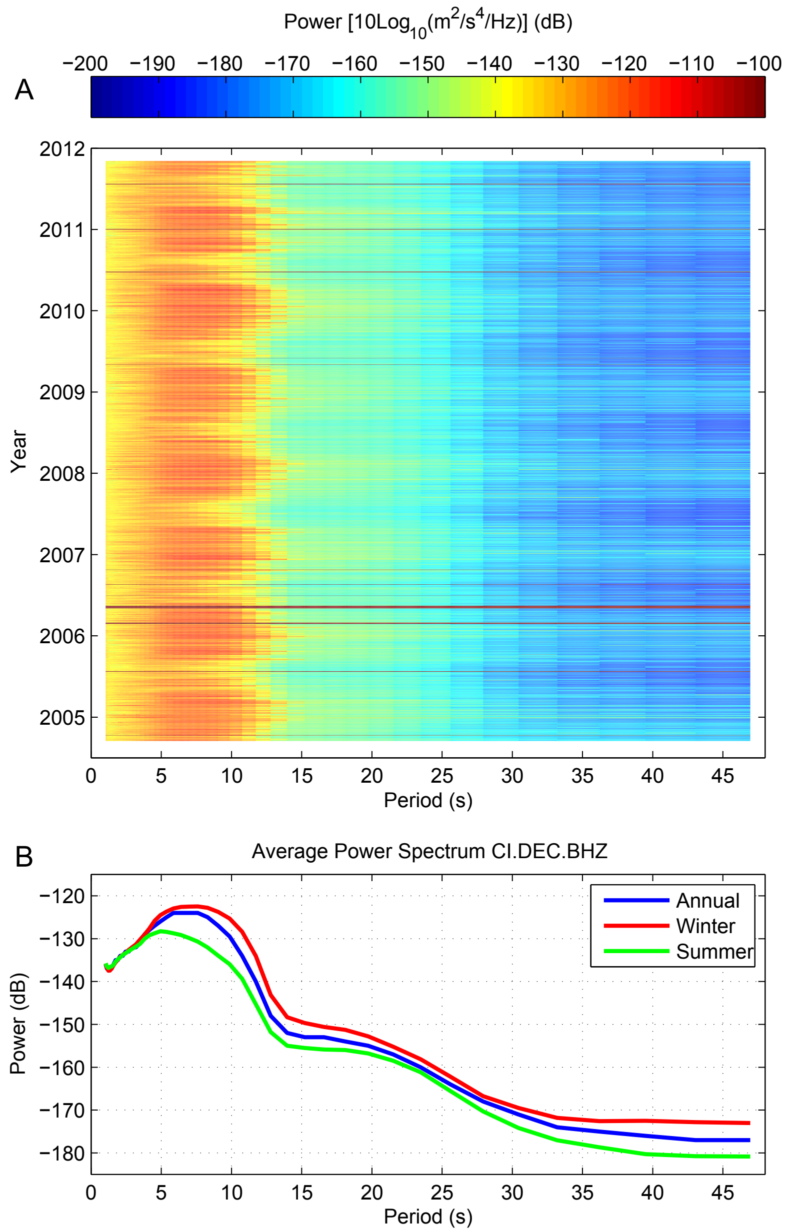


Figure 4.2: Temporal variability of raw noise frequency content. (A) Temporal variations in the noise power spectrum from 2004 to 2011 at station DEC. The dominant seasonal pattern shows higher noise level in winter and lower noise level in summer. Occasional dark red horizontal bands are due to gaps in data or instrument problems. (B) The blue line indicates the average noise power spectrum with the strongest peak at the secondary microseism period of 7 s. The red and green lines display the average spectra for winter and summer, respectively. Note that not only the absolute noise level changes, but the shape of the spectrum also changes.

responses and cut the data into one-hour segments. To remove the effect of earthquakes, we first filter the original seismograms between 15 s and 50 s to emphasize the surface waves of earthquakes and then calculate envelope functions. The inverse of these smoothed envelope functions multiply the corresponding seismograms to down-weight the earthquake signals. We also tested the effect of using one-bit normalization, and the resulting NCFs are similar in waveforms and spectra. We chose to present only the results for envelope weighting because its effect on waveforms is better understood than one-bit normalization. After envelope down-weighting, we then apply spectral whitening to broaden the frequency band of the NCFs. Finally, the two stations' waveforms are cross correlated at 1 hour intervals and stacked with a 60-day moving window and with an overlap of 30 days (Figure 4.3). Due to the shallow sediment layer in the Los Angeles Basin, the direct wave-train between the two stations can be as slow as 0.5 km/s (Figure 4.3A). The 60-day NCFs show high signal-to-noise ratios and good convergences, although small seasonal variability of the NCF waveforms is visible (Figure 4.3B). The amplitude spectra of the 60-day NCFs have even more obvious seasonal patterns (Figure 4.4A). To highlight the variability of the NCF frequency content, we calculate the standard deviations of the amplitude spectra for each frequency throughout the years (Figure 4.4B). The three maxima of the standard deviations at T= 5 s, 8 s and 10 s mark the three period bands with the strongest temporal variations (three colored squares in Figure 4.4B). To further examine the phases of these variations, the time series of these three periods' amplitude spectra are displayed in Figure 4.4C. They all show very strong seasonality, which is also supported by the dominant 1-year peaks in period analyses of all frequencies' amplitude spectra time series (Figure 4.4D). Among the three periods with the largest variations, the T=5 s band is stronger in summer and weaker in winter by more than 50%, while the T=10 s band shows the opposite trend. This means that although the absolute raw noise level is lower in summer for Southern California, the steps of pre-processing and calculating NCFs, including the temporal normalization and spectral whitening, do not remove the frequency content change of the raw noise, but produce the seesaw-style oscillating NCF amplitude spectrum. As pointed out by Tsai and Moschetti (2010), this is probably due to the presence of incoherent noise in the raw noise record. While the processing including spectral whitening is applied to the whole noise, cross correlations and NCFs only highlight the coherent part, whose spectrum is still not flat. Depending on the fraction of coherent noise and incoherent noise, the final NCFs may have the temporal variations of frequency content as observed (Figure 4.4).

With the more realistic oscillating NCF spectrum as observed in the LA Basin, we conduct a similar numerical test of apparent velocity change as in section 4.3 with the same phase spectrum but different amplitude spectra. As shown in Figure 4.5A, we set the reference NCF amplitude spectrum $A_r(\omega)$ to be the average NCF amplitude spectrum in winter, and set the current NCF amplitude spectrum $A_c(\omega)$ to be the average NCF amplitude spectrum in summer (see also Figure 4.4 for comparison). As previously described, the $A_c(\omega)$ spectrum has more high frequency energy. The resulting apparent velocity change $\varepsilon_{max}(t_0)$ as shown in Figure 4.5B has a similar shape to, but smaller amplitude than Figure 4.1B. It causes 0.05% apparent velocity increase up to $t_0 = 30\,\mathrm{s}$ and the maximum cross correlation coefficients are all larger than 0.9. These values are comparable to observations made by Meier et al. (2010). Since the distance between station WTT and LCG is about 12 km, wavelets with $t_0 = 30$s are well within the coda-wave window defined by most studies that assume a minimum velocity of 1 km/s (e.g., Meier et al. 2010). Additional numerical tests were also performed on smoother synthetic amplitude spectra with similar results as long as the fractional changes in spectra were comparable. In most real data applications, the stretching method is applied to NCF coda waves that consist of a series of scattered wavelets. In this study, we have chosen to examine each individual

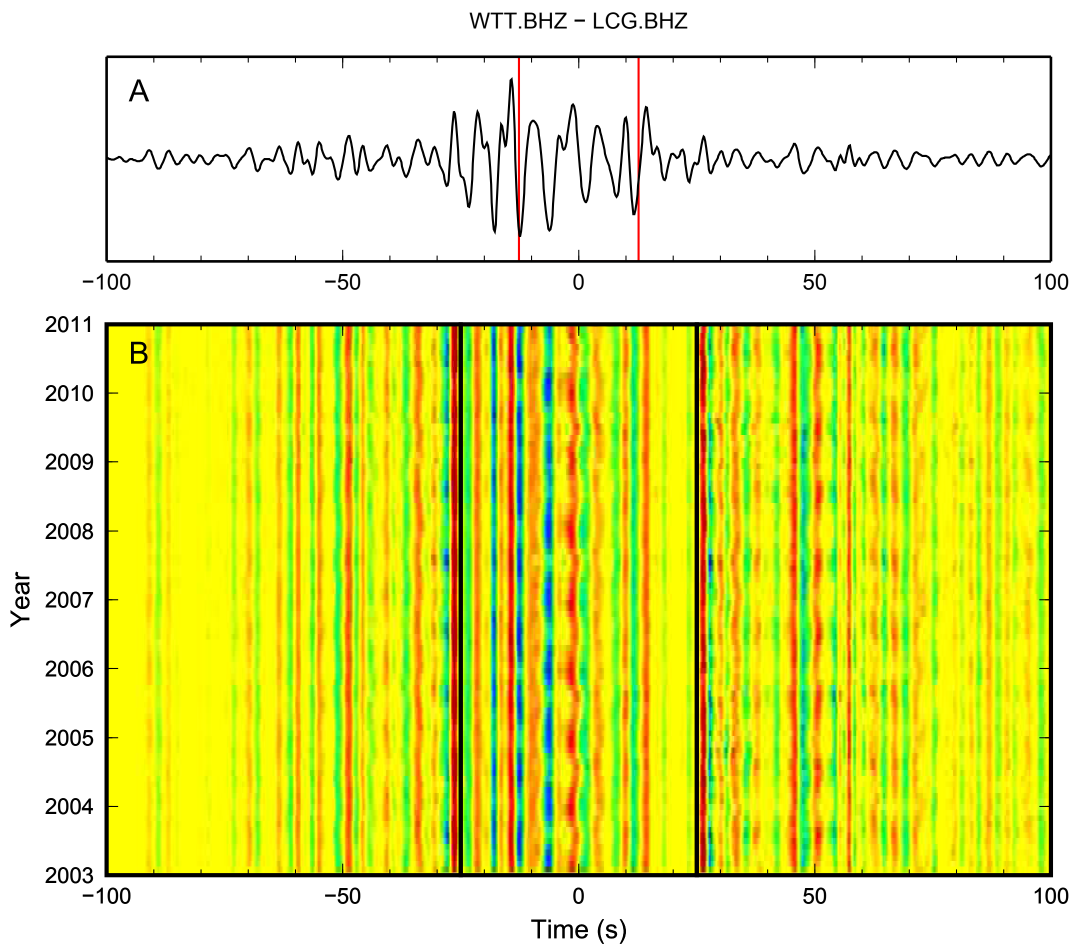


Figure 4.3: Noise cross correlation functions between WTT and LCG. (A) The stacked NCF between 2003 and 2011. The red lines mark the travel times for a wave speed of 1 km/s. Due to the shallow sediment layer, the direct wave-train lasts longer, corresponding to a wave speed of about 0.5 km/s. (B) The NCFs stacked every 60 days with 30 days overlapping show good signal-to-noise ratios and high coherence. Slight seasonal variations of the NCF waveforms can be observed. Different colorscales are used for direct waves and coda waves to highlight waveform details.

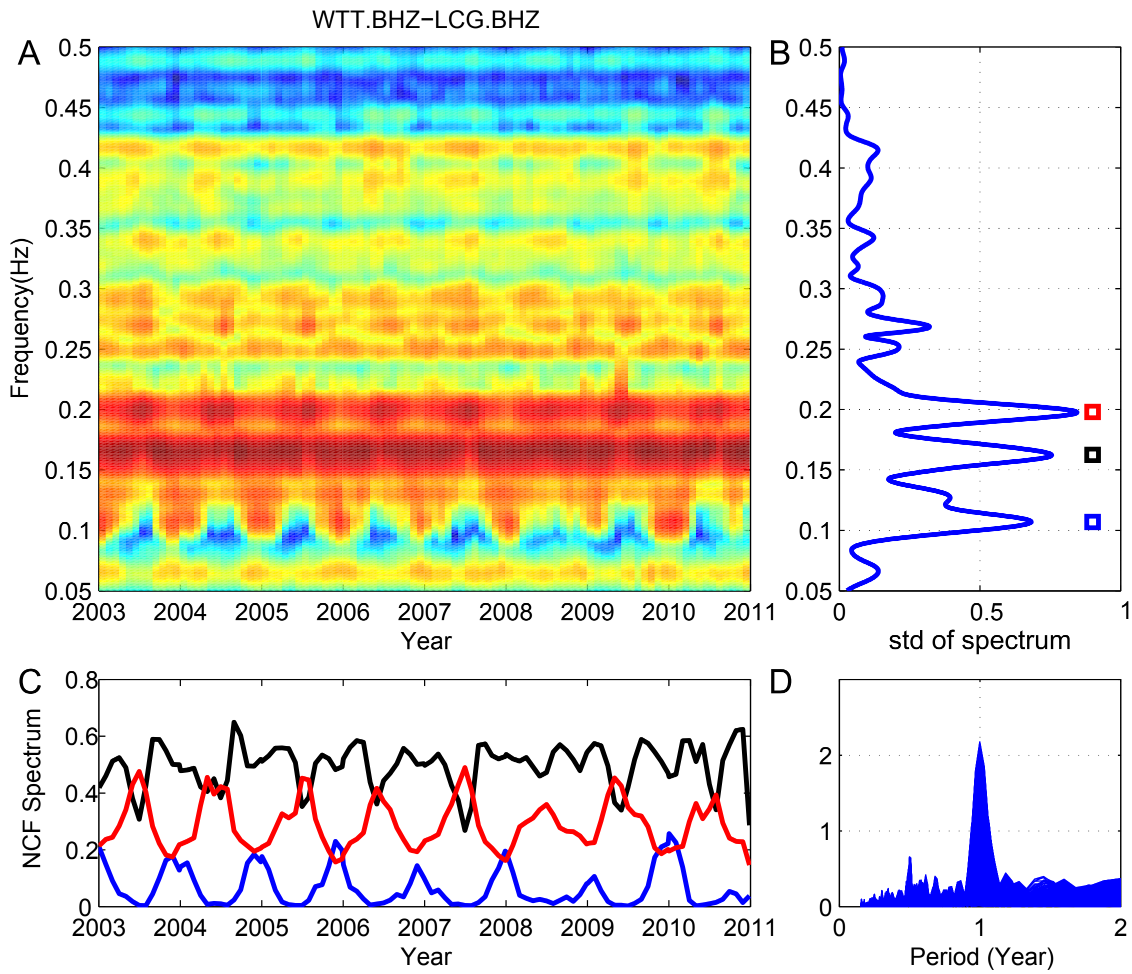


Figure 4.4: Temporal variability of NCF frequency content. (A) Amplitude spectra of the 60-day NCFs between 2003 and 2011 show clear seasonal patterns. (B) Standard deviation of the temporal variation of the NCF spectrum for each frequency. The three colored squares at the maxima mark the three period bands with the strongest temporal variations, and the corresponding time series of amplitude spectra are shown in (C) with different colors, respectively. (D) displays period analyses for all frequencies' temporal variations of amplitude spectra.

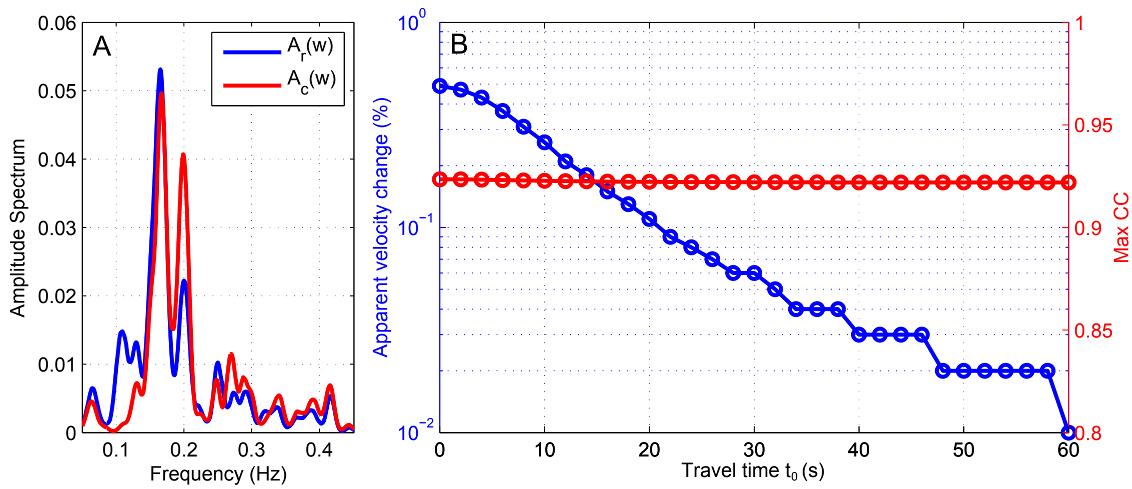


Figure 4.5: Similar numerical test of apparent velocity change $\varepsilon_{max}(t_0)$ as in Figure 4.1, but with the realistic NCF amplitude spectrum from the Los Angeles Basin. (A) The reference and current NCF amplitude spectra, $A_r(\omega)$ and $A_c(\omega)$ are set to be the average WTT-LCG NCF spectra in winter and summer, respectively. Note that $A_c(\omega)$ has more high frequency energy. (B) The blue line indicates the apparent velocity change $\varepsilon_{max}(t_0)$ calculated numerically using the stretching method. The red line shows the corresponding maximum cross correlation coefficients between the reference and current waveforms. Note that at $t_0 = 30\,\mathrm{s}$, the relative velocity change is 0.05%, comparable to the values measured in the Los Angeles Basin by Meier et al. (2010), and the maximum correlation value is >0.9.

wavelet at different travel times, rather than the combined coda, because it is easier to understand the bias effect for an individual wavelet and the effect on the whole coda can be understood by combining the individual wavelet results. We also note that for the same change in amplitude spectra, our results are the same, whether these changes occur seasonal, daily, or of any other time scale.

The numerical tests also suggest potential ways to diagnose this bias due to change in frequency content. As shown in Figure 4.1B and 4.5B, the apparent velocity change $\varepsilon_{max}(t_0)$ decays with increasing $t_0$, which means that, for a single NCF, the late part of the NCFs will produce smaller relative velocity changes. This trend is the opposite of what is expected from real velocity changes because late arrivals are more sensitive with more accumulated effect (Snieder et al., 2002; Brenguier et al., 2008a). The decay of $\varepsilon_{max}(t_0)$ with increasing $t_0$ also predicts that longer station pairs have smaller relative velocity changes than closer pairs, also opposite to the expectation from real velocity changes. This seems to have been observed in the LA basin by Meier et al. (2010), where the observed seasonal velocity variations are only obvious at station pairs shorter than 30 km, and decays with increasing station pair distance. Meier et al. (2010) attribute this observation to lower NCF coherence at larger distances and reject the effect of variable noise sources by averaging over different time windows and station pairs with different azimuths. However, our numerical tests show that the bias due to change of frequency content is systematic for different time windows ($t_0$). As long as noise from different azimuths have similar trends in the temporal variations of frequency content (e.g., more high frequency noise in summer than in winter), which is a weak constraint, the bias is also systematic over all azimuths. This implies that the apparent velocity change cannot be diagnosed by taking averages of $\varepsilon_{max}$ measured from different station pairs and different time windows.

## 4.5 Conclusions

We have shown that the temporal variability of NCF frequency content causes apparent velocity changes if the stretching method is used to measure the time shifts. This is primarily due to the mixing effects that stretching has on amplitude and phase spectra, and hence on waveform correlation. The apparent velocity change depends on a few factors: dispersion, forms of amplitude spectra, and travel times of time windows. Our numerical tests show that the bias decays with travel time, and therefore is most severe for close station pairs and early parts of the NCFs. For realistic seasonal variability of frequency content in the LA Basin and travel times up to 30s, our test examples still produce 0.05% apparent velocity changes and >0.9 waveform correlation coefficients, comparable to what usually has been observed in previous passive monitoring studies. Since temporal variability of noise frequency content at different time scales can also be caused by the change of background seismic activity that accompanies major earthquakes, slow slip events (SSEs) or volcanic eruptions, it is important to check for this potential bias in future applications of passive monitoring. To diagnose this bias, time shifts measured from NCFs should be examined for dependence on travel times of time windows and distances of station pairs. The traditional cross-spectral doublet method may be free of this bias due to the separation of amplitude and phase spectra in the frequency domain before measuring time shifts.

## Acknowledgments

We thank Fan-Chi Lin and Dongzhou Zhang for helpful discussions. We thank the editor Michael Ritzwoller and two anonymous reviewers for their comments that improved the manuscript. The facilities of the Southern California Earthquake Data Center (SCEDC), and the Southern California Seismic Network (SCSN), were used for access to waveforms data required in this study. This work is partially supported by the NSF/EAR-0838247 and Southern California Earthquake Center (12064).

## References

Aster, R.C., McNamara, D.E., Bromirski, P.D., 2008. Multidecadal climate-induced variability in microseisms. Seismological Research Letters 79, 194-202.

Bensen, G.D., Ritzwoller, M.H., Barmin, M.P., Levshin, A.L., Lin, F., Moschetti, M.P., Shapiro, N.M., Yang, Y., 2007. Processing seismic ambient noise data to obtain reliable broad-band surface wave dispersion measurements. Geophysical Journal International 169, 1239-1260.

Brenguier, F., Campillo, M., Hadziioannou, C., Shapiro, N.M., Nadeau, R.M., Larose, E., 2008a. Postseismic relaxation along the San Andreas fault at Parkfield from continuous seismological observations. Science 321, 1478-1481.

Brenguier, F., Shapiro, N.M., Campillo, M., Ferrazzini, V., Duputel, Z., Coutant, O., Nercessian, A., 2008b. Towards forecasting volcanic eruptions using seismic noise. Nature Geoscience 1, 126-130.

Clarke, D., Zaccarelli, L., Shapiro, N., Brenguier, F., 2011. Assessment of resolution and accuracy of the Moving Window Cross Spectral technique for monitoring crustal temporal variations using ambient seismic noise. Geophysical Journal International 186, 867-882.

Duputel, Z., Ferrazzini, V., Brenguier, F., Shapiro, N., Campillo, M., Nercessian, A., 2009. Real time monitoring of relative velocity changes using ambient seismic noise at the Piton de la Fournaise volcano (La Réunion) from January 2006 to June 2007. Journal of Volcanology and Geothermal Research 184, 164-173.

Grêt, A., Snieder, R., Aster, R.C., Kyle, P.R., 2005. Monitoring rapid temporal change in a volcano with coda wave interferometry. Geophysical Research Letters 32, L06304.

Hadziioannou, C., Larose, E., Coutant, O., Roux, P., Campillo, M., 2009. Stability of monitoring weak changes in multiply scattering media with ambient noise correlation: Laboratory experiments. Journal of the Acoustical Society of America 125, 3688-3695.

Li, Y.-G., Vidale, J.E., Aki, K., Xu, F., Burdette, T., 1998. Evidence of shallow fault zone strengthening after the 1992 M7. 5 Landers, California, earthquake. Science 279, 217-219.

McNamara, D.E., Buland, R.P., 2004. Ambient noise levels in the continental United States. Bulletin of the Seismological Society of America 94, 1517-1527.

Meier, U., Shapiro, N.M., Brenguier, F., 2010. Detecting seasonal variations in seismic velocities within Los Angeles basin from correlations of ambient seismic noise. Geophysical Journal International 181, 985-996.

Minato, S., Tsuji, T., Ohmi, S., Matsuoka, T., 2012. Monitoring seismic velocity change caused by the 2011 Tohoku-oki earthquake using ambient noise records. Geophysical Research Letters 39, L09309.

Niu, F., Silver, P.G., Daley, T.M., Cheng, X., Majer, E.L., 2008. Preseismic velocity changes observed from active source monitoring at the Parkfield SAFOD drill site. Nature 454, 204-208.

Niu, F., Silver, P.G., Nadeau, R.M., McEvilly, T.V., 2003. Migration of seismic scatterers associated with the 1993 Parkfield aseismic transient event. Nature 426, 544-548.

Peng, Z., Ben-Zion, Y., 2006. Temporal changes of shallow seismic velocity around the Karadere-Düzce branch of the north Anatolian fault and strong ground motion. Pure and Applied Geophysics 163, 567-600.

Peng, Z., Ben-Zion, Y., 2005. Spatiotemporal variations of crustal anisotropy from similar events in aftershocks of the 1999 M7. 4 Izmit and M7. 1 Düzce, Turkey, earthquake sequences. Geophysical Journal International 160, 1027-1043.

Poupinet, G., Ellsworth, W., Frechet, J., 1984. Monitoring Velocity Variations in the Crust Using Earthquake Doublets: An Application to the Calaveras Fault, California. Journal of Geophysical Research 89, 5719-5731.

Rivet, D., Campillo, M., Shapiro, N.M., Cruz-Atienza, V., Radiguet, M., Cotte, N., Kostoglodov, V., 2011. Seismic evidence of nonlinear crustal deformation during a large slow slip event in Mexico. Geophysical Research Letters 38, L08308.

Rubinstein, J.L., Uchida, N., Beroza, G.C., 2007. Seismic velocity reductions caused by the 2003 Tokachi-Oki earthquake. Journal of Geophysical Research 112, B05315.

Sens-Schonfelder, C., Wegler, U., 2006. Passive image interferometry and seasonal variations of seismic velocities at Merapi Volcano, Indonesia. Geophysical Research Letters 33.

Snieder, R., Grêt, A., Douma, H., Scales, J., 2002. Coda wave interferometry for estimating nonlinear behavior in seismic velocity. Science 295, 2253-2255.

Stehly, L., Campillo, M., Shapiro, N.M., 2006. A study of the seismic noise from its long-range correlation properties. Journal of Geophysical Research-Solid Earth 111.

Tsai, V.C., 2011. A model for seasonal changes in GPS positions and seismic wave speeds due to thermoelastic and hydrologic variations. Journal of Geophysical Research 116, B04404.

Tsai, V.C., Moschetti, M.P., 2010. An explicit relationship between time-domain noise correlation and spatial autocorrelation (SPAC) results. Geophysical Journal International 182, 454-460.

Vidale, J.E., Li, Y.-G., 2003. Damage to the shallow Landers fault from the nearby Hector Mine earthquake. Nature 421, 524-526.

Wang, B., Zhu, P., Chen, Y., Niu, F., Wang, B., 2008. Continuous subsurface velocity measurement with coda wave interferometry. Journal of Geophysical Research 113, B12313.

Xu, Z.J., Song, X., 2009. Temporal changes of surface wave velocity associated with major Sumatra earthquakes from ambient noise correlation. Proceedings of the National Academy of Sciences 106, 14207-14212.

Zaccarelli, L., Shapiro, N., Faenza, L., Soldati, G., Michelini, A., 2011. Variations of crustal elastic properties during the 2009 L'Aquila earthquake inferred from cross-correlations of ambient seismic noise. Geophysical Research Letters 38, L24304.

Zhan, Z., Wei, S., Ni, S., Helmberger, D., 2011. Earthquake centroid locations using calibration from ambient seismic noise. Bulletin of the Seismological Society of America 101, 1438-1445.

# Chapter 5

# Ambient noise correlation on the Amery Ice Shelf, East Antarctica

## 5.1 Abstract

The structure of ice shelves is important for modeling the dynamics of ice flux from the continents to the oceans. While other, more traditional techniques provide many constraints, passive imaging with seismic noise is a complementary tool for studying and monitoring ice shelves. As a proof of concept, here we study noise cross-correlations and auto-correlations on the Amery Ice Shelf, East Antarctica. We find that the noise field on the ice shelf is dominated by energy trapped in a low velocity waveguide caused by the water layer below the ice. Within this interpretation, we explain spectral ratios of the noise cross-correlations as $P$-wave resonances in the water layer, and obtain an independent estimate of the water-column thickness, consistent with other measurements. For stations with low levels of incoherent noise, noise auto-correlations also provide similar results. High-frequency noise correlations also require a 50-m firn layer near the surface with $P$-wave velocity as low as 1 km/s. Our study may also provide insight for future planetary missions that involve seismic exploration of icy satellites such as Titan and Europa.

## 5.2 Introduction

Ice shelves are important interfaces between grounded ice sheets and oceans, and contribute to the majority of grounded ice loss either through basal melting or iceberg calving. Accurate modeling of ice shelf dynamics (e.g., sub-ice circulation and ice flow modeling) requires high-resolution ice drafts and water-column thicknesses, which are usually poorly constrained for ice shelves. Currently, ice drafts and water-column thicknesses are constrained mostly from digital elevation modeling (Fricker et al., 2005), tidal modeling (Hemer et al., 2006; Galton-Fenzi et al., 2008), and sparse active seismic surveys and drillings (Craven et al., 2009; McMahon and Lackie, 2006). It is therefore of interest whether other methods can contribute additional and/or better constraints. One method that has received little attention in cryospheric studies is passive imaging with ambient seismic noise. Passive imaging can be applied over large areas at a low cost and without direct sampling, and has been widely used to study crustal structure around the globe in recent years (e.g., Shapiro et al., 2005; Yao et al., 2006; Lin et al., 2008), including in Antarctica (Pyle et al., 2010). However, most of these studies are located in the interior of the continent and concentrate on the structure of the crust or upper mantle using long-period (T>5 s) surface waves. To our knowledge, there has not been any report of small-scale noise correlation on ice shelves. The reason for this may be twofold. First, due to the harsh environment and difficult logistics, there is little continuous data available on ice shelves. Second, the ice-water-rock setting with a strong low velocity layer is significantly different from ordinary crustal structure and could affect the convergence and interpretation of noise cross-correlation functions (NCFs). To address the question of what can be gained with such an approach, we apply noise correlation methods to the Amery Ice Shelf on the east coast of Antarctica (Figure 5.1A), where a number of seismic instruments were deployed for multiple years near the tip of the Loose Tooth Rift system to monitor its growth (Bassis et al., 2005; Bassis et al., 2007; Fricker et al., 2005; Figure 5.1B). Near the site, the thicknesses of the ice and water layers are about 300m and 500m, respectively (Fricker et al., 2005; Galton-Fenzi et al., 2008; Figure 5.2). One question we explore is whether we can retrieve this structural information from noise correlations.

This experiment also serves as a proof of concept for planetary applications of the noise correlation method on icy satellites. For example, a variety of evidence suggests that there may exist subsurface liquid oceans on Europa (e.g., Carr et al., 1998; Kivelson et al., 2000) and Titan (e.g., Tobie et al., 2006; Lunine and Lorenz, 2009; Castillo-Rogez and Lunine, 2010). The thicknesses of the ice and liquid layers, which are important for understanding icy satellite dynamics, are still uncertain. Different kinds of seismic experiments have been proposed to improve estimates in future missions (e.g., Kovach and Chyba, 2001; Lee et al., 2003; Panning et al., 2006; Jackson et al., 2010; Tsai, 2010a). In particular, the emerging noise correlation method is attractive for planetary missions because it potentially provides surface-wave (e.g., Shapiro et al., 2005) and body-wave (e.g., Zhan et al., 2010; Poli et al., 2012; Lin et al., 2013) Green's functions without seismic events. For example, Larose et al. (2005) applied the noise correlation method to lunar data and constrained the near-surface (top 10-meter) seismic structure. Recently, Tibuleac and von Seggern (2012) and Gorbatov et al. (2013) also reported reflected crustal phases from noise auto-correlations on individual stations. Because it is difficult to deploy more than one seismic station in planetary missions, the noise auto-correlation method might be more practical than the cross-correlation method. With a similar ice-liquid-solid structural setting, the Amery Ice Shelf is an ideal test ground for the application of noise cross-correlation and auto-correlation methods on icy satellites.

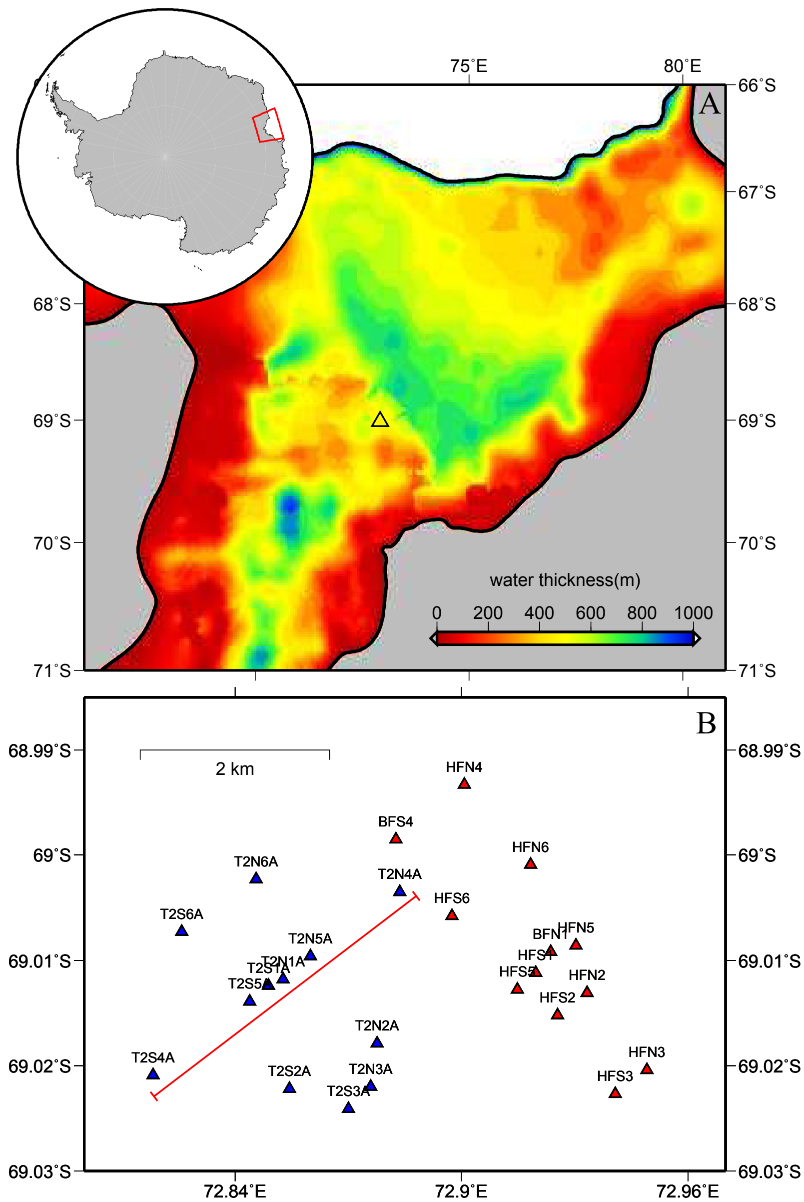


Figure 5.1: (A) Map of the Amery Ice Shelf and water-column thickness. The triangle marks the location of the seismic deployment. (B) Station distribution map. Blue triangles and red triangles show the stations deployed in 2005 and 2007, respectively. The red line denotes the profile whose NCFs are shown in Figure 5.3. In both years, the instruments surround the same ice area, but the ice has advected ~2 km (to the NE) in the 2 years between deployments.

## 5.3 Data and Method

Figure 5.1B shows the locations of the three-component short-period (1-10 Hz) instruments deployed during the 2005 and 2007 field seasons. Both campaigns (Bassis et al., 2007) were active for about 2 months during the Antarctic summer. Because of the different environment and frequency band from most noise correlation studies, we modified some of the common procedures (e.g., Bensen et al., 2007; Zhan et al., 2011) to calculate the 9-component NCFs (E, N, Z with E, N, Z) for all station pairs. We first remove instrumental responses and cut the data into 10-minute segments. Because signals from earthquakes are weak in the frequency band of 1 to 10 Hz, here we do not use temporal normalization to remove earthquakes. To preserve the amplitude spectrum, especially for auto-correlations, we also do not apply spectral whitening to the waveforms. The two stations' waveforms are cross correlated for each segment and then stacked with normalized maximum amplitudes. The use of very short 10-minute segments and normalized stacking achieves the equivalent of the temporal normalization used in most noise correlation studies to remove earthquakes, and may be important in the presence of occasional icequakes.

## 5.4 Noise cross-correlations in time domain

Although the elastic structure of the ice shelf near the site can be estimated with other methods (e.g., Vaughan, 1995), the NCFs produced here provide the first direct in situ measurement of ice shelf elastic structure. Elastic structure is inferred from the NCFs by comparing the observations with synthetic Green's functions produced for various assumed structures using a frequency-wavenumber method (Zhu and Rivera, 2002) to compute the synthetic Green's functions due to a surface point force. Using borehole measurements, Craven et al. (2009) show that the ice shelf consists of a ~50 m firn layer on top of a ~250 m continental meteoric and marine ice layer.

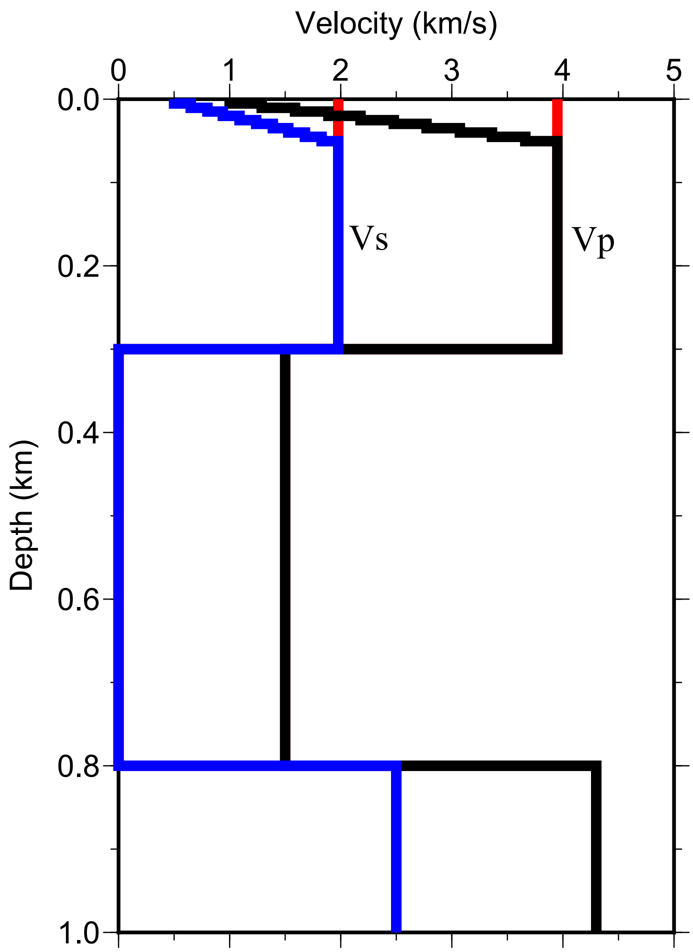


Figure 5.2: 1D $P$- and $S$-wave velocity models used to compute synthetic Green's functions. Differences between the two 1D models with or without the top 50-m firn layer are highlighted by the red segments.

Following Wittlinger and Farra (2012), we set the $V_p$ and $V_s$ to be 3.95 km/s and 2 km/s, respectively, for both the meteoric and marine ice layer. The velocities in the firn layer are poorly constrained and $V_p$ can be as low as 0.5 km/s (Albert, 1998), and we therefore test two different models, one without a slow firn layer, and one with a slow layer of constant gradient and $V_p/V_s$ ratio of 2 (Figure 5.2). For the latter model, we adjust the absolute $V_p$ on the surface to best fit the seismic data.

We first compare the NCFs along a NE-SW profile (red line in Figure 5.1B) with the synthetic Green's functions in the 5-10 Hz frequency band (Figure 5.3A, 5.3B). We rotated the EN-EN NCFs into radial-radial (RR) components and summed the positive and negative sides. We see clear Rayleigh waves in the NCFs (dashed line in Figure 5.3A) propagating at a speed of about 1.5 km/s, much slower than the synthetic Rayleigh waves of the 1D homogeneous ice model (without a slow firn layer), as shown in red in Figure 5.3B. To fit the observed Rayleigh waves, we adjust the 1D model with a slow firn layer to have a surface $V_p$ of 1 km/s and plot the synthetics in black in Figure 5.3B. We note that if a more complex velocity structure were allowed, there would be tradeoffs between the various parameters, including the thickness of the slow layer and its velocity anomaly.

In the 5-10 Hz frequency band, the observed Rayleigh waves are only sensitive to depths shallower than about 100 m, significantly shorter than the ice thickness, and therefore do not have sensitivity to the ice-water interface. To sample the interface, we need to study NCFs at lower frequencies. For the same station pairs at 1-5 Hz, the synthetic Green's functions are similar for the two 1D models because they are only different in the thin top layer. However, we find that the NCFs do not resemble these synthetic Green's functions (Figure 5.3C, 5.3D). In fact, the observed NCFs clearly cannot be represented by a Green's function because they violate causality. The dashed line in Figure 5.3D marks the onset of the synthetics, and the P, S and surface waves must arrive after this dashed line due to causality. On the other hand, the observed NCFs are acausal, with most of their energy arriving before or around the same time as the dashed line shown in Figure 5.3C. This comparison is also true for other station pairs. Therefore, it is not possible to interpret the NCFs solely as being Green's functions between stations, and we must rely on an alternative interpretation of the NCFs to retrieve further structural information.

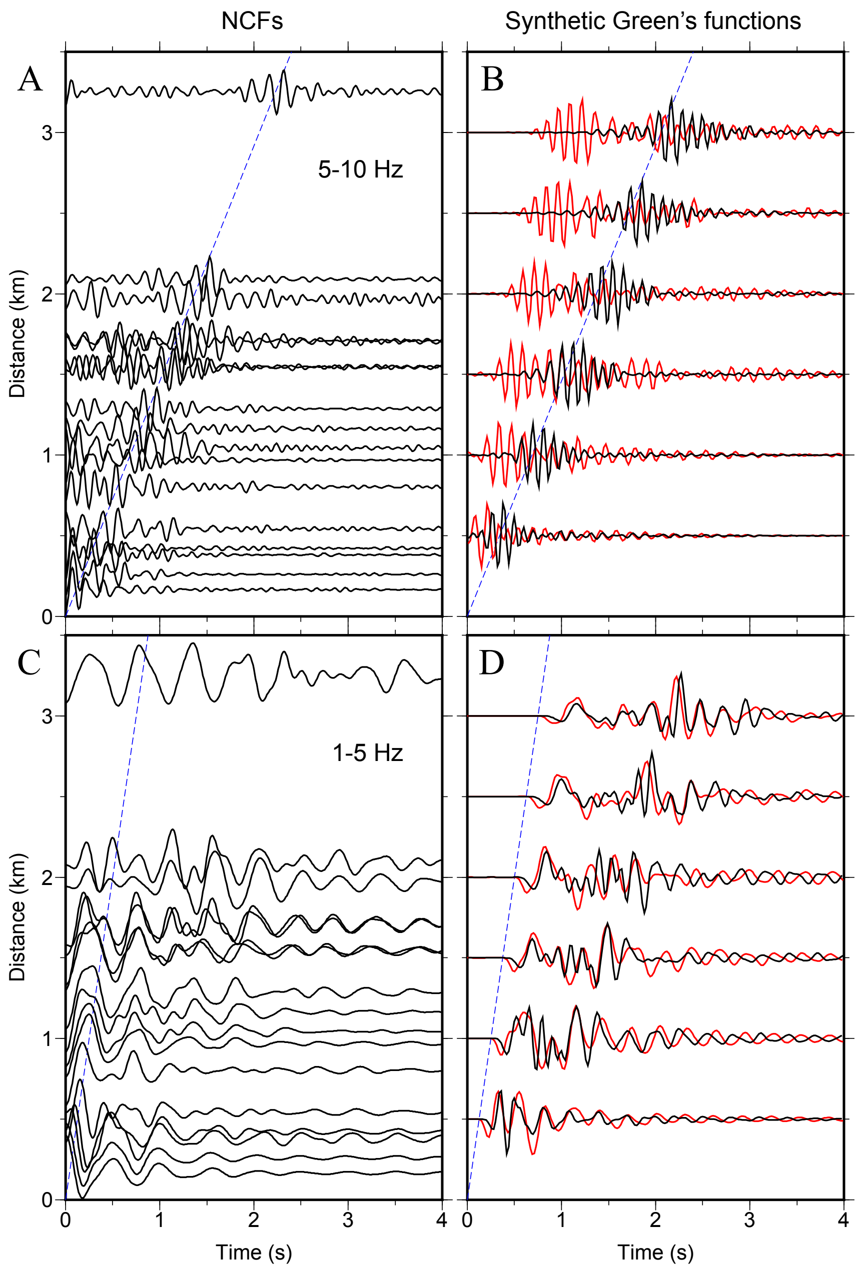


Figure 5.3: NCFs in the time domain (A, C) and comparisons with synthetic Green's functions (B, D). The top and bottom panels are for the frequency bands 5-10 Hz and 1-5 Hz, respectively. In (B, D), the red and black synthetics are computed with the 1D models without and with the firn layer, respectively.

## 5.5 Spectral ratios of noise cross-correlations

Although the 1-5 Hz NCFs in the time domain are difficult to interpret, we find that the spectral ratios of NCFs on different components still contain useful information about the velocity structure. With the three-component stations, we have 9 components of the NCFs (ZNE-ZNE) for each station pair. We first estimate the NCF amplitude spectra for all components and then take their spectral ratios with the ZZ component (ZZ/XY, where X and Y can be Z, N, or E). Figure 5.4 shows the average spectral ratios over all station pairs for each component in 2007. For all the components (except ZZ/ZZ which is 1 by definition), we observe regularly spaced peaks at about every 1.5 Hz up to about 6 Hz. These peaks are stronger on the components involving only East or North (Figs. 5.4E, F, H, and I). The observed peaks in the NCF spectral ratios are approximately equally spaced in frequency (a phenomenon typical for resonating systems), and imply more coherent waves on the vertical components than the horizontal components at these frequencies.

We interpret the observed peaks in Figure 5.4 as $P$-wave resonances in the water layer (Figure 5.5). As shown in Figure 5.2, the water layer sandwiched between the ice and rock layers is a strong low-velocity waveguide with little attenuation (high $Q$). Therefore the water layer traps seismic waves and creates a diffuse wavefield inside it. The $P$-wave critical angle is about 22° for the ice-water interface and even smaller (≈20°) for the water-rock interface. Therefore, waves in the water layer with incident angles larger than 22° will be completely reflected back to the water and are not recorded on the free surface under the assumption of geometrical ray theory. Waves with incident angles ($\theta$ in Figure 5.5) smaller than the critical angle can leak into the ice layer and reach the stations at the free surface. Due to the slow firn layer on top, the transmitted P waves will bend steeper toward the surface, and reach the stations with incident angles smaller than the $\theta \leq 22°$ in the water layer (Figure 5.5).

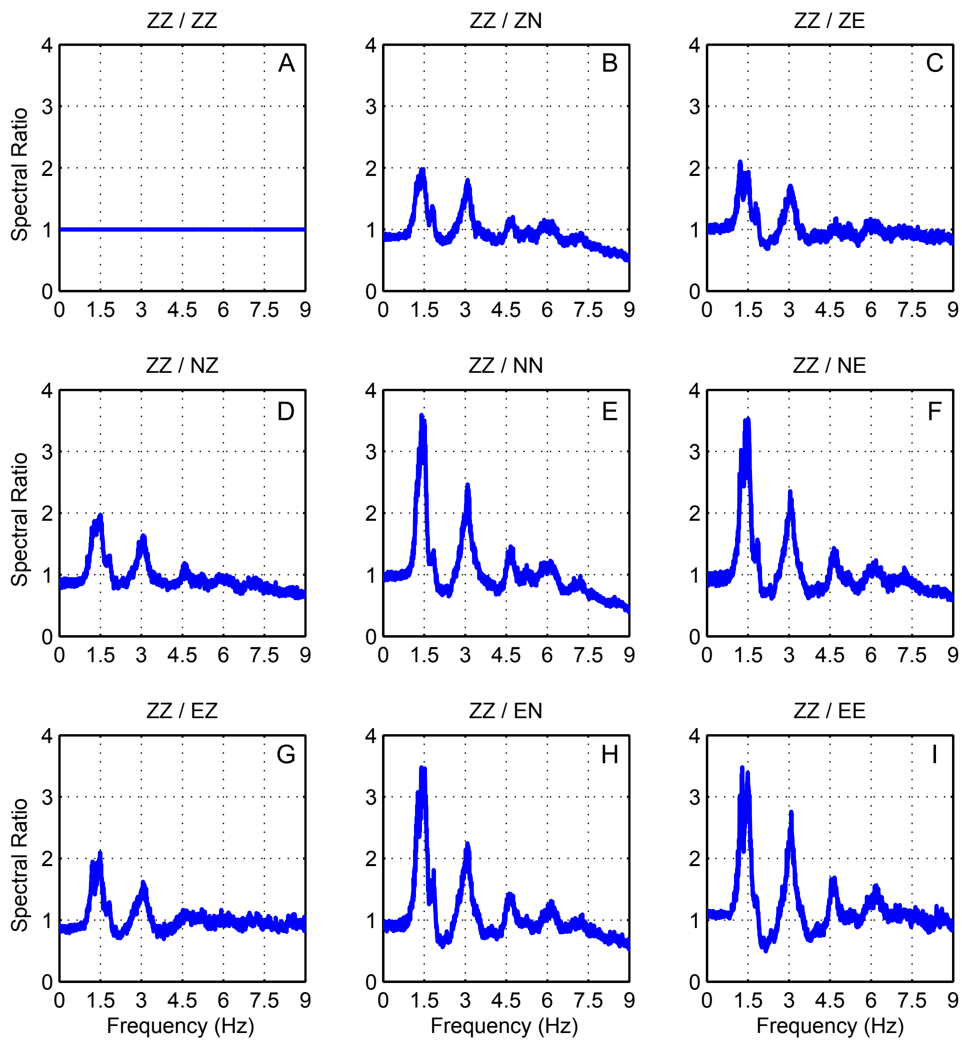


Figure 5.4: Average NCF spectral ratios for the year 2007. The title of each panel shows the components in format ZZ/XY, where X and Y can be one of E, N, Z.

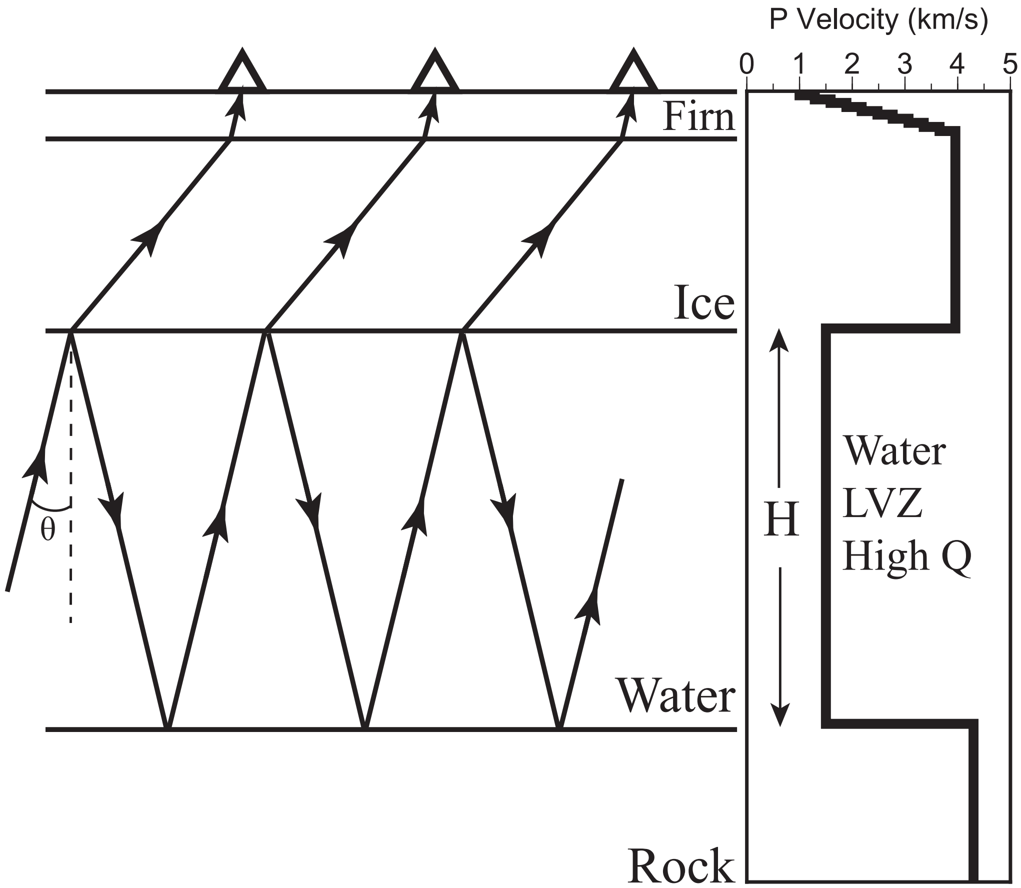


Figure 5.5: Illustration of how trapped waves in the slow water layer propagate to the free surface. The 1D $P$-wave velocity model is plotted to the right as reference. See the text for more details.

These steeply traveling $P$ waves will cause stronger ground motion on the vertical components than the horizontal components. Because these transmitted P waves have travelled nearly vertically ($\theta \leq 22°$) inside the water layer, we can calculate the resonance frequencies as $f_n = n\frac{V_p}{2H}$, where $n = 1, 2, 3, \ldots$, $H$ is the water-column thickness, and assuming $\theta$ is small. Given $V_p \approx 1.5$ km/s, we derive $H \approx 500$ m from the resonance peaks at 1.5 Hz, 3 Hz, 4.5 Hz, 6 Hz (Figure 5.4), consistent with the previous measurements shown in Figure 5.1A (Galton-Fenzi et al., 2008).

With the new interpretation of the NCF spectral ratios described above, we can now explain the observed NCFs in the time domain (Figure 5.3C). Because the coherent 1-5 Hz noise at the stations are dominated by the nearly vertical $P$ waves from the water layer, the NCFs will have most of their signal near zero lag and will not resemble the Green's functions between the stations (Figure 5.3), which would have been retrieved if the noise field were diffuse (Lobkis and Weaver, 2001). Note that the NCFs' failure to converge to Green's functions is directly related to the structure itself, i.e. the strong low-velocity water layer causes the noise field to be non-diffuse. In order for the noise field to remain diffuse with this structure, a very specific non-uniform distribution of noise sources would be required (Tsai, 2010b). The observed resonance peaks decay as frequency increases (Figure 5.4) and are small at about 6 Hz. This may be caused by stronger seismic scattering or attenuation at higher frequencies. Therefore for the frequency band of 5-10 Hz, the coherent noise field may be more diffuse than in the 1-5 Hz band, and the observed NCFs resemble the Rayleigh-wave Green's functions (Figure 5.3).

## 5.6 Noise auto-correlations

The raw ambient seismic noise at a station consists of coherent and incoherent contributions. The coherent noise consists of seismic waves propagating in the medium and, in this study, is dominated by the $P$ waves from the water layer. The incoherent parts may be mechanical noise, electronic noise, inelastic deformation, or any other perturbations that do not propagate from one station to another. Cross-correlations between two stations emphasize the coherent noise and reduce the incoherent noise such that we can clearly identify the resonance peaks from the NCFs. If the incoherent noise is weaker than the coherent noise at some stations, we should still be able to observe the resonance peaks in the spectral ratios of auto-correlations. Indeed, for one broadband station during the 2007 deployment, we can observe the

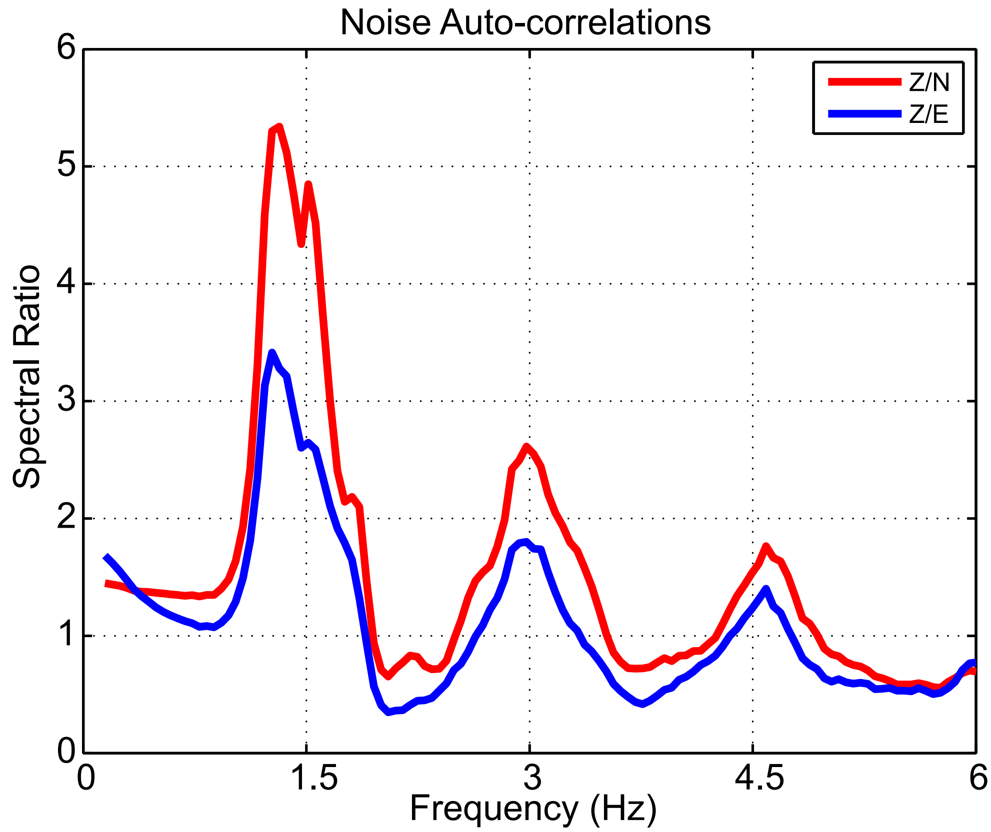


Figure 5.6: Spectral ratios of noise auto-correlations at station BFN1 in 2007. The red and blue curves are for ratios between vertical and north or east, respectively.

same resonances in the spectral ratios between the vertical and two horizontal components (Figure 5.6). This suggests that noise auto-correlations can also be used to study ice shelf structure but requires a better setup (e.g., instrument type, wind isolation, ground coupling) for lower levels of incoherent noise. Since the auto-correlation method is particularly attractive for planetary missions with a single station, these factors should be considered in the design of such experiments.

## 5.7 Conclusions

In this paper, we have studied noise cross-correlations and auto-correlations on the Amery Ice Shelf. For the frequency band 5-10 Hz, we retrieved Rayleigh-wave Green's functions between stations, and determined that P-wave velocities in the top 50-m firn layer (down to 1 km/s) are significantly slower than typical ice *P*-wave velocities. For the frequency band 1-5 Hz, we find that the NCFs do not converge to the Green's functions. Instead, we explain the observations as resulting from a significantly non-diffuse noise field caused by the low velocity waveguide of the water layer sandwiched between the ice and rock layers. Under this new interpretation, we explain the observed peaks in the NCF spectral ratios as *P*-wave resonances in the water layer, and estimate the water-column thickness. For stations with low levels of incoherent noise, noise auto-correlations also provide a consistent estimate of water thickness. These results can help in the design of future passive seismic experiments to estimate and monitor the structure of ice shelves and water-column thicknesses. Our study may also provide insight for the design of future missions involving seismic exploration of other planetary bodies. In particular, the study presented here serves as a proof of concept for planetary applications of the noise correlation method on icy satellites, such as Titan and Europa.

# References

Albert, D.G., 1998. Theoretical modeling of seismic noise propagation in firn at the South Pole, Antarctica, Geophysical Research Letters, 25, 4257-4260.

Bassis, J.N., Coleman, R., Fricker, H. & Minster, J., 2005. Episodic propagation of a rift on the Amery Ice Shelf, East Antarctica, Geophysical Research Letters, 32, L06502.

Bassis, J.N., Fricker, H.A., Coleman, R., Bock, Y., Behrens, J., Darnell, D., Okal, M. & Minster, J.-B., 2007. Seismicity and deformation associated with ice-shelf rift propagation, Journal of Glaciology, 53, 523-536.

Bensen, G., Ritzwoller, M., Barmin, M., Levshin, A., Lin, F., Moschetti, M., Shapiro, N. & Yang, Y., 2007. Processing seismic ambient noise data to obtain reliable broad-band surface wave dispersion measurements, Geophysical Journal International, 169, 1239-1260.

Carr, M.H., Belton, M.J., Chapman, C.R., Davies, M.E., Geissler, P., Greenberg, R., McEwen, A.S., Tufts, B.R., Greeley, R. & Sullivan, R., 1998. Evidence for a subsurface ocean on Europa, Nature, 391, 363-365.

Castillo-Rogez, J.C. & Lunine, J.I., 2010. Evolution of Titan's rocky core constrained by Cassini observations, Geophysical Research Letters, 37, L20205.

Craven, M., Allison, I., Fricker, H.A. & Warner, R., 2009. Properties of a marine ice layer under the Amery Ice Shelf, East Antarctica, Journal of Glaciology, 55, 717.

Fricker, H., Young, N., Coleman, R., Bassis, J. & Minster, J.B., 2005. Multi-year monitoring of rift propagation on the Amery Ice Shelf, East Antarctica, Geophysical Research Letters, 32, L02502.

Galton-Fenzi, B., Maraldi, C., Coleman, R. & Hunter, J., 2008. The cavity under the Amery Ice Shelf, East Antarctica, Journal of Glaciology, 54, 881-887.

Gorbatov, A., Saygin, E. & Kennett, B., 2013. Crustal properties from seismic station autocorrelograms, Geophysical Journal International, 192, 861-870.

Hemer, M., Hunter, J. & Coleman, R., 2006. Barotropic tides beneath the Amery Ice Shelf, Journal of Geophysical Research, 111, C11008.

Jackson, J., Zhan, Z., Clayton, R., Helmberger, D. & Tsai, V., 2010. Ambient seismic noise applications for Titan. in AGU Fall Meeting, San Francisco, Calif., 13-17 Dec.

Kivelson, M.G., Khurana, K.K., Russell, C.T., Volwerk, M., Walker, R.J. & Zimmer, C., 2000. Galileo magnetometer measurements: A stronger case for a subsurface ocean at Europa, Science, 289, 1340-1343.

Kovach, R.L. & Chyba, C.F., 2001. Seismic detectability of a subsurface ocean on Europa, Icarus, 150, 279-287.

Larose, E., Khan, A., Nakamura, Y. & Campillo, M., 2005. Lunar subsurface investigated from correlation of seismic noise, Geophysical Research Letters, 32, L16201.

Lee, S., Zanolin, M., Thode, A.M., Pappalardo, R.T. & Makris, N.C., 2003. Probing Europa's interior with natural sound sources, Icarus, 165, 144-167.

Lin, F.C., Moschetti, M.P. & Ritzwoller, M.H., 2008. Surface wave tomography of the western United States from ambient seismic noise: Rayleigh and Love wave phase velocity maps, Geophysical Journal International, 173, 281-298.

Lin, F.C., Tsai, V.C., Schmandt, B., Duputel, Z. & Zhan, Z., 2013. Extracting seismic core phases with array interferometry, Geophysical Research Letters, 40, 1049-1053.

Lobkis, O.I. & Weaver, R.L., 2001. On the emergence of the Green's function in the correlations of a diffuse field, The Journal of the Acoustical Society of America, 110, 3011.

Lunine, J.I. & Lorenz, R.D., 2009. Rivers, lakes, dunes, and rain: Crustal processes in Titan's methane cycle, Annual Review of Earth and Planetary Sciences, 37, 299-320.

McMahon, K.L. & Lackie, M.A., 2006. Seismic reflection studies of the Amery Ice Shelf, East Antarctica: delineating meteoric and marine ice, Geophysical Journal International, 166, 757-766.

Panning, M., Lekic, V., Manga, M., Cammarano, F. & Romanowicz, B., 2006. Long-period seismology on Europa: 2. Predicted seismic response, Journal of geophysical Research, 111, E12008.

Poli, P., Campillo, M. & Pedersen, H., 2012. Body-Wave Imaging of Earth's Mantle Discontinuities from Ambient Seismic Noise, Science, 338, 1063-1065.

Pyle, M.L., Wiens, D.A., Nyblade, A.A. & Anandakrishnan, S., 2010. Crustal structure of the Transantarctic Mountains near the Ross Sea from ambient seismic noise tomography, Journal of Geophysical Research, 115, B11310.

Shapiro, N.M., Campillo, M., Stehly, L. & Ritzwoller, M.H., 2005. High-resolution surface-wave tomography from ambient seismic noise, Science, 307, 1615-1618.

Tibuleac, I.M. & von Seggern, D., 2012. Crust–mantle boundary reflectors in Nevada from ambient seismic noise autocorrelations, Geophysical Journal International, 189, 493-500.

Tobie, G., Lunine, J.I. & Sotin, C., 2006. Episodic outgassing as the origin of atmospheric methane on Titan, Nature, 440, 61-64.

Tsai, V.C., 2010a. One-station seismology without traditional seismic sources, in AGU Fall Meeting, San Francisco, Calif., 13-17 Dec.

Tsai, V.C., 2010b. The relationship between noise correlation and the Green's function in the presence of degeneracy and the absence of equipartition, Geophysical Journal International, 182, 1509-1514.

Vaughan, D.G., 1995. Tidal flexure at ice shelf margins, Journal of Geophysical Research, 100, 6213-6224.

Wittlinger, G. & Farra, V., 2012. Observation of low shear wave velocity at the base of the polar ice sheets: evidence for enhanced anisotropy, Geophysical Journal International, 190, 391-405.

Yao, H., van Der Hilst, R.D. & De Hoop, M.V., 2006. Surface-wave array tomography in SE Tibet from ambient seismic noise and two-station analysis–I. Phase velocity maps, Geophysical Journal International, 166, 732-744.

Zhan, Z., Ni, S., Helmberger, D.V. & Clayton, R.W., 2010. Retrieval of Moho-reflected shear wave arrivals from ambient seismic noise, Geophysical Journal International, 182, 408-420.

Zhan, Z., Wei, S., Ni, S. & Helmberger, D., 2011. Earthquake centroid locations using calibration from ambient seismic noise, Bulletin of the Seismological Society of America, 101, 1438-1445.

Zhu, L. & Rivera, L.A., 2002. A note on the dynamic and static displacements from a point source in multilayered media, Geophysical Journal International, 148, 619-627.

# Part II

# Earthquake Waveforms

# Chapter 6

# Anomalously steep dips of earthquakes in the 2011 Tohoku-Oki source region and possible explanations

This chapter has been published as:

Zhongwen Zhan, Don Helmberger, Mark Simons, Hiroo Kanamori, Wenbo Wu, Nadaya Cubas, Zacharie Duputel, Risheng Chu, Victor C. Tsai, Jean-Philippe Avouac, Kenneth W. Hudnut, Sidao Ni, Eric Hetland, Francisco H. Ortega Culaciati (2012), Anomalously steep dips of earthquakes in the 2011 Tohoku-Oki source region and possible explanations, Earth and Planetary Science Letters, Volume 353-354, Pages 121-133.

## 6.1 Abstract

The 2011 Mw 9.1 Tohoku-Oki earthquake had unusually large slip (over 50 m) concentrated in a relatively small region, with local stress drop inferred to be 5–10 times larger than that found for typical megathrust earthquakes. Here we conduct a detailed analysis of foreshocks and aftershocks (Mw 5.5–7.5) sampling this megathrust zone for possible clues regarding such differences in seismic excitation. We find that events occurring in the region that experienced large slip during the Mw 9.1 event had

steeper dip angles (by 5–10°) than the surrounding plate interface. This discrepancy cannot be explained by a single smooth plate interface. We provide three possible explanations. In Model I, the oceanic plate undergoes two sharp breaks in slope, which were not imaged well in previous seismic surveys. These break-points may have acted as strong seismic barriers in previous seismic ruptures, but may have failed in and contributed to the complex rupture pattern of the Tohoku-Oki earthquake. In Model II, the discrepancy of dip angles is caused by a rough plate interface, which in turn may be the underlying cause for the overall strong coupling and concentrated energy-release. In Model III, the earthquakes with steeper dip angles did not occur on the plate interface, but on nearby steeper subfaults. Since the differences in dip angle are only 5–10°, this last explanation would imply that the main fault has about the same strength as the nearby subfaults, rather than much weaker. A relatively uniform fault zone with both the main fault and the subfaults inside is consistent with Model III. Higher resolution source locations and improved models of the velocity structure of the megathrust fault zone are necessary to resolve these issues.

## 6.2 Introduction

The devastating 2011 Mw 9.1 Tohoku-Oki earthquake occurred on the megathrust where the Pacific Plate subducts below Japan at an average rate of about 8.0–8.5 cm/yr (DeMets et al., 2010). This earthquake was largely unexpected mainly due to the absence of large (M>8.3) earthquakes in recorded history, despite evidence for a similar earthquake in 869 AD, the Jogan earthquake (Minoura et al., 2001 and Usami, 1966). Geophysical observations of the Tohoku-Oki earthquake stem from global and regional broadband seismographic networks (e.g., Ammon et al., 2011, Ide et al., 2011 and Lay et al., 2011), a near-field geodetic network (e.g., Ozawa et al., 2011 and Simons et al., 2011), as well as ocean bottom measurements (e.g., Sato et al., 2011 and Tsuji et al., 2011) and open ocean tsunami data (e.g., Simons et al., 2011). Earthquake slip models generated from various combinations of these datasets all display high co-seismic slip (25–50 m) in a relatively small region (~150 km by 100 km) (Figure 6.1A). For comparison, models of the 2010 Mw 8.8 Maule, Chile, earthquake typically have twice the along-strike extent of slip and less than half the peak slip (Simons et al., 2011). The long recurrence time and concentrated region of large slip suggest the potential existence of barriers that support high stress accumulation before they rupture. Under this hypothesis, such barriers may pin the fault locally, limiting the amount of seismic slip occurring in neighboring areas that have lower thresholds for failure. When the strongest barrier finally ruptures, the surrounding areas can catch up (Simons et al., 2011). Several candidates for barriers, including subducted seamounts and bending of the oceanic plate, have been proposed by Fukao et al. (2011). Zhao et al. (2011) suggest that the high stress drop may be controlled by structural heterogeneities in the megathrust zone.

Another important aspect of the Tohoku-Oki earthquake is the depth variation of seismic wave radiation. While co-seismic slip models show that large slip occurred updip of the hypocenter (e.g., Lay et al., 2011, Shao et al., 2011b, Simons et al., 2011 and Wei et al., 2012), the majority of back-projection methods locate most coherent high-frequency (~1 Hz) radiation downdip of the hypocenter (e.g., Koper et al., 2011 and Simons et al., 2011; light blue area in Figure 6.1A). This spatial offset between large slip and high-frequency radiation is also reported for other megathrust earthquakes, such as the 2004 Sumatra-Andaman earthquake and the 2010 Chile earthquake (e.g., Lay et al., 2012). This depth variation in seismic radiation may suggest along-dip variations in mechanical or frictional properties (Lay et al., 2012 and Simons et al., 2011), but the physical cause is still unclear.

To better understand the Tohoku-Oki earthquake's large stress drop and the offset between the areas of large slip and high-frequency radiation, we need more information

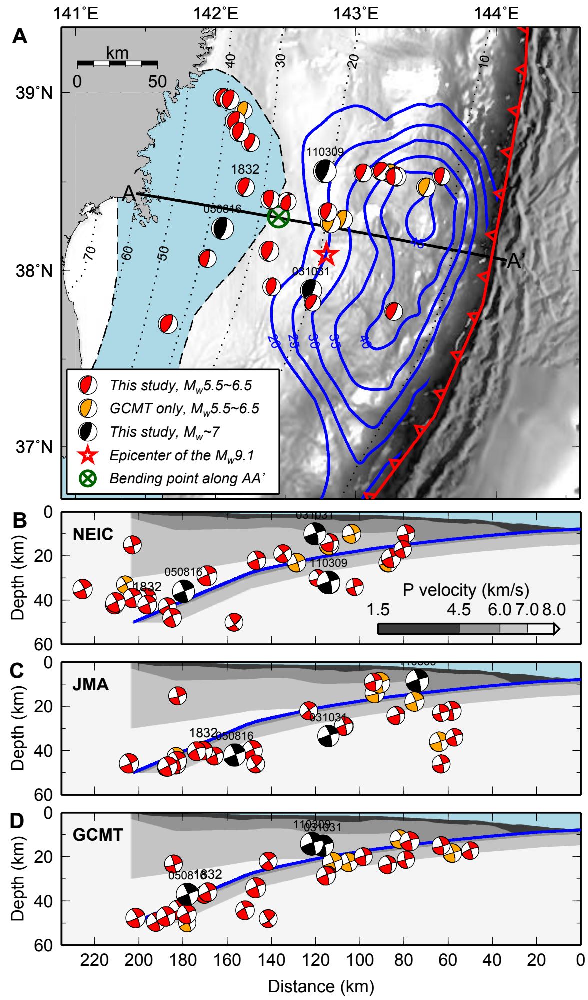


Figure 6.1: Locations of events occurring along the megathrust. (A) Map view of our study area. Blue contours are the co-seismic slip model of the 2011 Tohoku-Oki earthquake from Wei et al. (2012). The light blue area shows the source area of high frequency radiation as imaged by back-projection method (Koper et al., 2011). AA' is a seismic reflection and refraction profile (Miura et al., 2005), whose result is shown in Figure 6.1B. Colored beachballs (see legend) indicate all the Mw>5.5 shallow-angle thrust earthquakes near the AA' profile (<60 km), except the 2011 Tohoku-Oki earthquake. The red star indicates the epicenter location of the Tohoku-Oki earthquake determined by an Ocean-Bottom-Seismometer (OBS) network (Suzuki et al., 2012). (B) Greyscale background shows the 2D P wave velocity model along AA' profile, from Miura et al. (2005). The blue line is the reference plate interface at the top of the low-velocity oceanic crust. Colored beachballs (see the legend in (A)) show the NEIC locations of the earthquakes, projected to the AA' profile. (C, D) Similar to (B), but for JMA and GCMT, respectively. The red beachball labeled 1832 is the December 16, 2005, 18:32 Mw 6.0 earthquake, discussed later as an example event. Note the inconsistencies among earthquake locations, especially depths, from different catalogs.

about the megathrust's properties. Small to moderate interplate earthquakes have been widely used to extract mechanical properties on and around the plate interface. For example, Hasegawa et al. (2007) used repeating earthquakes to infer the coupling rate on the megathrust. Zhao et al. (2011) inverted earthquake travel times for a P wave velocity model around the plate interface. By studying seismic source spectra for Mw 6.0–7.6 earthquakes, Ye et al. (2012) showed depth dependent stress drops.

In this paper, we use the locations and focal mechanisms of all Mw≥5.5 earthquakes in the source area of the Tohoku-Oki earthquake to systematically study the geometry of the plate interface. We first discuss potential biases and uncertainties in earthquake locations and focal mechanisms from routine catalogs. Due to these issues, we explore high-resolution methods to re-estimate earthquake depths and focal mechanisms using available velocity models in the Tohoku-Oki region. We find that interplate earthquakes in this area occurred close to the plate interface imaged in previous seismic surveys, but there is a clear depth-dependent dip angle discrepancy. Three possible explanations of the discrepancy and their pros/cons are discussed.

## 6.3 Routine Catalogs and Previous Studies

Earthquake locations and focal mechanisms of Mw≥5.5 earthquakes around the globe are reported by many routine catalogs. However, these routinely determined results have significant inconsistencies as displayed in Figure 6.1. For the Tohoku-Oki source region, Figure 6.1B–D compares the projected locations of Mw 5.5–7.5 shallow-angle thrust earthquakes on the AA' profile (Figure 6.1A), based on the National Earthquake Information Center (NEIC), the Japan Meteorological Agency (JMA) and the Global Centroid Moment Tensor (GCMT) catalogs, respectively. The NEIC catalog's horizontal locations are systematically shifted to the west of the JMA and GCMT locations by about 20 km. JMA's and GCMT's horizontal locations are relatively consistent near the Japan coast, but less consistent towards the trench. Depths are even less well resolved for the three catalogs. The uncertainty in earthquake locations, especially depths, makes it hard to distinguish between interplate and intraplate earthquakes.

Earthquake focal mechanisms or moment tensor solutions also have similar difficulties. Most routine catalogs of earthquake focal mechanisms do not have (meaningful) error estimation. By comparing focal mechanisms from different catalogs (e.g., the GCMT catalog and the USGS CMT catalog) between 1977 and 2003, Kagan (2003) shows that for shallow M$\geq$6 earthquakes, the average 3D rotation angle is about 20°. However, the uncertainties of different focal mechanism parameters (strike, dip and rake) were not addressed. Depending on the wave types and inverse method, particular focal mechanism parameters could be well resolved. For example, if teleseismic P waves are used to constrain a shallow-angle thrust focal mechanism as displayed in Figure 6.2, the steep fault plane (denoted as Plane2 in Figure 6.2B, described by strike2 and dip2) is well sampled and resolved. The shallow-angle fault plane (Plane1) is related to Plane2 by rake2, which could have a larger uncertainty. Figure 6.2C shows the scatter of focal mechanisms with perfectly constrained strike2 and dip2, but rake2 with a Gaussian error (std=5°). The corresponding distributions of strike2, dip2, rake2, strike1, dip1 and rake1 are shown in (D, E, F, G, H, I). Although strike1 and rake1 have large uncertainties, dip1 (especially its lower limit) is well constrained. It is this dip angle that we focus on here.

There is significant moment-dip-depth tradeoff in inversions of focal mechanisms for shallow earthquakes determined by long-period surface waves (e.g., Kanamori and Given, 1981 and Tsai et al., 2011). This tradeoff is generally not explicitly addressed in routine catalogs. Due to these difficulties, the interpretation of focal mechanisms in terms of plate interface geometry is not straight-forward. For example, Hayes et al. (2009) observed a systematic difference between the dips of their inverted plate

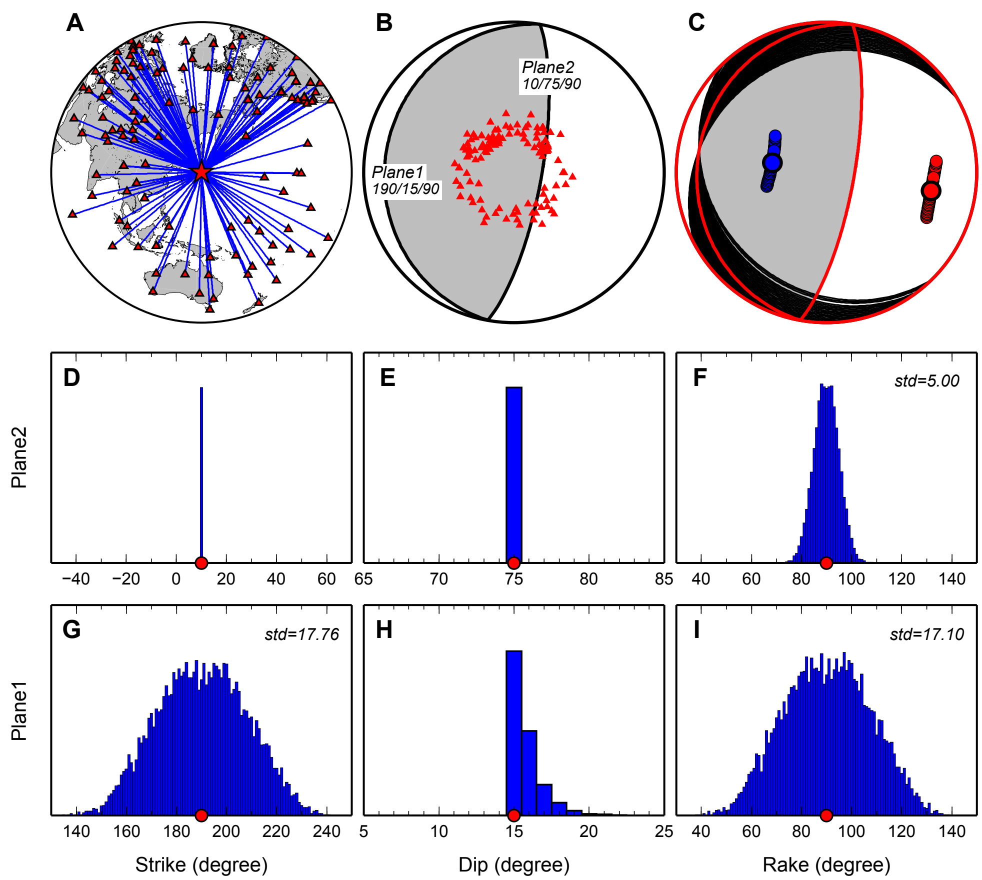


Figure 6.2: Sensitivity analysis of focal mechanism parameters. (A) Map view of the Global Seismographic Network (GSN) and International Federation of Digital Seismograph Networks (FDSN) stations used in this study (red triangles). Note the good azimuthal coverage with respect to our study region (red star). (B) Sampling of teleseismic body waves (red triangles) on the lower hemisphere of a typical shallow-angle thrust focal mechanism in this region. Apparently Plane2 (described by strike2, dip2) is well sampled, while Plane1 (described by strike1, dip1) is not. Plane1 and Plane2 are related by the rake angles (rake1, rake2). (C) Scatter of focal mechanisms (black lines and small dots) when strike2 and dip2 are perfectly constrained but rake2 has a Gaussian error with std=5°. The focal mechanism shown with the red line is the same as in (B). Red dots and blue dots indicate the P axes and T axes, respectively. The corresponding distributions of strike2, dip2, rake2, strike1, dip1 and rake1 are shown in (D, E, F, G, H, I). Although strike1 and rake1 have large uncertainties, dip1 (especially its lower limit) is well constrained.

interface model and the dips of GCMT moment tensors, but could not fully resolve whether this difference was real or related to focal mechanism bias.

The source area of the Tohoku-Oki earthquake is ideal for high-resolution study because of the availability of detailed crustal surveys. Using reflection and refraction data from an active source seismic experiment with 36 ocean bottom seismographs (OBS), Miura et al. (2005) and Ito et al. (2005) presented seismic profiles along AA' shown in Figure 6.1A. The 2D P wave velocity model from Miura et al. (2005) is shown as gray-scale background in Figure 6.1B–D. The plate interface can be easily identified as the top of the low velocity oceanic crust (blue lines). In this plate interface model, there is a kink at about 150 km from the trench, at a depth of ~28 km (see Figure 6.1A for a map view and B for side view), where the dip angle jumps from 13° to 23°. Although the ray coverage and resolution values indicate well-resolved model parameters, it should be noted that this velocity model and plate interface model are smoothed due to damping during inversion, and therefore only represent large-scale features. For example, Ito et al. (2005) presented a slightly different model using a similar dataset but a different inverse method. We use the Miura et al. (2005) plate interface model as our reference model, and differences that would result from using different models are described in Section 5. For our purposes, locations (especially depths) of events with respect to the plate boundary are important. As shown in Figure 6.1, while the JMA and GCMT horizontal locations have no systematic differences, the NEIC horizontal locations are offset ~20 km toward the coast. Suzuki et al. (2012) show that the JMA catalog near the coast does not have a systematic bias with respect to the catalog determined by OBS data. Because the quality of the JMA catalog drops toward the trench and the GCMT catalog appears to be most compatible with the OBS catalog, we will use GCMT catalog's horizontal locations in what follows. We consider all the Mw 5.5–7.5 interplate earthquakes over the time period from 1994 to mid-2012 near this seismic profile, and compare them with the reference plate interface model.

## 6.4 Methods

To avoid potential effects of strong lateral variations of seismic structure, we confined our study area to lie within a 120 km band centered around the AA' profile (Figure 6.1A). Since we are mainly interested in interplate earthquakes, we studied all the shallow-angle thrust events in this area from 1994 to the present (Mw 5.5–7.5 in the GCMT catalog). We used all available Global Seismographic Network (GSN) and International Federation of Digital Seismograph Networks (FDSN) seismograms to ensure a relatively uniform azimuthal coverage (Figure 6.2A). We present our high-resolution waveform analysis in detail for an example event (2005/12/16, 18:32 Mw 6.0, see Figure 6.1 for event information reported by the various organizations). We first invert for earthquake depths using broadband teleseismic P waves (Figure 6.3); then we invert for focal mechanisms using longer period teleseismic P and SH body waves and explore the uncertainties of different parameters (Figure 6.3).

### 6.4.1 Earthquake Depths

Earthquake depths are not well constrained in routine catalogs as shown in Figure 6.1B–D because only long-period waves or travel-time information are used in most cases. Accurate depth determination requires fitting relatively broadband waveforms including direct and depth phases taking into account a local seismic velocity model in the source region. The local high-resolution 2D tomographic model (Figure 6.1B) allows for broadband waveform modeling. For each earthquake, we only choose high signal-to-noise ratio (SNR) broadband (2–50 s period) vertical-component P wave packages (P+pP+sP) to estimate depth (Figure 6.3A). Synthetic seismograms are calculated with a 1D source-side velocity model extracted from the 2D velocity model

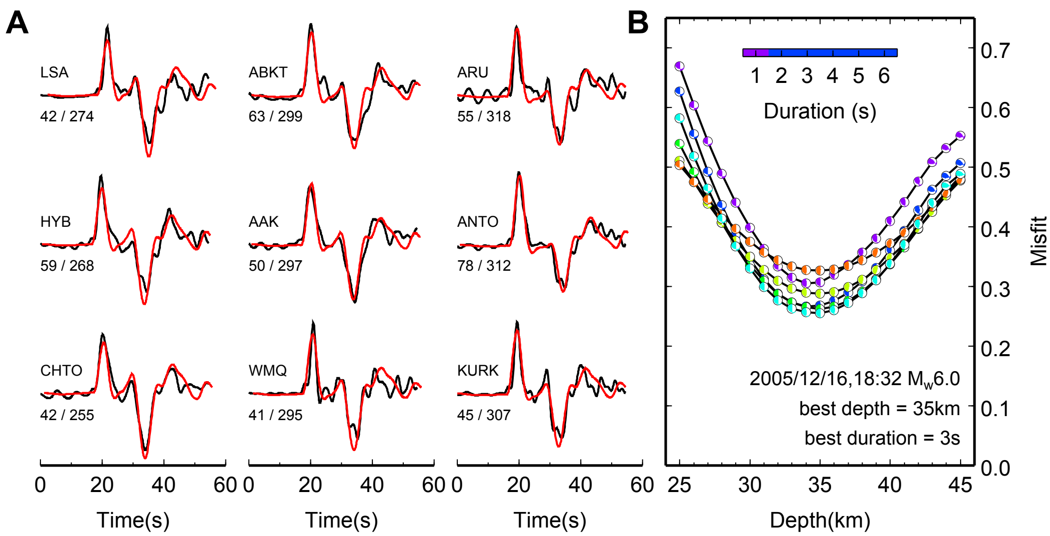


Figure 6.3: Estimation of earthquake depths using broadband teleseismic P waves with depth phases. (A) Examples of waveform fit for the 2005/12/16 Mw 6.0 earthquake. Data and synthetics seismograms are shown in black and red, respectively. The two numbers below each station name are epicentral-distance and azimuth in degrees. (B) Waveform misfits as a function of grid-searched earthquake depth and duration.

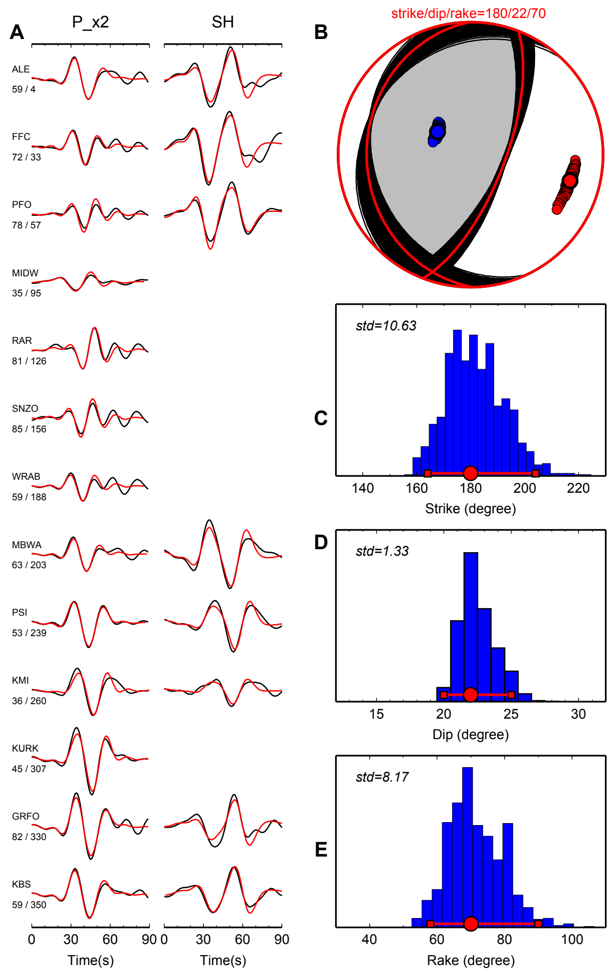


Figure 6.4: Focal mechanism inversion using 15–50 s period-band teleseismic P and SH waves. (A) Examples of waveform fit for the 2005/12/16 Mw 6.0 earthquake. Data and synthetic seismograms are shown in black and red, respectively. The two numbers below each station name are epicentral-distance and azimuth in degrees. P waves are multiplied by a factor of 2 to balance the larger SH amplitudes. Due to the higher quality control for SH, we usually have more P wave records than SH waves. (B) Red beachball and big dots show the best fit solution. We perform bootstrapping analysis to estimate the confidence limits. Black beachballs and small dots show the bootstrapping results. Red and blue dots indicate the P axes and T axes, respectively. (C, D, E) display the histograms of strike, dip and rake of the bootstrapping results, respectively. As quantified by the standard deviation (std shown in the upper-left corners) dip is constrained much better than strike and rake. Red dots represent the optimal values. Red squares and red lines indicate the corresponding 95% confidence limits, estimated by removing 2.5% on both sides of the histograms.

(Figure 6.1B) based on the earthquake's projected location on AA' (e.g., Kikuchi and Kanamori, 1982). We grid-search earthquake depth, duration and focal mechanism to best fit the normalized waveform. Note that due to large variations in broadband P wave amplitudes, we do not invert for seismic moment. As a typical example, Figure 6.3 shows the depth inversion and best waveform fits for the 2005/12/16, 18:32 Mw 6.0 earthquake, whose misfit curves have a well-defined minimum at 35 km, with little tradeoff with earthquake duration. This accurate estimation of earthquake depth will benefit our later focal mechanism inversion by largely removing the depth tradeoff.

Since the broadband P wave package includes the sP phase, and the 2D velocity model is only based on P waves, we generate an S velocity model by assuming a Vp/Vs ratio. Brocher (2005) compiled several different Vp/Vs measurements, and derived an empirical relation between Vp/Vs and Vp. The suggested average Vp/Vs is ~1.73. However, Suzuki et al. (2012) noticed that this forearc area may have a relatively high Vp/Vs ratio. Takahashi et al. (2002) determined both Vp and Vs velocity models along a high-resolution seismic profile in the forearc region of the Nankai Trough, and they also found higher Vp/Vs values. In this study, we use an average Vp/Vs ratio of ~1.87 from Takahashi et al. (2002). Tests show that different Vp/Vs ratios could cause systematic differences in earthquake depths (e.g., $\leq$3 km for Vp/Vs=1.73 or 1.87), but have little effect on earthquake focal mechanisms.

### 6.4.2 Earthquake Focal Mechanisms

We first determine the depth of each earthquake as described above and then we fix the depth and invert for focal mechanism. For Mw 5.5-6.5 earthquakes, 15-50s period-band teleseismic P and SH wave packages are fit by grid-searching moment, strike, dip and rake. The waveform fit is insensitive to earthquake duration due to the longer period band than typifies the duration of Mw<6.5 earthquakes. We treat Mw~7 earthquakes slightly differently, as discussed later. Figure 6.4A shows example P and

SH seismograms for the 2005/12/16, 18:32 Mw 6.0 earthquake, sorted by azimuth. Note the clear variation of both P and SH waveform and amplitudes with azimuths, which we use as a constraint on the focal mechanism. P waves are weighted twice as much as SH waves to compensate for the overall smaller amplitudes. Teleseismic SH waves are known to be noisier than P waves due to generally noisier horizontal components and contamination from sPL waves (Helmberger and Engen, 1974), so we have a higher quality control for SH waves. A group of 6 earthquakes close to the coast are chosen to be benchmark events as they are relatively easy to study, even with only P waves. We require that the SH waveform fits have cross correlation coefficients higher than 90% for all the benchmark events. This requirement filtered out about half of the SH records. Figures 6.4A, 6.4B display the best waveform fits and optimal focal mechanism in red for the 2005/12/16, 18:32 Mw 6.0 earthquake.

As mentioned earlier, focal mechanism inversions for shallow earthquakes using long-period surface waves are subject to a significant moment-dip-depth tradeoff (e.g., Kanamori and Given, 1981; Tsai et al., 2011). Since we estimate earthquake depths independently using broadband P waveforms, we only have the moment-dip tradeoff problem to deal with. As there is no theoretical study about this tradeoff for the case when using relatively broadband teleseismic body waves, we performed an empirical check for each earthquake. Figure 6.5A shows the relations between Mw and dip angle for inversions using only P waves (blue dots), SH wave only (red dots) and P+SH waves (yellow dots). The SH-only case has a much stronger moment-dip tradeoff than P-only or P+SH. Also the moment-dip tradeoff for the SH-only case is very severe because the misfits do not change much along the tradeoff curve (flat red curve in Figure 6.5B). However, the P-only case shows a much sharper misfit curve, which means the moment-dip tradeoff is much less significant for P waves. The reason for this is that depth phases pP and sP interfere with each other (opposite-sign) making the waveforms very sensitive to dip-angle. As expected, the P+SH case is dominated by P waves.

Due to the non-linear characteristics of waveform inversion, it is not trivial to assess the accuracy of the result. Here we apply the bootstrapping method to estimate 95% confidence intervals (e.g., Tichelaar and Ruff, 1989). In detail, we independently resample the N (~80) stations used in the inversion M times (where M is a large number, e.g., 10000), each with N stations but with some station duplication and some stations not being sampled. We then analyze each sampled data set in the same way as the original dataset to estimate the source parameters. The confidence intervals and other statistical quantities can be estimated from these M results. Note that our grid-searching methodology requires little additional computation time for the bootstrapping process, because we can store the waveform misfits for each station and focal mechanism in the first grid-search step. In this study, obtaining an accurate fault geometry from earthquake focal mechanism is critical, so we estimate the 95% confidence limits of strike, dip and rake by evaluating the point corresponding to 2.5% from each end of the distribution of the M results (Figure 6.4C, D, E). The M bootstrapping focal mechanisms are also plotted in Figure 6.4B in black to show the rotation angles. While strike and rake have large uncertainties (std ~ 10°), the dip angle is well constrained (Figure 6.4). This behavior is expected for inversions using teleseismic body waves, as shown by the sensitivity test in Figure 6.2.

Because 1D velocity models extracted from a 2D tomography model are used in the inversions, we consider the potential bias caused by the dipping velocity structure on our estimates of the earthquake focal mechanisms, especially dip angles. The west-dipping subducting slab and east-dipping seafloor are the two major dipping structures. To assess the effect of dipping source-side structure on focal mechanism, we conduct a synthetic test. It is not trivial to calculate synthetic seismograms for T$\geq$15s teleseismic body waves and take into account the detailed source-side structure with a dipping water layer and slow sediment layers. We designed a hybrid method

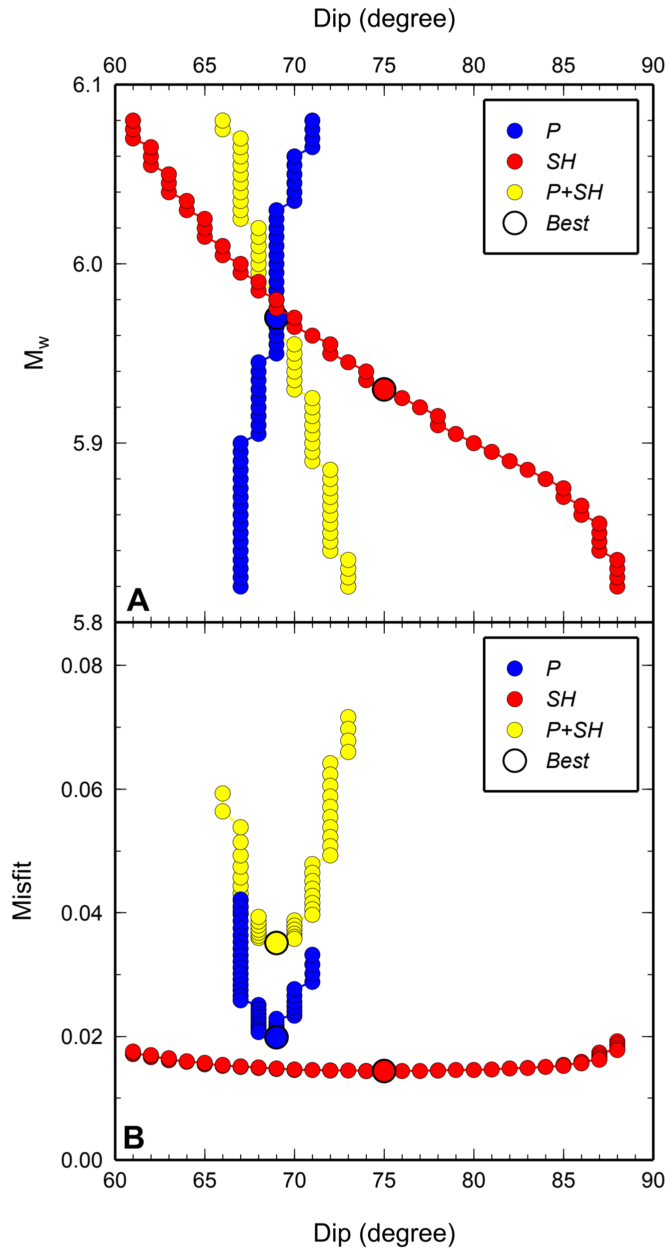


Figure 6.5: Moment-dip tradeoff for teleseismic P and SH waves. (A) The Mw-Dip tradeoff curves for P only, SH only and P+SH in blue, red and yellow dots, respectively. The best solutions with least waveform misfit for each case are indicated by larger dots. (B) The corresponding waveform misfits as a function of dip angle. Colors and sizes of dots are the same as in (A).

which interfaces the Spectral Element Method (SEM, Komatitsch and Tromp, 1999) in the source area with geometrical ray theory elsewhere (Figure 6.6A). More details about this hybrid numerical method will be presented in another paper (Wu et al., in preparation). In the synthetic test, we estimate the focal mechanism and 95% confidence intervals using the same procedures discussed above and result is shown in Figure 6.6B. Ignoring 3D source-side structure causes some scatter in the focal mechanism, but no systematic bias is observed. For the best constrained parameter, the dip angle, the scatter is on the order of 1 degree (Figure 6.6C), smaller than the uncertainties observed for real data (e.g., Figure 6.4D).

### 6.4.3 M~7 Earthquakes

There are three Mw~7 events in our catalog, shown as black beachballs in Figure 6.1: 2003/10/31, 01:06, Mw 6.9; 2005/08/16, 02:46, Mw 7.3; 2011/03/09, 02:45, Mw 7.3. Due to the longer source durations and more complicated source time functions, the depth phases cannot be easily identified or fit to estimate the depths and we therefore use a slightly different approach to modeling these events. We adopt the latitude and longitude of the GCMT centroid and adjust the depths such that they occurred on the assumed reference plate interface. During the focal mechanism inversion, we use a longer period band (25-50s) to ensure the validity of the point source approximation. The 95% confidence intervals are estimated applying the above bootstrapping method.

## 6.5 Results

We studied a total of 28 shallow-angle thrust events (details in Table 6.1), 2 of which are located more than 5km away from the reference plate interface hence considered intraplate, 5 of which are too noisy for body wave waveform modeling due to interference from events close in time so we just adopt their GCMT solutions (orange color

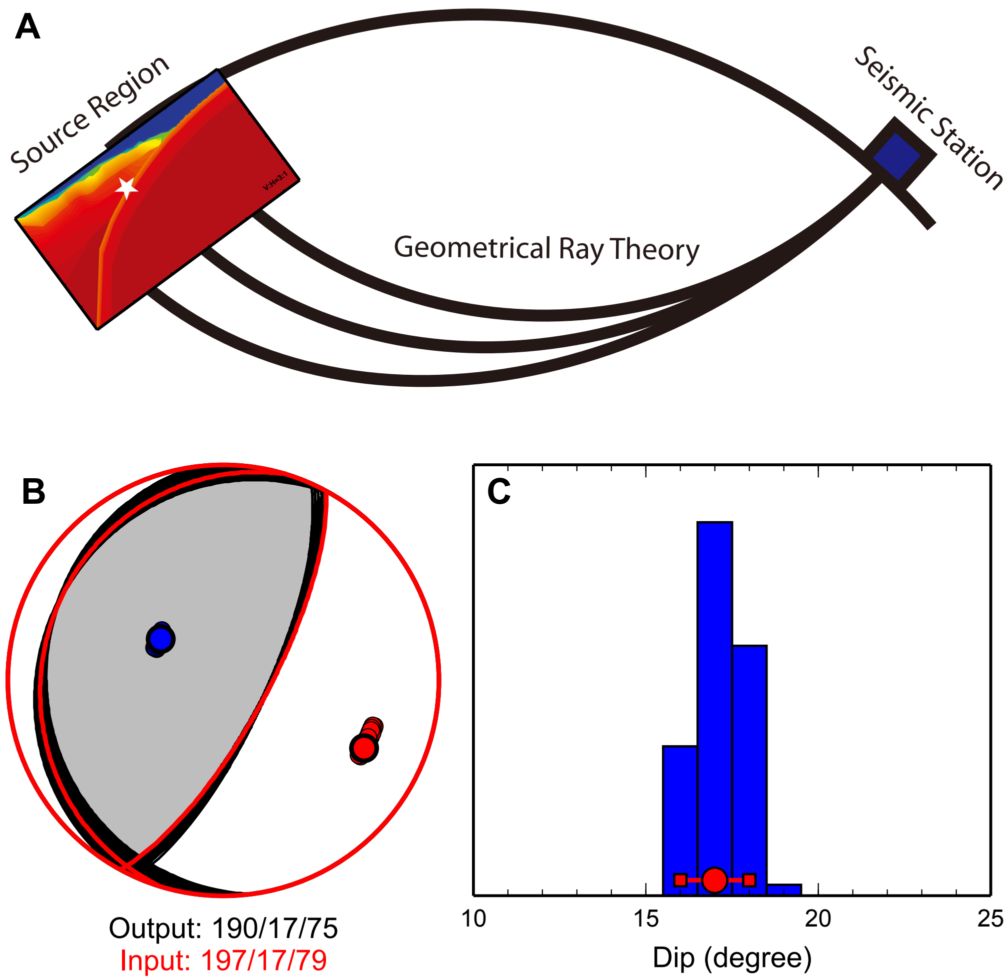


Figure 6.6: Synthetic test of 3D source-side structure's effect on focal mechanism inversion with a hybrid method. (A) Sketch illustrating the hybrid method. In the source region, we use the SEM to fully take into account the 3D structure, including the water layer and slow sediment layers. White star shows the earthquake location. On the boundary of the source region, SEM is interfaced with geometrical ray theory to calculate the teleseismic body waves recorded at seismic stations. (B) The input focal mechanism is shown in red beachball and big dots. The inverted focal mechanisms with bootstrapping results are shown as a black beachballs and small dots. Red and blue dots are P axes and T axes, respectively. (C) Histogram of the inverted dip angles. Red dots are the optimal values. Red squares and red lines indicate the corresponding 95% confidence limits.

in Figure 6.1 and Figure 6.7). Figure 6.7 shows the results for the other 21 events, including the 3 Mw~7 events. Five of these events are aftershocks of the Tohoku-Oki earthquake, and they all occurred downdip of the large slip area. Using the GCMT horizontal locations and the re-estimated depths, these earthquakes are located along the reference plate interface, with significant improvement compared with the locations from routine catalogs shown in Figure 6.1. Since these earthquakes all have shallow-angle thrust mechanisms, we assume that they are interplate earthquakes. This assumption is also supported by their source spectra. Ye et al. (2012) used Empirical Green's Functions to isolate the source spectra for earthquakes in Tohoku-Oki region, and found that these earthquakes had less high-frequency energy than intraplate earthquakes.

If these interplate events occurred on the reference plate interface as shown by the blue line in Figure 6.7A, both their locations and their fault geometry should be consistent. Since the dip angle is the best constrained focal mechanism parameter, we can compare the earthquake dip angles with plate interface dip angles. In Figure 6.7B, the blue line indicates the dip angle calculated from the reference plate interface model, increasing toward the coast. Note the jump of dip angle from 13° to 23° at the kink (marked by the green line in Figure 6.7A). Red and dark gray dots with error bars indicate the earthquake dip angles with 95% confidence limits, for Mw 5.5-6.5 and Mw~7, respectively. Orange dots are the 5 events with only GCMT solutions. For events in the western part of the AA' profile (distance>150 km from the trench, downdip of the kink), earthquake dip angles are relatively consistent with the dip angle of the reference plate interface. However, earthquakes within a distance of 150 km from the trench (the eastern portion of AA', updip of the kink) have systematically larger dip angles than the reference plate interface dip angle, suggesting that they occurred on steeper fault planes. The minimal dip differences are ~5-10 degrees, considering the 95% confidence limits. The dip angles from the GCMT catalog show

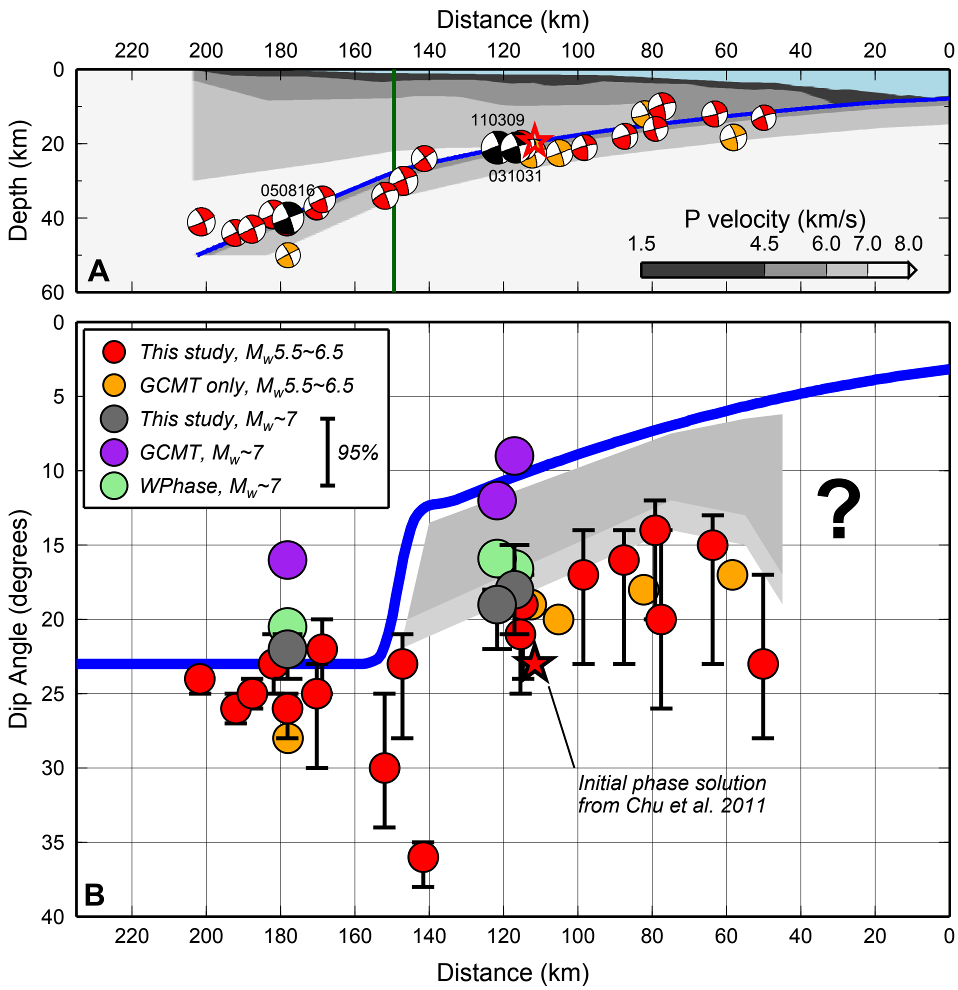


Figure 6.7: (A) Colored beachballs (see the legend in Figure 6.1A) show earthquakes with re-estimated depths and GCMT horizontal locations projected to the AA' profile. Red star indicates the hypocenter of the 2011 Tohoku-Oki earthquake. Green line marks the position of the kink in the reference plate interface model (blue line). (B) The comparison between dip angles from earthquake focal mechanisms (colored dots, see legend and main text for details) and the reference plate interface model (blue line). Note the jump of dip angle from 13° to 23° at the kink. Errorbars show the 95% confidence limits estimated by the bootstrapping method. The GCMT and W-Phase focal mechanisms for the three M7 earthquakes are also shown for comparison. Note the ~7° systematic difference in dip between the GCMT solution and this study. Updip of the kink, the gray zone shows the 5°-10° differences between the earthquake dip angles and the reference plate interface dip angle. The red star indicates the initial phase of the 2011 Tohoku-Oki earthquake modeled as an Mw 4.9 earthquake with a dip angle of 23° (Chu et al., 2011).

Table 6.1: Details of the 28 studied earthquakes. Events with gray shading have only GCMT solutions because they are noisy/complicated for teleseismic body wave waveform modeling. Events with light blue shading are actually intraplate. Events with orange shading are Mw~7 events. Locations are from GCMT catalog and other source parameters are estimated in this study.

| Date (UTC) | Latitude | Longitude | Depth, km | Strike° | Dip° | Rake° | Magnitude |
|---|---|---|---|---|---|---|---|
| **1994/08/14, 09:06** | 38.72 | 142.25 | 37 | 177 | 25 | 66 | 5.75 |
| **1994/08/16, 10:09** | 37.91 | 142.40 | 24 | 184 | 36 | 87 | 5.79 |
| **1999/01/21, 22:02** | 38.55 | 143.05 | 21 | 166 | 18 | 57 | 5.77 |
| **1999/11/15, 01:34** | 38.30 | 142.31 | 48[1] | 202 | 31 | 103 | 5.61 |
| **2002/10/12, 10:59** | 37.82 | 142.69 | 21 | 209 | 18 | 96 | 5.44 |
| **2002/11/03, 03:37** | 38.84 | 142.14 | 39 | 194 | 23 | 78 | 6.35 |
| **2003/10:31, 01:06** | 37.89 | 142.68 | $21^{fixed}$ | 180 | 18 | 67 | 6.89 |
| **2003/11/01, 13:10** | 37.77 | 143.27 | 12 | 209 | 14 | 102 | 5.82 |
| **2005/08/16, 02:46** | 38.24 | 142.05 | $40^{fixed}$ | 190 | 22 | 83 | 7.16 |
| **2005/08/24, 10:15** | 38.55 | 143.24 | 12 | 214 | 18 | 90 | 5.90 |
| **2005/08/30, 18:10** | 38.53 | 143.29 | 10 | 157 | 20 | 46 | 6.12 |
| **2005/12/02, 13:13** | 38.11 | 142.38 | 30 | 173 | 24 | 69 | 6.51 |
| **2005/12/16, 18:32** | 38.47 | 142.21 | 35 | 180 | 22 | 70 | 5.97 |
| **2007/12/25, 14:04** | 38.40 | 142.39 | 34 | 151 | 30 | 51 | 6.07 |
| **2008/12/03, 23:16** | 38.56 | 143.18 | 18 | 180 | 16 | 72 | 5.81 |
| **2008/12/05, 20:03** | 38.53 | 143.27 | 16 | 191 | 13 | 81 | 5.52 |
| **2011/03/09, 02:45** | 38.56 | 142.78 | $21^{fixed}$ | 174 | 19 | 63 | 7.32 |
| **2011/03/09, 18:16** | 38.33 | 142.80 | 20 | 168 | 20 | 58 | 6.00 |
| **2011/03/09, 18:44** | 38.47 | 143.50 | 18.3 | 190 | 17 | 77 | 5.9 |
| **2011/03/09, 21:22** | 38.29 | 142.91 | 22.5 | 195 | 20 | 87 | 6.0 |
| **2011/03/09, 21:24** | 38.27 | 142.82 | 22.6 | 191 | 19 | 80 | 6.5 |
| **2011/03/10, 08:08** | 38.53 | 143.61 | 13 | 159 | 23 | 53 | 5.66 |
| **2011/03/12, 23:24** | 38.05 | 141.72 | 16[2] | 141 | 27 | 57 | 6.02 |
| **2011/03/13, 09:52** | 38.90 | 142.20 | 50.0 | 180 | 28 | 71 | 5.6 |
| **2011/03/25, 11:36** | 38.78 | 142.17 | 41 | 177 | 26 | 67 | 6.18 |
| **2011/03/31, 07:15** | 38.97 | 142.05 | 44 | 191 | 26 | 77 | 5.98 |
| **2011/07/23, 04:34** | 38.96 | 142.10 | 43 | 185 | 25 | 73 | 6.29 |
| **2011/07/24, 18:51** | 37.70 | 141.66 | 41 | 205 | 24 | 90 | 6.26 |

[1]Too deep to be on the plate interface. [2]Too shallow to be on the plate interface.

a similar trend (Figure 6.8), except for the three Mw~7 events (purple dots in Figure 6.7B) which we discuss in more detail later. In addition, the initial phase of the Tohoku-Oki earthquake can be modeled as an Mw 4.9 shallow-angle thrust event as shown by Chu et al. (2011). By modeling its teleseismic short period (0.5-2Hz) P waveform, Chu et al. (2011) show that this beginning event also has an anomalous dip angle of 23° (red star in Figure 6.7).

The GCMT dip angles for the three Mw~7 events (purple dots in Figure 6.7B) are all smaller than our inverted dip angles (gray dots in Figure 6.7B) by ~7 degrees. Note that for the two shallower events (2003/10/31, 2011/03/09), the GCMT dip angles are actually consistent with the reference plate interface dip angle, while for the deeper event (2005/08/16) the GCMT dip angle is 7 degrees smaller than the reference plate interface. It should be noted that the GCMT depths for the two shallower events are 15km and 14.1km respectively, ~6km shallower than the reference plate interface depth (~21km) based on their centroid locations. Due to the moment-dip-depth tradeoff, long-period moment tensor inversion could have significant dip angle bias due to the depth bias. To explore this problem, we conducted W-Phase moment tensor inversions for the three events and tested the effect of depth (Kanamori and Rivera, 2008; Duputel et al., 2012). Figure 6.9 shows clear depth-dependence of dip angle and moment for the 2011/03/09 Mw 7.3 earthquake. If the depth is set above the plate interface, at 16km, the W-Phase dip angle is about 11.5°, consistent with the GCMT solution; if depth is set at the plate interface, 21km, the W-Phase dip angle is about 16°, close to our inverted result. The W-Phase solutions for the three Mw~7 events with depths fixed at the reference plate interface are shown in Figure 6.7B as light green dots. For the deeper 2005/08/16 Mw 7.2 earthquake, the GCMT depth is 37 km, not significantly different from the reference plate interface depth of 40 km, but still the GCMT dip angle (16°) is smaller than our inverted result (22°) and our W-Phase result (21°). For this earthquake, we have additional information

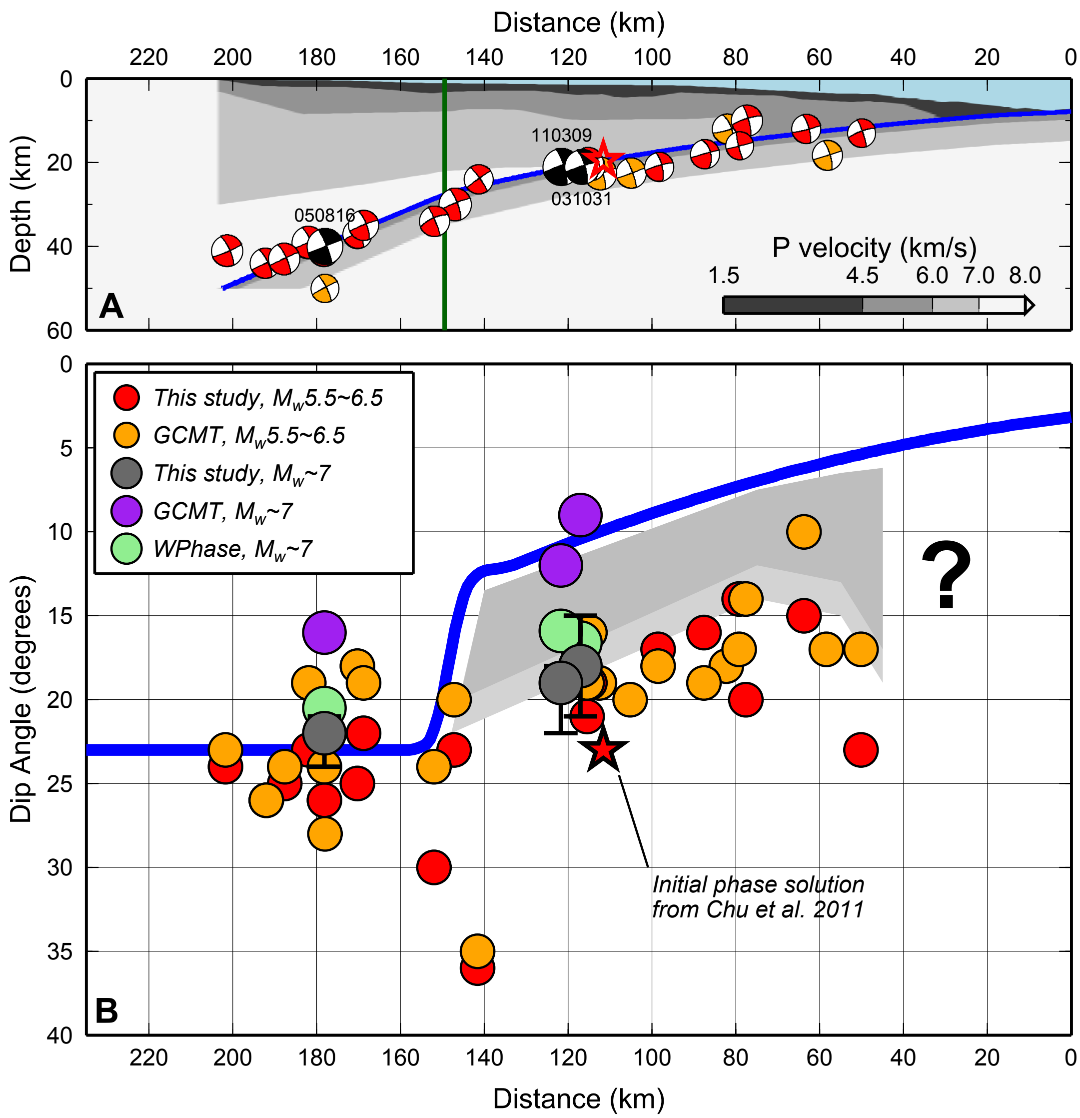


Figure 6.8: The same as Figure 7, except that all events' GCMT dip angles are shown for comparison.

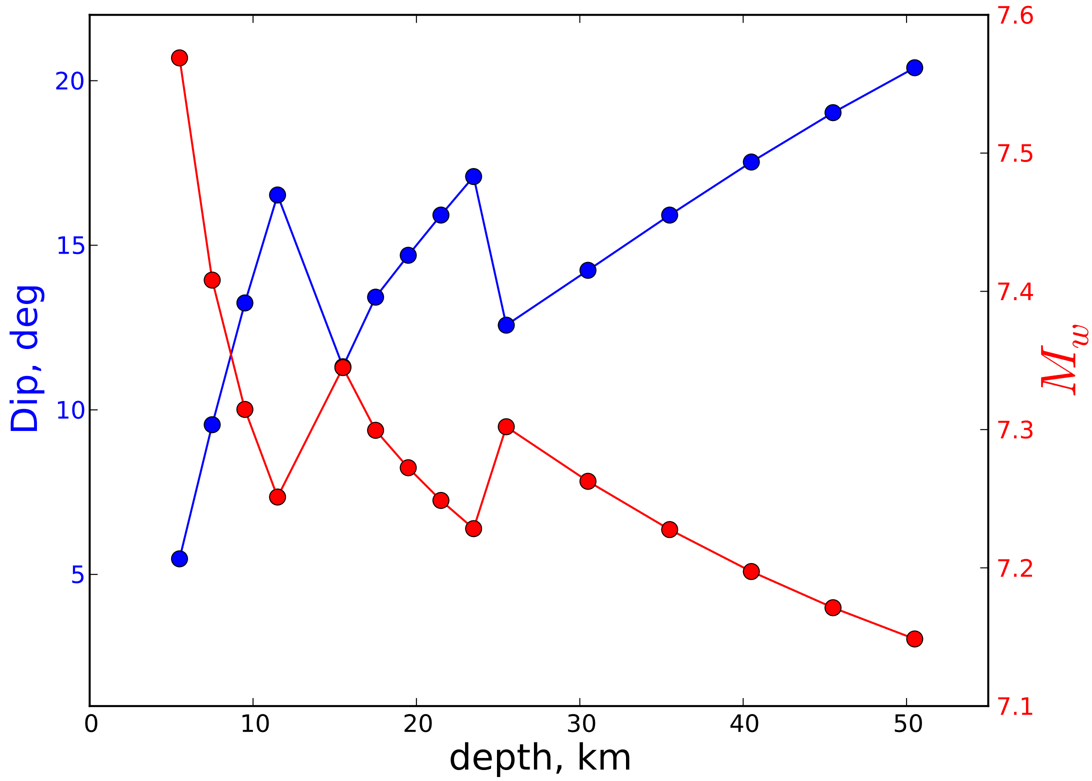


Figure 6.9: The moment-dip-depth tradeoff for the 2011/03/09 Mw7.4 foreshock using W-Phase inversion.

from regional and local observations. The NIED F-Net moment tensor solution using regional waveforms for this earthquake has a dip angle 23°. Using an OBS network above the source area, Hino et al. (2006) show that this earthquake's aftershock sequence formed a well-defined plane, with a dip angle of 23°.

In summary, although the interplate earthquakes in this area occurred close to the reference plate interface imaged in previous seismic surveys, there is a clear depth-dependent dip angle discrepancy. Downdip of the break-point of slope (vertical green line in Figure 6.7), earthquake dip angles are consistent with the reference plate interface dip angle; on the other hand, updip of the kink, all the earthquakes, including the initial phase of the 2011 Tohoku-Oki earthquake, have 5°-10° steeper dip angles than the reference plate interface. Within the 95% confidence intervals, no clear lateral variation or moment dependence is observed within our study area (within 60km from AA') and magnitude range (Mw 5.5-7.5).

## 6.6 Discussion

We discuss three possible explanations for the observed dip angle discrepancy. Both pros and cons for each explanation will be presented.

### 6.6.1 Model I: Segmented fault along dip

The reference plate interface model derived by Miura et al. (2005) has a kink at ~150km from the trench (green line in Figure 6.7A). The dip angle jumps from 13° to 23° at the kink. Using a similar dataset, Ito et al. (2005) presented a slightly different plate interface model (green line in Figure 6.10A) with an additional kink at ~80km from the trench. The dip angles of the three segments separated by the two kinks are 4°, 13° and 23°, respectively. Most of the events with steeper dip angles are located in the middle segment and have an average dip angle of 17°. Our model I for the dip angle discrepancy uses the same locations of the two kinks as in Ito et al. (2005), but has the middle segment dipping 17° to explain the earthquake dip angles (red line in Figure 6.10A). We have little constraint on the dip angle of the updip segment because very few earthquakes ruptured there except the 2011 Tohoku-Oki earthquake, so we set the dip angle to be 3°, the same as the ocean floor dip just outside the trench. Compared to the plate interface model by Ito et al. (2005), the updip kink is sharper (difference in dip increases from 9° to 14°) and the downdip kink is smoother (difference in dip decreases from 10° to 6°).

In this model, the 2011 Tohoku-Oki earthquake nucleated in the middle segment (red star in Figure 6.10A), but ruptured all the way to the trench with large slip (>40 m) in the outer wedge (e.g., Lay et al., 2011; Wei et al., 2012). Complete stress release is inferred by the occurrence of many aftershocks with normal faulting mechanisms (Hasegawa et al., 2011). To explain these unique features and the long recurrence time, Fukao et al. (2011) proposed a model in which the inner and outer wedges are separated by a strong seismic barrier. In the pre-seismic stage, the seismic barrier prevented rupture in the inner wedge from propagating into the outer wedge, and accumulated stress, which was eventually released during the Tohoku-Oki earthquake. The very low dynamic basal friction in the outer wedge caused complete stress drop and very large slip. In our Model I, the sharp kink separating the inner wedge and outer wedge could act as the proposed strong seismic barrier.

The difficulty with Model I is the significant depth difference from the previous plate interface models. For distances $>$ 120 km from the trench, Model I is ~5km deeper than the plate interface model by Miura et al. (2005) (red and blue lines in Figure 6.10A), and ~3km deeper than the model by Ito et al. (2005) (red and green lines in Figure 6.10A), which are significant differences for a seismic profile with both reflection and refraction data. Unfortunately, earthquake depth determination using either OBS data or teleseismic depth phases usually rely on the assumption of

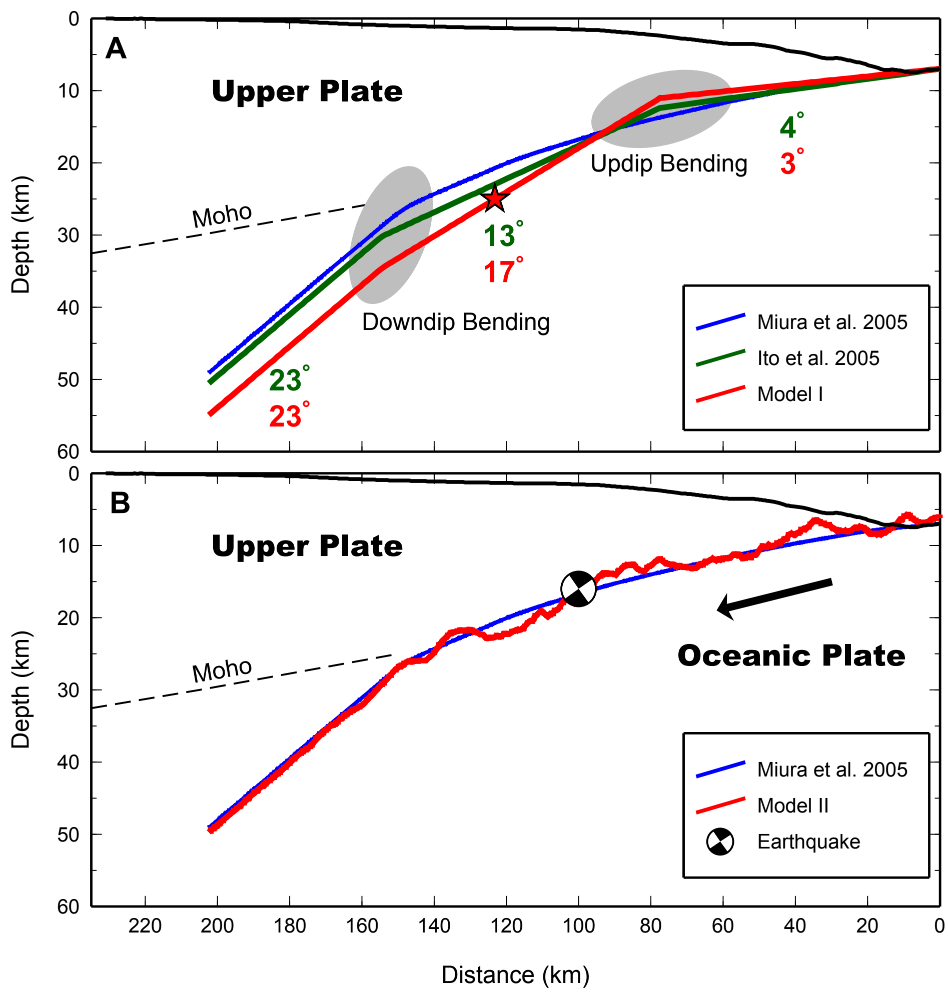


Figure 6.10: Sketch of Model I and Model II. (A) Model I: Oceanic plate undergoes two points with significant changes in dip angle. The blue line shows the reference plate interface model from Miura et al. (2005). The green line indicates a slightly modified plate interface model with two kinks from Ito et al. (2005) using similar dataset. The green numbers below each segment are the dip angles, respectively. Model I is illustrated as the red line, with dip angles shown below in red numbers. The red star shows the hypocenter of the 2011 Tohoku-Oki earthquake. (B) Model II: plate interface with topography (red line). The beachball shows an earthquake occurring on the front side of a local topographic high. Note the smoother interface topography at depths greater than the Moho.

Vp/Vs ratio (e.g., Suzuki et al., 2012) and hence cannot distinguish these differences conclusively.

### 6.6.2 Model II: Rough plate interface

In Model II, we interpret these earthquakes with steeper dip angles as indicators of rough fault topography, as schematically indicated by the red line in Figure 6.10B. If the plate interface has rough topography at different scales, small events may tend to occur on the front sides of local fault topography due to concentration of stress or particular orientation of the local stress tensor. These events will have steeper dip angles than the average fault dip angle. Most of the earthquakes analyzed in this study have Mw~6, so the fault patch dimensions are on the order of 10 km, assuming a circular rupture area and "reasonable" stress drop (~3MPa, Kanamori and Anderson, 1975). Consequently, 5° to 10° differences in dip angle imply heights of about 1 km. Topography of this scale at depth may be hard to image in seismic reflection or refraction profiles. The consistent dip angle downdip of the kink (Figure 6.7B) requires the topography to be smoother, potentially due to increased temperature, or stiffer ambient mantle material beyond the Moho discontinuity that may serve to reduce any fault roughness (Figure 6.10B).

Since the earthquakes with steeper dip angles occurred in the area with large coseismic slip in the Tohoku-Oki earthquake, Model II implies that the ruptured interface during the Tohoku-Oki earthquake was rough, and thus potentially more strongly coupled (i.e., requiring a higher stress to fail seismically) than surrounding regions. This strong coupling could explain the inferred high stress drop and by extension the long recurrence time between events. Using highly accurate relative locations, Hasegawa et al. (2007) also suggested that a geometrically irregular plate interface could explain their observations of the fault plane dip of repeating earthquakes which are believed to lie on the megathrust. Their interpretation called upon a locally coupled spot embedded in a larger creeping portion of the fault.

However, the physical origin of this local fault topography is uncertain. We note that the dimension of the smaller earthquakes is comparable to that of small seamounts (with moderate footprint, but relatively smooth topography). In other subduction margins, subducted seamounts are thought to strongly enhance plate coupling (Cloos, 1992; Scholz and Small, 1997), although some studies suggest the opposite (Mochizuki et al., 2008; Wang and Bilek, 2011). This mechanism has been previously called upon to explain the rupture regions of large earthquakes in the Costa Rica subduction zone (Bilek et al., 2003) and behavior of the rupture pattern of the 1946 M 8.1 Nankaido earthquake (Kodaira et al., 2000). Several seamounts are known to have subducted (Mochizuki et al., 2008) or are presently in the process of being subducted in the regions proximal to the 2011 Tohoku-Oki earthquake (Figure 6.11A). The horst and graben structures formed in the top of the descending plate in response to extension induced as the plate bends into the subduction zone may be another candidate for the inferred fault roughness. Such structures are clearly evident to the east of the trench in high-resolution bathymetry of the area (Figure 6.1A) and have been imaged at the shallow subduction interface by previous seismic surveys (e.g., Von Huene and Cullota, 1989; Tsuru et al., 2000). The possibility of induced topography after subduction cannot be ruled out either.

One difficulty of Model II comes from the two Mw~7 events with steeper dip angles (Figure 6.7B). Clearly, Mw~7 events have larger rupture areas than their smaller brethren. For example, Shao et al. (2011a) show that the large-slip patch of the 2011/03/09 Mw 7.3 foreshock is about 30km along dip. Consequently, 5° to 10° difference in dip angle implies a height of about 3 km with respect to the background. Previous seismic profiles did not run right above the two events so it is unclear whether topography of this scale exists. However, the inferred topography of 3km is comparable to the un-subducted seamounts offshore from Iwaki, such as the Kashima

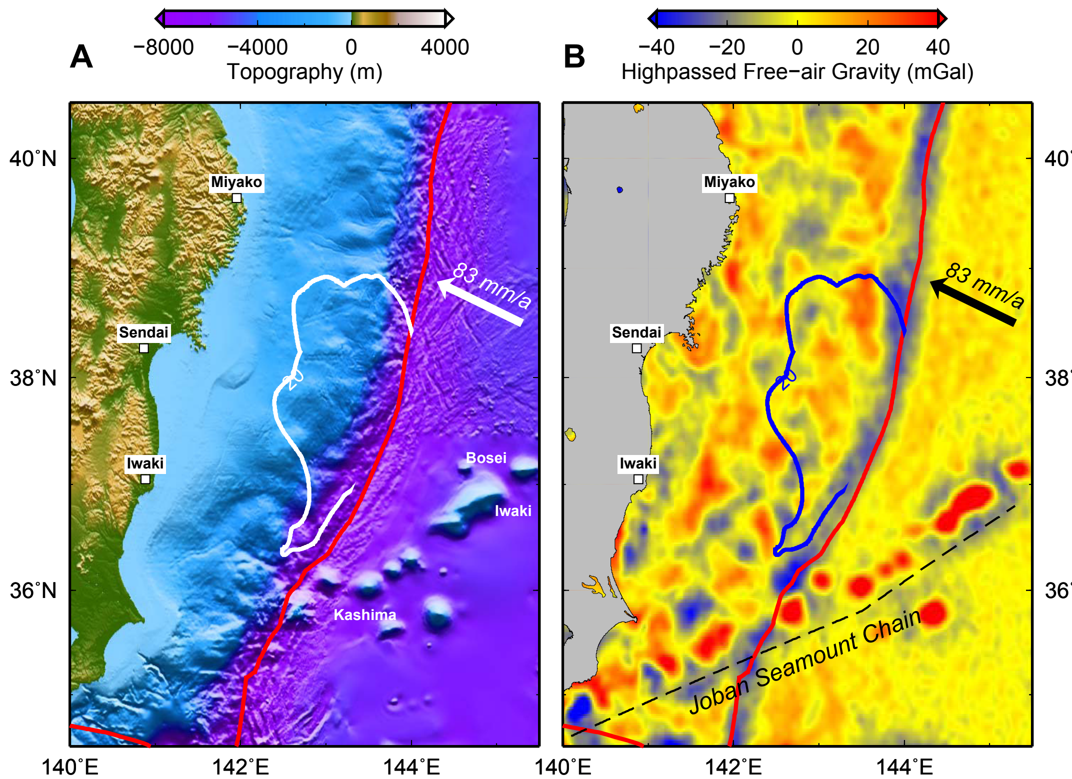


Figure 6.11: (A) Topography and bathymetry map of northeast Japan with identified seamounts. Red lines indicate the subduction plate boundaries and white arrow indicates the direction of convergence between the Pacific Plate and northeast Japan. The white line indicates the 20 m contour of co-seismic slip of the 2011 Tohoku-Oki earthquake (Wei et al., 2012). (B) Free air gravity field offshore Tohoku. The gravity field has been high-passed filtered with a Gaussian filter (wavelength < 50km). Dashed line indicates the strong positive anomalies of the Joban Seamount Chain and its extension under the forearc to just offshore the Boso Peninsula. The blue line indicates the 20m contour of co-seismic slip of the 2011 Tohoku-Oki earthquake. The black arrow indicates the direction of convergence between the Pacific Plate and northeast Japan.

Tablemount and Iwaki Seamount (Figure 6.11A). These seamounts and others stand in a line that extends northeastward from the Japan Trench along the Joban Seamount Chain, which is clearly visible in a highpassed version (wavelengths less than ~50 km) of the free-air gravity field (Figure 6.11B). We also observed strong bathymetric disturbance and positive gravity anomalies in the southwestward extension of the Joban Seamount Chain under the forearc to just offshore. However, in the source area of the 2011 Tohoku-Oki earthquake (marked by the 20m co-seismic slip contour in Figure 6.11), we do not observe a significant bathymetric disturbance or gravity anomaly of similar amplitude. If subducted seamounts are the reason for the inferred rough fault surface, they must be sufficiently small in amplitude or of neutral enough density as to not have an obvious signature in the bathymetry or gravity field.

Model II makes several other predictions, which cannot be tested with the available observations. First, a rough plate interface may produce more diverse dip angles for smaller earthquakes (Mw<5.5), rather than always steeper. Second, the dip angle difference for Mw>5.5 should be moment-dependent. As the rupture area increases, the average dip angle should converge to the background dip angle as imaged in seismic surveys. Within the 95% confidence interval, we are currently unable to observe such dependence.

### 6.6.3 Model III: Subfaults

In Model III, the earthquakes with steeper dip angles do not occur on the plate interface as imaged by Miura et al. (2005), but instead occur on steeper nearby subfaults (Figure 6.12A). While such subfaults have not been imaged, if there is no strong velocity contrast across these subfaults, previous seismic surveys might not be able to image them. Since the Mw~6 earthquake depths may only be systematically shallower than the plate interface by ~1km in Model III, current earthquake location accuracy is insufficient to determine if they are off the main fault. For the two Mw~7 earthquakes, the centroid depth differences could be more significant, but their depths are even harder to estimate due to their longer durations.

These steeper subfaults might reflect deep basal duplexes, formed by thrust sheets bounded from below by the plate interface and from above by a shallower décollement. Deep extensive underplating through duplexes has been observed in present and ancient accretionary prisms, as in the Costa Rica forearc, the Kodiak Islands in Alaska and the Kii Peninsula in southwest Japan (e.g., Hashimoto and Kimura, 1999; Sample and Fisher, 1986; Silver et al., 1985) and have been successfully reproduced by sandbox experiments (Gutscher et al., 1998; Kukowski et al., 2002).

Although the suggested geometry resembles splay fault-main fault junction, these subfaults may not be related to splay faults in the forearc wedge. In the same region as this study, Tsuji et al. (2011) find splay faults only within ~60 km of the trench (outer wedge), while most of the events studied in this paper are >60 km away from the trench (inner wedge). The outer wedge and inner wedge are separated by a steeply dipping normal fault. Seismic reflection profiles in other regions, such as the Nankai subduction zone (Park et al., 2002) and Sunda margin (Kopp and Kukowski, 2003), show similar widths of outer wedges containing extensive splay faulting. Wang and Hu (2006) proposed that the inner wedge generally stays in the stable regime, while the outer wedge undergoes active deformation.

Considering the uncertainty of our dataset, here we only explore a simple mechanical model with a uniform stress field. The maximum and minimum principal stresses $\sigma 1$ and $\sigma 3$ are assumed to be sub-horizontal and sub-vertical, respectively, perpendicular to the trench (Figure 6.12B). Since all of the earthquakes with steeper dip angles occurred before the 2011 Tohoku-Oki earthquake, this assumption is reasonable (e.g., Hasegawa et al., 2011). Red line OA in Figure 6.12B indicates the stress state of the subfaults. Since the main fault's dip angle is on average 7.5° (5°-10°) smaller than the subfaults, we need to rotate OA in Figure 6.12B by 15° to OB to obtain the shear

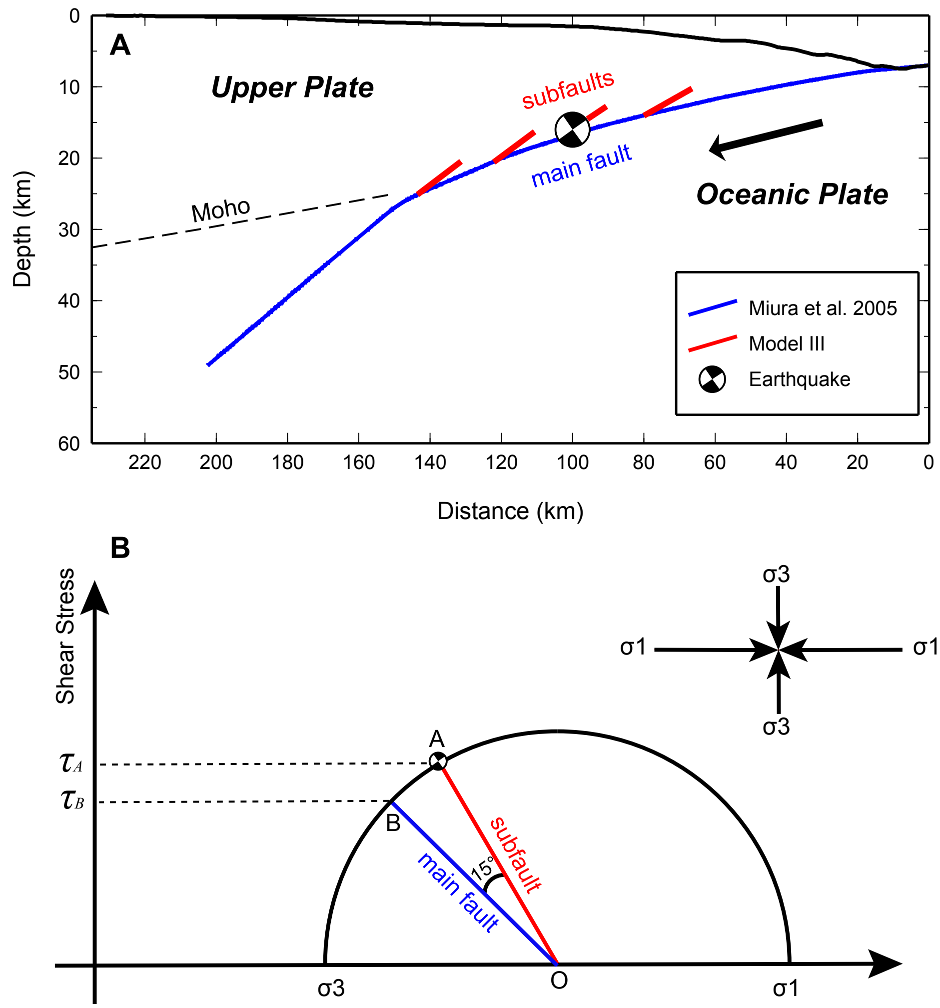


Figure 6.12: Model III: Subfaults. (A) Earthquakes with steeper dip angles (black beachball) occurred on steeper subfaults (red lines) near the main fault (blue line). Note the absence of subfaults beyond the Moho or the kink. (B) Mohr diagram showing a simple mechanical model consistent with earthquakes on the steeper dipping subfaults (red lines and black beachball at point A), rather than on the main fault (blue, point B).

stress on the main fault. With the assumed stress orientation, the shear stress on the subfault ($\tau_A$ in Figure 6.12B) is always larger than the shear stress on the main fault ($\tau_B$). Thus, earthquakes can occur on the subfaults rather than on the nearby main fault even if the strength of the main fault is slightly smaller than that of the subfaults. However, since the average difference in the dip angles is only 7.5 degrees, the difference in shear stress ($\tau_A - \tau_B$) is also small. This suggests that the main fault's strength is actually comparable to that of the nearby subfaults.

One possible interpretation of this behavior is as follows. Since observations of the 2011 Tohoku-Oki earthquake suggest high stress drop, the main fault may have healed to a relatively strong fault during the interseismic period preceding the 2011 Tohoku-Oki earthquake. The mega-thrust fault zone may not be a well-defined interface, but may be a zone with a finite thickness in which both the "main fault" and the "subfaults" exist (e.g., basal duplexes). As commonly suggested for weak mega-thrust faults (e.g., Magee and Zoback, 1993; Wang and Suyehiro, 1999) and weak strike-slip faults (e.g., Hardebeck and Hauksson, 1999), relatively uniform pore-pressure and/or frictional properties within this fault zone may cause them to have about the same strength. To contain the anomalous M7 earthquakes, the fault zone would need to be ~3km thick, at least locally. This kind of fault zone structure may have been imaged in some subduction zones, such as the 3-5km thick ultra-slow velocity layer in southern Mexico (Song et al., 2009), and the low velocity zone imaged in Cascadia (Calvert, et al., 2011). One possible scenario is that most earthquakes before the 2011 Tohoku-Oki earthquake preferentially occurred on the subfaults as discussed above until finally the main fault failed either by triggering from the subfault earthquakes or by local weakening on the main fault.

## 6.7 Conclusions

In this paper, we determine the locations and focal mechanisms of Mw 5.5-7.5 earthquakes in the source region of the 2011 Tohoku-Oki earthquake using teleseismic waveforms. Although the interplate earthquakes in this area occurred close to the plate interface imaged in previous seismic surveys, there is a clear depth-dependent dip angle discrepancy. All the earthquakes in the region that experienced large-slip during the Mw 9.1 event, including the initial phase of the 2011 Tohoku-Oki earthquake, have 5°-10° steeper dip angles than the reference plate interface dip angle. This discrepancy cannot be explained by a single smooth plate interface. We provide three possible explanations.

In Model I, the oceanic plate undergoes two distinct changes in dip. These two geometric discontinuities may have acted as strong seismic barriers in previous seismic ruptures, but may have failed in and contributed to the Tohoku-Oki earthquake's rupture.

In Model II, the discrepancy of dip angles is due to a rough plate interface, which in turn may be the underlying cause for the overall strong coupling and concentrated energy-release.

In Model III, the earthquakes with steeper dip angles did not occur on the plate interface imaged before, but on nearby steeper subfaults. Since the differences in dip angle are on average only 7.5 degrees, this explanation implies that the main fault has almost the same strength as the nearby subfaults, rather than much weaker. A relatively uniform thick fault zone with both the "main fault" and the "subfaults" inside is consistent with this model.

To distinguish between these different models, detailed study of seismic structure, gravity and magnetic anomalies, especially in the source areas of the anomalous M7 earthquakes, are necessary. Since the physical reason for this dip angle discrepancy is still unclear, approaches relying solely on earthquake focal mechanisms to constrain plate interface geometry may be problematic, as previously pointed out by Hayes et al. (2009).

## Acknowledgement

We thank Seiichi Miura, Narumi Takahashi, Aki Ito and Ryota Hino for providing their velocity models or earthquake catalog. We thank Robert Graves, another anonymous USGS internal reviewer and two anonymous reviewers for their comments that improved the manuscript. The Incorporated Research Institutions for Seismology (IRIS) provided the seismic data. All figures are made with GMT. This work is supported by the National Science Foundation through grant number EAR-1142020.

## References

Ammon, C.J., Lay, T., Kanamori, H., Cleveland, M., 2011. A rupture model of the 2011 off the Pacific coast of Tohoku Earthquake. Earth Planets Space 63, 693-696.

Bilek, S.L., Schwartz, S.Y., DeShon, H.R., 2003. Control of seafloor roughness on earthquake rupture behavior. Geology 31, 455.

Brocher, T.M., 2005. Empirical relations between elastic wavespeeds and density in the Earth's crust. Bull. Seismol. Soc. Am. 95, 2081-2092.

Calvert, A. J., Preston, L. A., Farahbod, A. M., 2011. Sedimentary underplating at the Cascadia mantle-wedge corner revealed by seismic imaging. Nature Geoscience, 4, 545-548

Chu, R., Wei, S., Helmberger, D.V., Zhan, Z., Zhu, L., Kanamori, H., 2011. Initiation of the great Mw 9.0 Tohoku-Oki earthquake. Earth Planet. Sci. Lett. 308.

Cloos, M., 1992. Thrust-type subduction-zone earthquakes and seamount asperities: A physical model for seismic rupture. Geology 20, 601.

DeMets, C., Gordon, R.G., Argus, D.F., 2010. Geologically current plate motions. Geophys. J. Int. 181, 1-80.

Duputel, Z., Rivera, L., Kanamori, H., Hayes, G., 2012. W-phase fast source inversion for moderate to large earhquakes (1990-2010). Geophys. J. Int. 189(2), 1125-1147.

Fukao, Y., Hori, T., Kodaira, S., 2011. The 2011 Mw9.0 Tohoku-Oki Earthquake: Joint occurrence of tectonic stress-driven and lithostatic stress-driven slips along the plate boundary, AGU 2011 Fall Meeting, San Francisco, Calif.

Gutscher, M.-A., Kukowski, N., Malavieille, J., Lallemand, S., 1998. Episodic imbricate thrusting and underthrusting: Analog experiments and mechanical analysis applied to the Alaskan Accretionary Wedge. J. Geophys. Res. 103, 10161-10176.

Hardebeck, J. L., Hauksson, E., 1999. Role of fluids in faulting inferred from stress field signatures. Science, 285, 236-239.

Hasegawa, A., Uchida, N., Igarashi, T., Matsuzawa, T., Okada, T., Miura, S., Suwa, Y., 2007. Asperities and quasi-static slips on the subducting plate boundary east off Tohoku, NE Japan. SEIZE volume, Columbia Univ. Press.

Hasegawa, A., Yoshida, K., Okada, T., 2011. Nearly complete stress drop in the 2011 A/w 9.0 off the Pacific coast of Tohoku Earthquake. Earth Planets Space 63, 703.

Hashimoto, Y., Kimura, G., 1999. Underplating process from melange formation to duplexing: Example from the Cretaceous Shimanto Belt, Kii Peninsula, southwest Japan. Tectonics 18, 92-107.

Hayes, G.P., Wald, D.J., Keranen, K., 2009. Advancing techniques to constrain the geometry of the seismic rupture plane on subduction interfaces a priori: Higher-order functional fits. Geochem. Geophys. Geosyst 10, Q09006.

Helmberger, D.V., Engen, G.R., 1974. Upper mantle shear structure. J. Geophys. Res. 79, 4017-4028.

Hino, R., Yamamoto, Y., Kuwano, A., Nishino, M., Kanazawa, T., Yamada, T., Nakahigashi, K., Mochizuki, K., Shinohara, M., Minato, K., 2006. Hypocenter distribution of the main-and aftershocks of the 2005 Off Miyagi Prefecture earthquake located by ocean bottom seismographic data. Earth Planets Space 58, 1543.

Ide, S., Baltay, A., Beroza, G.C., 2011. Shallow Dynamic Overshoot and Energetic Deep Rupture in the 2011 Mw 9.0 Tohoku-Oki Earthquake. Science 332, 1426-1429.

Ito, A., Fujie, G., Miura, S., Kodaira, S., Kaneda, Y., Hino, R., 2005. Bending of the subducting oceanic plate and its implication for rupture propagation of large interplate earthquakes off Miyagi, Japan, in the Japan Trench subduction zone. Geophys. Res. Lett. 32, L05310.

Kagan, Y.Y., 2003. Accuracy of modern global earthquake catalogs. Phys. Earth Planet. In. 135, 173-209.

Kanamori, H., Anderson, D.L., 1975. Theoretical basis of some empirical relations in seismology. Bull. Seismol. Soc. Am. 65, 1073.

Kanamori, H., Given, J.W., 1981. Use of long-period surface waves for rapid determination of earthquake-source parameters. Phys. Earth Planet. In. 27, 8-31.

Kanamori, H., Rivera, L., 2008. Source inversion of W phase: speeding up seismic tsunami warning. Geophys. J. Int. 175, 222-238.

Kikuchi, M., Kanamori, H., 1982. Inversion of complex body waves. Bull. Seismol. Soc. Am. 72, 491-506.

Komatitsch, D., Tromp, J., 1999. Introduction to the spectral element method for three-dimensional seismic wave propagation. Geophys. J. Int. 139, 806-822.

Kodaira, S., Takahashi, N., Nakanishi, A., Miura, S., Kaneda, Y., 2000. Subducted seamount imaged in the rupture zone of the 1946 Nankaido earthquake. Science 289, 104.

Koper, K.D., Hutko, A.R., Lay, T., Ammon, C.J., Kanamori, H., 2011. Frequency-dependent rupture process of the 2011 Mw 9.0 Tohoku Earthquake: Comparison of short-period P wave backprojection images and broadband seismic rupture models. Earth Planets Space 63, 599-602.

Kopp, H., Kukowski, N., 2003. Backstop geometry and accretionary mechanics of the Sunda margin. Tectonics 22, 1072.

Kukowski, N., Lallemand, S.E., Malavieille, J., Gutscher, M.A., Reston, T.J., 2002. Mechanical decoupling and basal duplex formation observed in sandbox experiments with application to the Western Mediterranean Ridge accretionary complex. Mar. Geol. 186, 29-42.

Lay, T., Ammon, C.J., Kanamori, H., Xue, L., Kim, M.J., 2011. Possible large near-trench slip during the 2011 Mw 9.0 off the Pacific coast of Tohoku Earthquake. Earth Planets Space 63, 687-692.

Lay, T., Kanamori, H., Ammon, C.J., Koper, K.D., Hutko, A.R., Ye, L., Yue, H., Rushing, T.M., 2012. Depth-varying rupture properties of subduction zone megathrust faults. J. Geophys. Res. 117, B04311.

Magee, M. E., Zoback, M. D., 1993. Evidence for a weak interplate thrust fault along the northern Japan Subduction zone and implications for the mechanics of thrust faulting and fluid expulsion. Geology, 21, 809-812.

Minoura, K., Imamura, F., Sugawara, D., Kono, Y., Iwashita, T., 2001. The 869 Jogan tsunami deposit and recurrence interval of large-scale tsunami on the Pacific coast of northeast Japan. J. Natural Disaster Sci. 23, 83.

Miura, S., Takahashi, N., Nakanishi, A., Tsuru, T., Kodaira, S., Kaneda, Y., 2005. Structural characteristics off Miyagi forearc region, the Japan Trench seismogenic zone, deduced from a wide-angle reflection and refraction study. Tectonophysics 407, 165-188.

Mochizuki, K., Yamada, T., Shinohara, M., Yamanaka, Y., Kanazawa, T., 2008. Weak interplate coupling by seamounts and repeating M~ 7 earthquakes. Science 321, 1194.

Ozawa, S., Nishimura, T., Suito, H., Kobayashi, T., Tobita, M., Imakiire, T., 2011. Coseismic and postseismic slip of the 2011 magnitude-9 Tohoku-Oki earthquake. Nature 475, 373-376.

Park, J.O., Tsuru, T., Kodaira, S., Cummins, P.R., Kaneda, Y., 2002. Splay fault branching along the Nankai subduction zone. Science 297, 1157.

Sample, J., Fisher, D., 1986. Duplex accretion and underplating in an ancient accretionary complex, Kodiak Islands, Alaska. Geology 14, 160-163.

Sato, M., Ishikawa, T., Ujihara, N., Yoshida, S., Fujita, M., Mochizuki, M., Asada, A., 2011. Displacement Above the Hypocenter of the 2011 Tohoku-Oki Earthquake. Science 332, 1395.

Scholz, C.H., Small, C., 1997. The effect of seamount subduction on seismic coupling. Geology 25, 487.

Shao, G., Ji, C., Zhao, D., 2011a. Rupture process of the 9 March, 2011 Mw 7.4 Sanriku-Oki, Japan earthquake constrained by jointly inverting teleseismic waveforms, strong motion data and GPS observations. Geophys. Res. Lett. 38, L00G20.

Shao, G., Li, X., Ji, C., Maeda, T., 2011b. Focal mechanism and slip history of the 2011 Mw 9.1 off the Pacific coast of Tohoku Earthquake, constrained with teleseismic body and surface waves. Earth Planets Space 63, 559.

Silver, E.A., Ellis, M.J., Breen, N.A., Shipley, T.H., 1985. Comments on the growth of accretionary wedges. Geology 13, 6-9.

Simons, M., Minson, S.E., Sladen, A., Ortega, F., Jiang, J., Owen, S.E., Meng, L., Ampuero, J.-P., Wei, S., Chu, R., Helmberger, D.V., Kanamori, H., Hetland, E., Moore, A.W., Webb, F.H., 2011. The 2011 Magnitude 9.0 Tohoku-Oki Earthquake: Mosaicking the Megathrust from Seconds to Centuries. Science 332, 1421-1425.

Song, T.-R. A, Helmberger, D.V., Brudzinski, M.R., Clayton, R.W., Davis, P., Perez-Campos, X., Singh, S.K., 2009, Subducting slab ultra-slow velocity layer coincident with silent earthquakes in southern Mexico, Science, 324, 502–505.

Suzuki, K., Hino, R., Ito, Y., Suzuki, S., Inazu, D., Iinuma, T., Fujimoto, H., Shinohara, M., Kaneda, Y., 2012. Seismicity near hypocenter of the 2011 off the Pacific coast of Tohoku earthquake deduced by using Ocean Bottom Seismographic data. Earth Planets Space, 64, 1125–1135.

Takahashi, N., Kodaira, S., Nakanishi, A., Park, J.-O., Miura, S., Tsuru, T., Kaneda, Y., Suyehiro, K., Kinoshita, H., Hirata, N., Iwasaki, T., 2002. Seismic structure of western end of the Nankai trough seismogenic zone. J. Geophys. Res. 107, 2212.

Tichelaar, B.W., Ruff, L.J., 1989. How good are our best models?; jackknifing, bootstrapping, and earthquake depth. Eos. Trans. AGU 70, 593-593.

Tsai, V.C., Hayes, G.P., Duputel, Z., 2011. Constraints on the long-period moment-dip tradeoff for the Tohoku earthquake. Geophys. Res. Lett. 38, L00G17.

Tsuji, T., Ito, Y., Kido, M., Osada, Y., Fujimoto, H., Ashi, J., Kinoshita, M., Matsuoka, T., 2011. Potential tsunamigenic faults of the 2011 off the Pacific coast of Tohoku Earthquake. Earth Planets Space 63, 831-834.

Tsuru, T., J.-O. Park, N. Takahashi, S. Kodaira, Y. Kido, Y. Kaneda, and Y. Kono, 2000, Tectonic features of the Japan Trench convergent margin off Sanriku, northeastern Japan, revealed by multichannel seismic reflection data, J. Geophys. Res., 105(B7), 16,403–16, 413.

Usami, T., 1966. Descriptive table of major earthquakes in and near Japan which were accompanied by damages. Bull. Earthquake Res. Inst., Tokyo Univ 44, 1571-1622.

Von Huene, R., Culotta, R., 1989. Tectonic erosion at the front of the Japan Trench convergent margin. In: J.P. Cadet and S. Uyeda (Editors), Subduction Zones: the Kaiko Project. Tectonophysics, 160: 75-90.

Wang, K., Bilek, S.L., 2011. Do subducting seamounts generate or stop large earthquakes? Geology 39, 819.

Wang, K., Hu, Y., 2006. Accretionary prisms in subduction earthquake cycles: The theory of dynamic Coulomb wedge. J. Geophys. Res. 111, B06410.

Wang, K., Suyehiro, K., 1999. How does plate coupling affect crustal stresses in Northeast and Southwest Japan. Geophys. Res. Lett. 26, 2307-2310.

Wei, S., Graves, R., Helmberger, D.V., Avouac, J.-P., Jiang, J., 2012. Sources of shaking and flooding during the Tohoku-Oki earthquake: A mixture of rupture styles. Earth Planet. Sci. Lett. Volumes 333–334, Pages 91–100.

Wu, W., Ni, S., Zhan, Z., A three-dimensional hybrid method for modeling teleseismic body waves with complicated source-side structure. In preparation.

Ye, L., Lay, T., Kanamori, H., 2012. Ground shaking and seismic source spectra for large earthquakes around the megathrust fault offshore of Northeastern Honshu, Japan. Bull. Seismol. Soc. Am., 103(2B), 1221-1241.

Zhao, D., Huang, Z., Umino, N., Hasegawa, A., Kanamori, H., 2011. Structural heterogeneity in the megathrust zone and mechanism of the 2011 Tohoku-oki earthquake (Mw 9.0). Geophys. Res. Lett. 38, L17308.

# Chapter 7

# Rupture complexity of the Great 1994 Bolivia and 2013 Sea of Okhotsk deep earthquakes

## 7.1 Abstract

The physical mechanism of deep earthquakes (depth>300km) remains enigmatic (Green and Houston, 1995; Houston, 2007; Kirby et al., 1996), partly because their rupture dimensions are difficult to estimate due to their low aftershock productivity (Frohlich, 1989) and absence of geodetic or surface rupture observations. The two largest deep earthquakes, the recent Great 2013 Sea of Okhotsk earthquake (M8.3) and the Great 1994 Bolivia earthquake (M8.3) (Kanamori et al., 1998; Kikuchi and Kanamori, 1994), together provide a unique opportunity to compare their rupture patterns in detail. Here we extend a travel-time sub-event location method (Duputel et al., 2012; Kikuchi and Kanamori, 1991; Tsai et al., 2005) to perform full teleseismic P-waveform inversion. This new method allows us to explain the observed broadband records with a set of sub-events whose model parameters are robustly constrained without smoothing. We find that while the Okhotsk event is mostly unilateral, rupturing 90km along strike with a velocity over 4km/s, the Bolivia earthquake ruptured about half this distance at a slow velocity (about 1.5 km/s) and displayed

a major change in rupture direction. We explain the observed differences between the two earthquakes as resulting from two fundamentally different faulting mechanisms in slabs with different thermal states. Phase transformational faulting (Green II and Burnley, 1989; Kirby et al., 1991) is inferred to occur inside the metastable olivine wedge within cold slab cores whereas shear melting (Griggs and Baker, 1969; Kanamori et al., 1998; Karato et al., 2001; Ogawa, 1987) occurs inside warm slabs once triggered.

## 7.2 Introduction

Several mechanisms for deep earthquakes have been proposed, including thermal shear instability (Griggs and Baker, 1969; Kanamori et al., 1998; Karato et al., 2001; Ogawa, 1987), dehydration embrittlement of pre-existing faults (Meade and Jeanloz, 1991; Silver et al., 1995), and transformational faulting associated with a metastable olivine wedge in cold subducting slabs (Green and Houston, 1995; Green II and Burnley, 1989; Kirby et al., 1991; Kirby et al., 1996). These mechanisms have been previously evaluated using deep earthquake rupture properties (e.g., duration, rupture dimension, rupture speed, stress drop, and radiation efficiency) (Suzuki and Yagi, 2011; Tibi et al., 2003; Wiens, 2001), aftershock statistics (Houston, 2007; Wiens, 2001), and their depth dependence (Persh and Houston, 2004a, b; Tocheport et al., 2007). Among these mechanisms, phase transformational faulting and thermal shear instability, possibly involving melting, have so far garnered the most evidence (Houston, 2007; Wiens, 2001). It has also been suggested that deep earthquake mechanisms may depend on the thermal state of the subducting slab (Houston, 2007; Tibi et al., 2003; Wiens, 2001; Wiens and Gilbert, 1996; Wiens and McGuire, 1995), but evidence has been inconclusive (Suzuki and Yagi, 2011).

The 1994 Bolivia earthquake was the largest deep earthquake until the recent

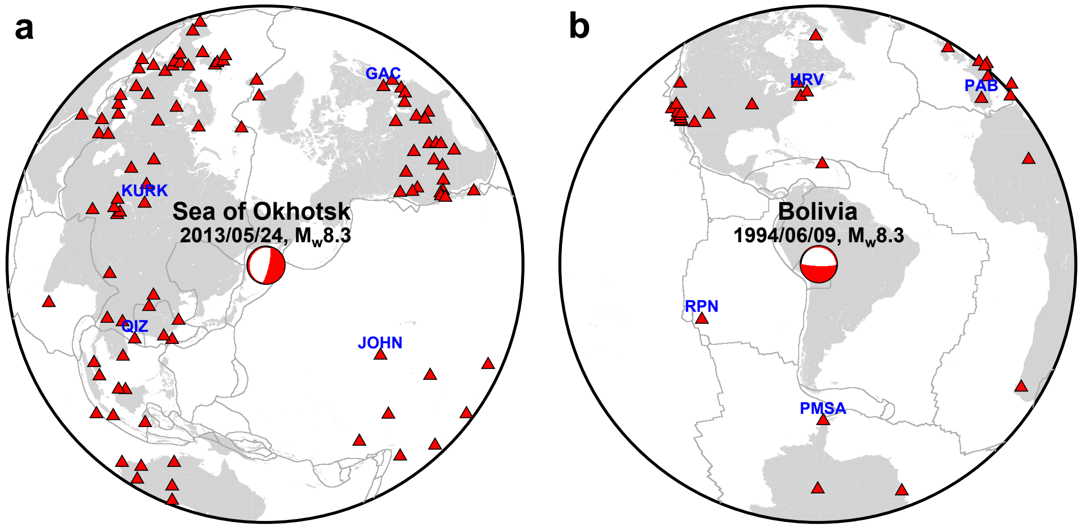


Figure 7.1: Teleseismic stations used to study (a) the 2013/05/24 Mw 8.3 Okhotsk earthquake, and (b) the 1994/06/09 Mw 8.3 Bolivia earthquake.

2013 Okhotsk earthquake of similar magnitude (Figure 7.1), and has provided critical information about deep earthquake mechanisms. The earthquake was previously characterized by low rupture speed (~1.5km/s), high static stress drop, and low radiation efficiency (Ihmlé, 1998; Kikuchi and Kanamori, 1994; Silver et al., 1995). The earthquake's rupture dimension (~30kmx40km) is small for its size, yet significantly larger than the predicted width of the metastable olivine wedge (Tibi et al., 2003), unless significant thickening of the slab occurs due to plate bending (Kirby et al., 1995). Kanamori et al. suggest instead that shear melting could have promoted extensive sliding with high energy dissipation which resulted in large slip, high stress drop and slow rupture speed (Kanamori et al., 1998).

The 2013 Okhotsk deep earthquake was of similar size as the Bolivia earthquake, but occurred in a different tectonic setting. The subducted Pacific plate in which the Okhotsk earthquake occurred is significantly older and hence colder than the subducted Nazca plate in which the Bolivia earthquake occurred (Wiens and Gilbert, 1996). A thorough comparison of these two earthquakes' rupture properties thus provides important constraints on the faulting mechanism of deep earthquakes and its temperature dependence.

## 7.3 Directivity analysis

Earthquake source dimension and rupture directivity directly affect the azimuth and distance dependence of waveforms. This directivity effect is easily quantified for an earthquake that consists of a few sub-events. For the $n$-th sub-event at time $T_n$ with distance $L_n$ from the hypocenter, the timing of the observed displacement pulse at any station $i$ can be written as

$$T_n^i = T_n - \frac{L_n}{c_P^i} \cos(\theta_i - \theta_r^n),$$

where $\theta_i$ is the station azimuth, $\theta_r^n$ is the rupture direction, and$c_P^i$ is the phase velocity of teleseismic $P$ waves (which depends on station distance). Defining a directivity parameter following Ammon et al. (2005), $x_i = -\frac{\cos(\theta_i - \theta_r^n)}{c_P^i}$, then $T_n^i = T_n + L_n \cdot x_i$. Therefore, arranging teleseismic $P$ waves by directivity parameter $x_i(\theta_r^n)$, different sub-events can be identified as different straight lines with slopes of $L_n$ and zero-crossing points at $T_n$. The choice of rupture direction $\theta_r^n$ is based on trial and error, and could be different for different sub-events.

Figure 7.1 shows the teleseismic stations that we use for analysis of the 1994 Bolivia earthquake and the 2013 Okhotsk earthquake. We choose stations based on data quality and azimuthal coverage, and remove near-nodal stations to avoid complicated waveforms due to 3D structure. The qualitative rupture properties of a seismic event can be inferred by making the directivity plots (Silver et al., 1995). As mentioned above, arrivals from different earthquake sub-events will be aligned with different linear moveouts if the sub-events occur in the assumed rupture direction. Teleseismic

P waveforms for the Okhotsk earthquake (Figure 7.2a) show strong directivity to the NNW and SSE (N165°E), with a few major sub-events clearly visible in the directivity plot. Unlike for the Okhotsk earthquake, waveforms of the Bolivia earthquake cannot be aligned well with a single rupture direction, and require two rupture stages (Figure 7.2b, c). In stage 1, the Bolivia earthquake ruptured to the east with a series of small sub-events, whereas in stage 2 the rupture grew rapidly and the last sub-event arrival is better fit with rupture to the NE.

## 7.4 Subevent modeling

While the essential features of both the Okhotsk and Bolivia earthquakes are easily visualized in the directivity plots of Figure 7.2, quantitative details regarding the precise locations and timings of the sub-events cannot be determined from visual inspection. We therefore introduce a new sub-event algorithm to simultaneously invert broadband P waveforms for multiple sub-events' centroid locations, centroid times and moments. As with other sub-event methods (Duputel et al., 2012; Kikuchi and Kanamori, 1991; Tsai et al., 2005), we use only a small number of sub-events with a correspondingly small number of free parameters; yet our method can explain the observed broadband data with sufficient detail and estimate the moment distribution. Due to the small number of parameters estimated, our sub-event inversion does not require damping, smoothing or constraints on rupture velocity. Our method also uses global broadband data, rather than the regional high-frequency data of back-projection methods (Ishii et al., 2005), and therefore resolves the broadband slip distribution.

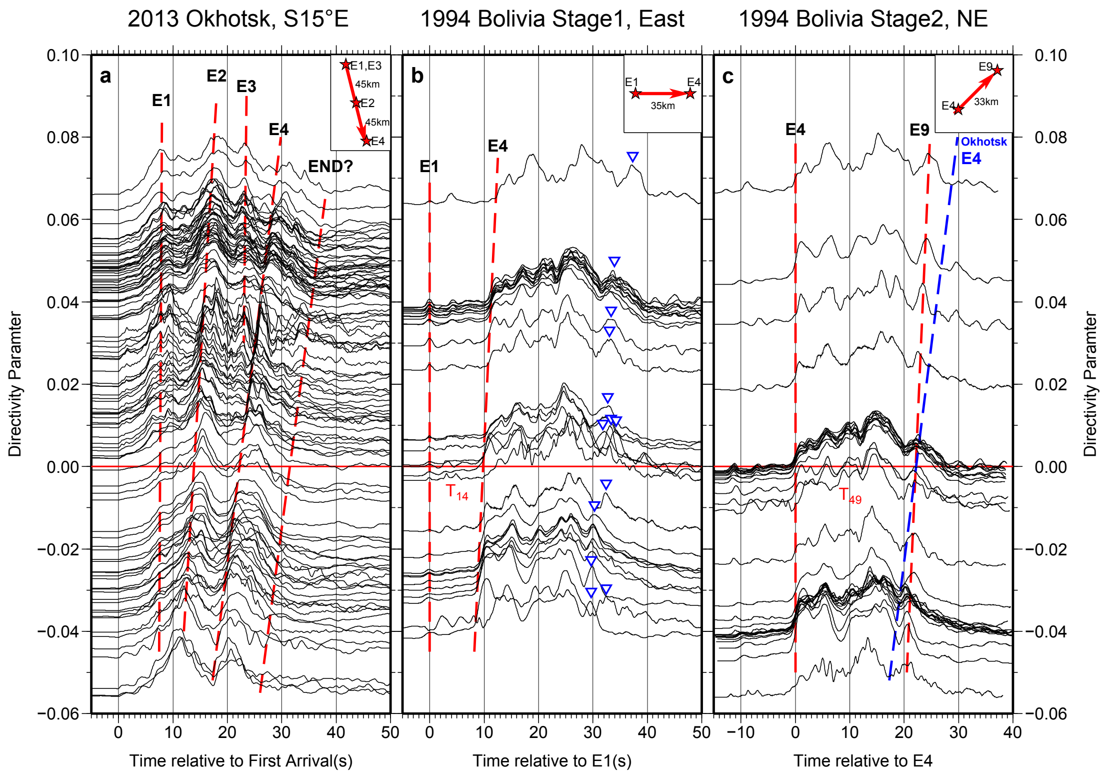


Figure 7.2: Rupture Directivity. Directivity plots for the broadband teleseismic P waves from the Okhotsk and Bolivia earthquakes. Since we do not invert for focal mechanisms here, we flip the P-wave polarities to be positive only, while keeping the true amplitudes. (a) Teleseismic P waves from the Okhotsk earthquake arranged by directivity parameter, assuming rupture direction towards S15°E and aligned by hand-picked first arrivals. We identify four major sub-events (E1, E2, E3 and E4) and the approximate end (END) marked by the red dashed lines, whose slopes are controlled by their distances from the epicenter. The times of the dashed lines at directivity parameter 0.00 identify the times of the sub-events from the earthquake origin time. The inset shows the approximate relative locations of E1, E2, E3 and E4. (b) Similar to (a) but for the Bolivia earthquake stage 1, assuming rupture direction to the East. Due to the non-emergent first arrivals, the waveforms are aligned by the first sub-event E1. Sub-event E4 denotes the sharp rise of P wave amplitudes, is well aligned, and its time from E1 is denoted as T14. The blue inverted triangles show that arrivals from the last major sub-event E9 are not well aligned by directivity to the east. (c) Similar to (b) but for the Bolivia earthquake stage 2, assuming rupture to the North-East. The P waveforms are aligned by sub-event E4. The last major sub-event E9 is delayed by T49 relative to E4, and is marked by a red dashed line. For comparison, the Okhotsk sub-event E4 from panel (a) is shown as a blue dashed line. The similar timing but steeper slope of the Bolivia E9 compared to the Okhotsk E4 suggests that the Bolivia earthquake has smaller rupture dimension and lower average speed than the Okhotsk earthquake.

### 7.4.1 Methods

This new algorithm is based on previous travel-time sub-event modeling (Duputel et al., 2012; Kikuchi and Kanamori, 1991; Tsai et al., 2005), but does not require the subjective hand picking of coherent arrivals. Given a set of sub-event locations and times, we first predict the sub-event arrival times for each station. We then assume Gaussian-shaped source-time-functions centered at the predicted arrival times and invert the waveform data for the best fitting durations and amplitudes for each station independently to accommodate radiation patterns, path and site effects. Sub-event amplitudes and durations are assumed to be the average of the individual station amplitudes and durations, respectively. We use an iterative nonlinear least squares algorithm similar to Tsai et al. (2005) (Tsai et al., 2005) to iteratively update the sub-event locations and times by minimizing waveform misfit. The procedure requires initial guesses for sub-event model parameters, and we use our visually-determined results for both the Okhotsk and Bolivia earthquakes (plus published results for the Bolivia earthquake (Ihmlé, 1998; Kikuchi and Kanamori, 1994; Silver et al., 1995)), so that convergence is reached within 20 iterations. The choice of starting points and the number of sub-events can be adjusted based on waveform misfit and directivity analysis. Note that in this paper we assume that all sub-events occurred at the same depth. However, possibly different depths of sub-events will only bias the timing of the sub-events, but not the sub-event locations because of different azimuthal dependences.

### 7.4.2 Results

Figure 7.3a, 7.3b and Table 7.1a, 7.1b describe the final sub-event models for the Okhotsk and Bolivia earthquakes, respectively, where sub-event moments are assumed to be proportional to the average observed P-wave amplitudes. Waveforms are generally well fit (Figure 7.3c, 7.3d and Figure 7.4) and the sub-event models confirm the first-order features revealed by the directivity analysis. The Okhotsk earthquake first ruptured sub-event E1 slightly to the NE of the epicenter at about 8s, then proceeded to the south and ruptured its biggest sub-event E2. Perhaps due to the large slip, the rupture reset to propagate both north and south, generating E3 back near the epicenter (between E1 and E2) and E4 to the south. Finally, the rupture ended towards E4 at about 30s (see Figure 7.3a and 7.2a). The overall rupture was about 90km long, and was aligned roughly with the N-axis of the Okhotsk earthquake's GCMT focal mechanism (Ekström et al., 2012) as well as being fairly close to the slab strike from Slab 1.0 (Hayes et al., 2012) (dashed lines in Figure 7.3a) considering the uncertainties in Slab 1.0. The Bolivia earthquake started with a 10s-long weak but fast (3.5km/s) eastward rupture and generated three small sub-events (E1, E2 and E3) and a large sub-event E4 (stage 1). In stage 1, the rupture was approximately aligned with the N-axis of the Bolivia earthquake's GCMT focal mechanism (Ekström et al., 2012) and the slab strike from Slab 1.0 (Hayes et al., 2012) (dashed lines in Figure 7.3b). Similar to what happened after E2 of the Okhotsk earthquake, after E4, the Bolivia rupture also reset and changed rupture direction. However, rather than continuing along the slab strike, the rupture went to the North and NNW with E5, E6, E7, E8 and to the NE with E9. This stage is when most of the slip occurred. This main rupture area was about 30km$\times$40km, and lasted about 22s, characterizing a slow rupture speed of about 1.5km/s. In short, although the Bolivia earthquake and the Okhotsk earthquake have similar depths and moments, they have significantly different rupture processes and geometries. We find that the Okhotsk earthquake is twice as long and has rupture speed twice as high as the Bolivia earthquake. This implies that the Okhotsk earthquake has significantly lower static stress drop and higher radiation efficiency than the Bolivia earthquake. The two earthquakes' major ruptures also have different orientations with respect to the N-axes of the focal mech-

Table 7.1: Sub-event models

(a) Sub-event model of the 2013 Okhotsk earthquake

| | Times (s) | Longitude (°) | Latitude (°) | Mw |
|---|---|---|---|---|
| I1 | 1.33 | 153.278 | 54.877 | 7.10 |
| E1 | 8.94 | 153.347 | 54.898 | 7.95 |
| E2 | 15.30 | 153.507 | 54.475 | 8.13 |
| E3 | 22.95 | 153.471 | 54.823 | 7.88 |
| E4 | 24.23 | 153.653 | 54.160 | 7.95 |
| E4 | 32.27 | 153.656 | 54.135 | 7.42 |

(b) Sub-event model of the 1994 Bolivia earthquake

| | Times (s) | Longitude (°) | Latitude (°) | Mw |
|---|---|---|---|---|
| E1 | 0.04 | -67.561 | -13.845 | 7.18 |
| E2 | 3.34 | -67.425 | -13.880 | 7.14 |
| E3 | 6.55 | -67.416 | -13.849 | 7.24 |
| E4 | 11.77 | -67.227 | -13.884 | 7.71 |
| E5 | 15.96 | -67.208 | -13.840 | 7.81 |
| E6 | 20.67 | -67.406 | -13.729 | 7.71 |
| E7 | 26.11 | -67.322 | -13.697 | 7.91 |
| E8 | 35.04 | -67.241 | -13.764 | 7.51 |
| E9 | 32.55 | -67.003 | -13.682 | 7.61 |

anisms and the local slab strikes. Additionally, both earthquakes show well-resolved dynamic rupture processes strongly affected by sub-events with large slip.

## 7.5 Discussion and conclusions

The new rupture models obtained here have significant implications for the mechanics of deep earthquakes. Previous studies (Tibi et al., 2003; Wiens, 2001), using sets of large deep earthquakes (M>7), have observed slow rupture velocities for events in warm subduction zones, such as the South American subduction zone, and fast rupture velocities in cold subduction zones like Tonga. Although speculative, it has been suggested that two fundamentally different faulting mechanisms might operate for deep earthquakes (Houston, 2007). For the two largest deep earthquakes studied

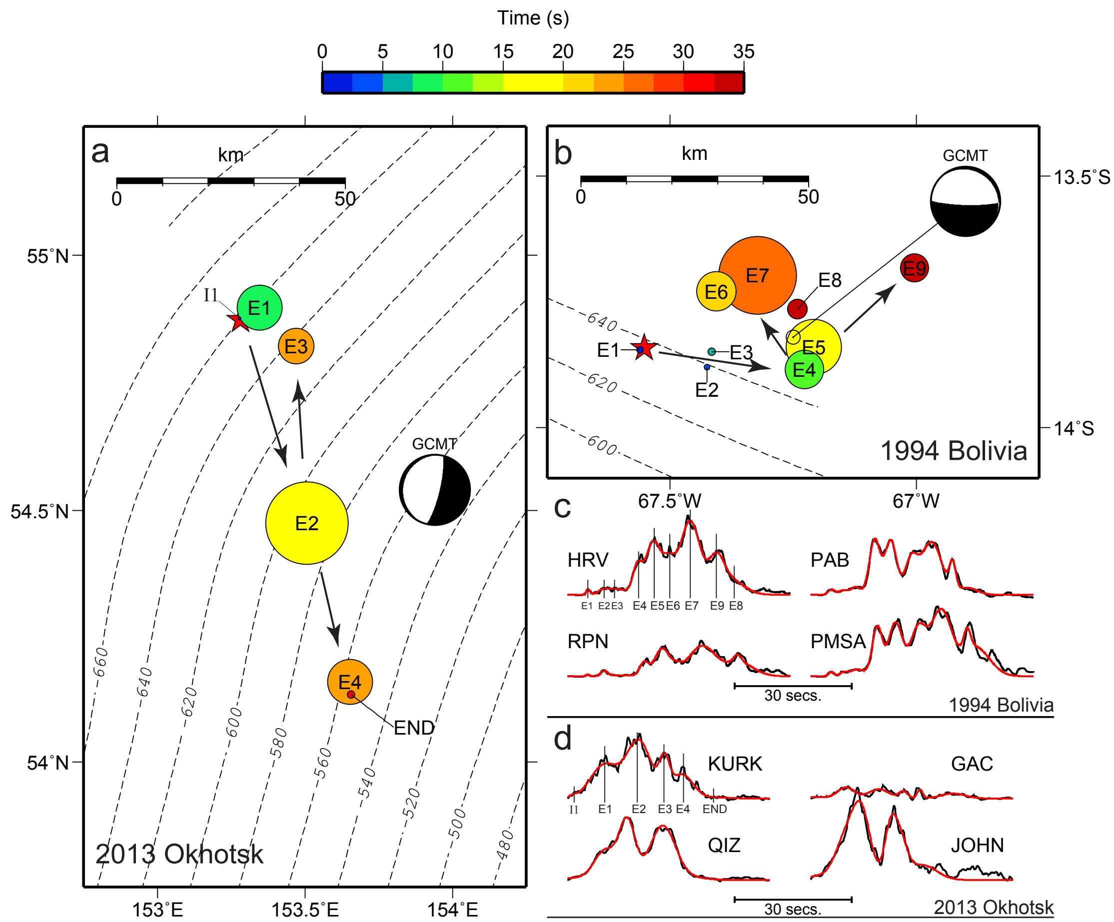


Figure 7.3: Sub-event models of the Okhotsk earthquake in (a) and of the Bolivia earthquake in (b). The red stars are the USGS NEIC epicenters, used as the reference starting points. Circles represent the earthquake sub-events with moments denoted by the sizes of the circles, and colors indicating sub-event centroid times. The black arrows illustrate the approximate rupture sequences. The slab depth contours from the Slab 1.0 model30 are shown as dashed lines. The N-axes of the Global CMT solutions of both earthquakes are approximately aligned with their respective slab strikes. (c) and (d) show example waveform fits for the sub-event models, for the Bolivia and Okhotsk earthquakes, respectively, with observed waveforms in black and predicted waveforms in red. The stations shown here are highlighted in Figure 7.1, and are representative of different azimuths. On the first example for each earthquake, the predicted arrival times of sub-events are marked by thin vertical lines. The complete waveform fits can be found in the supplementary material.

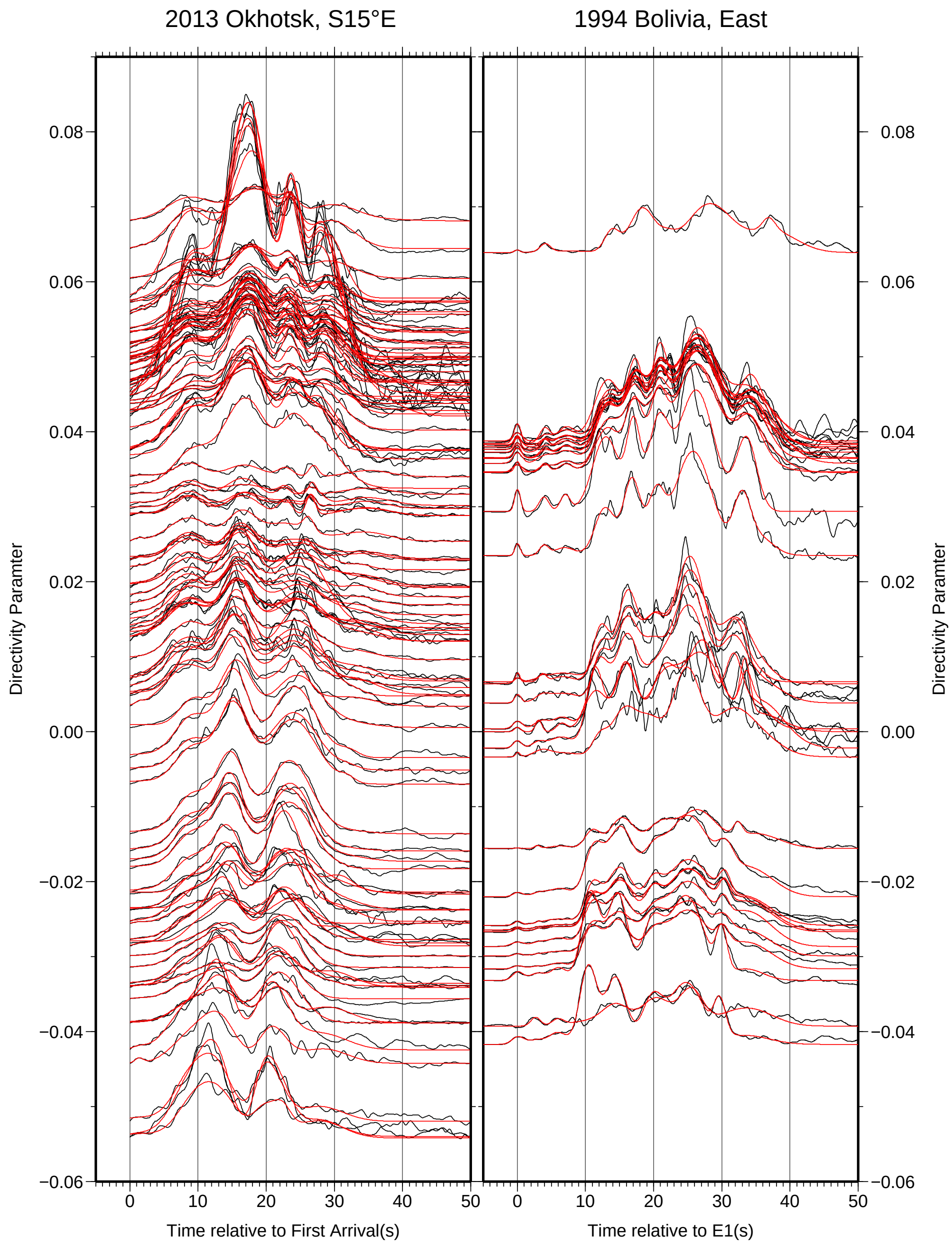


Figure 7.4: Waveform fits for the sub-event models of the 2013 Okhotsk earthquake and 1994 Bolivia earthquake. The data is plotted in black and the synthetics are plotted in red.

in this paper, the Bolivia earthquake occurred in the relatively warm South American subduction zone, whereas the Okhotsk earthquake occurred in the relatively cold Kuril subduction zone (Wiens and Gilbert, 1996). We find that they have significantly different source dimension, rupture speed, and orientation with respect to the slab strike, consistent with observations for other deep earthquakes (Tibi et al., 2003; Wiens, 2001), and resulting in different stress drops and radiation efficiencies. However, our sub-event analysis also shows that the first stage of the Bolivia earthquake, although weak, actually had a fast rupture speed, similar to the Okhotsk earthquake and other deep earthquakes in cold slabs. Furthermore, stage 1's rupture direction is also sub-parallel to the local strike of the slab, similar to the Okhotsk earthquake. From this, we infer that the Bolivia earthquake involved two different mechanisms in its two stages, with its first stage being similar to the Okhotsk earthquake except consisting of relatively small amplitude slip. Since the shear melting inferred during the Bolivia earthquake was mostly based on the major rupture parameters dominated by the area with large slip (Kanamori et al., 1998), it is reasonable to assume that the mechanism of stage 2 is shear instability caused by shear melting in a relatively warm slab.

Given our new results, we suggest a conceptual model to explain the different rupture processes of the Bolivia and Okhotsk earthquakes (Figure 7.5). Due to the difference in the thermal state of the subducting slabs responsible for the two earthquakes, the predicted widths of the metastable olivine wedges are also different. The Bolivia earthquake nucleated inside the relatively thin cold slab core by the transformational faulting mechanism (Green and Houston, 1995; Green II and Burnley, 1989; Kirby et al., 1991; Kirby et al., 1996), and ruptured inside the core along slab strike. Due to the small thickness of cold core, the rupture was relatively small but fast. However, after about 10s, the large sub-event E4 triggered shear melting, allowing the rupture to grow outside the metastable olivine wedge into the warmer slab

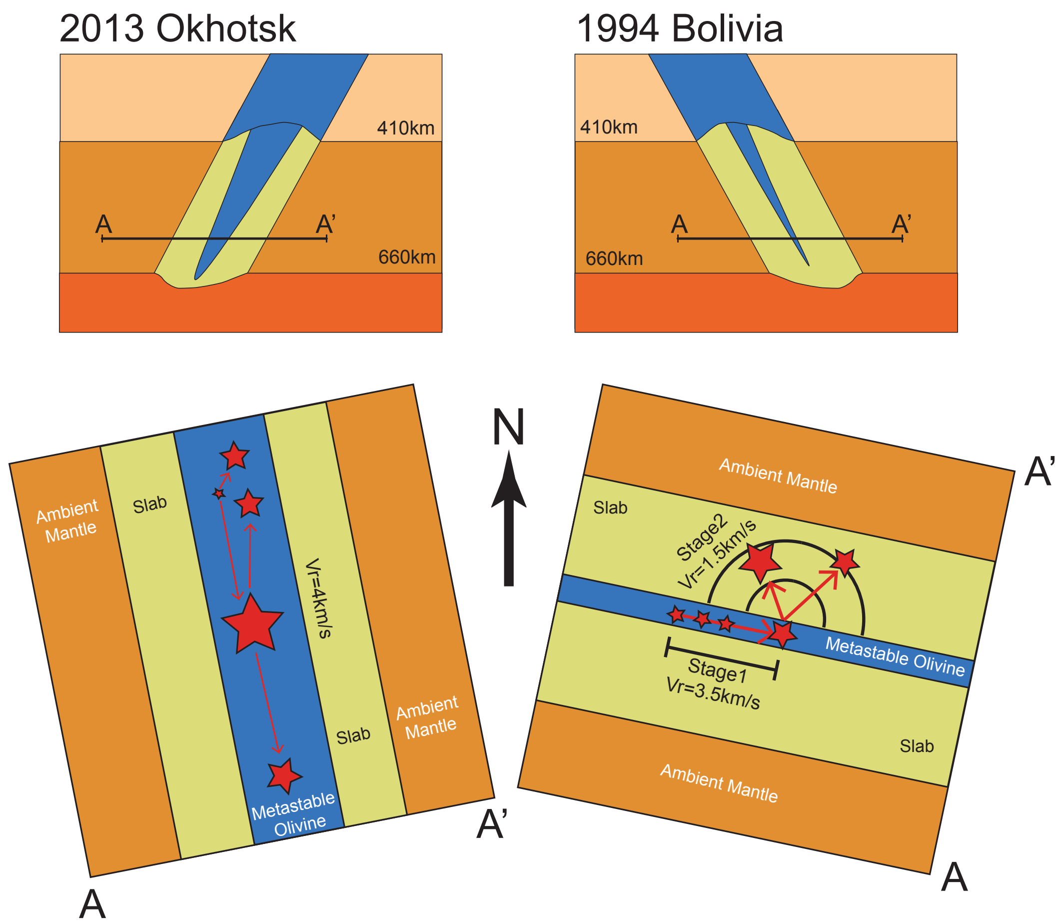


Figure 7.5: Conceptual models of the Okhotsk and Bolivia earthquakes in cross section (top panels) and map view (bottom panels). Due to differences in the thermal states of the subducting slabs in which the two earthquake occurred, the widths of the metastable olivine wedges in the slab core are also different. This causes different dominant faulting mechanisms for the two largest deep earthquakes. The Okhotsk earthquake is inferred to have ruptured mostly inside the relatively thick metastable olivine wedge, whereas the Bolivia earthquake's major rupture, stage 2, was outside the relatively thin metastable olivine wedge. See the main text for details.

material, where the melting point is reached more easily (Ogawa, 1987). The positive feedback during shear melting caused the slip to grow rapidly to cause a great earthquake. Due to the substantial energy dissipation involved with shear melting, the rupture speed in this stage decreased significantly. On the other hand, we propose that the recent Okhotsk earthquake nucleated and managed to stay inside the relatively wide metastable olivine wedge in a cold slab. Therefore, the rupture direction stayed close to the slab strike, and the rupture speed stayed relatively high. Interestingly, after the biggest sub-event E2, the rupture also seems to have reset and ruptured both northward and southward, similar to the Bolivia earthquake after its E4. This implies that very dynamic rupture processes occur during great deep earthquakes, despite inferred differences in the mechanisms. The results shown in this paper demonstrate the complexity of deep earthquakes, and the methodology described has the potential to reveal the mechanics of other earthquakes.

## References

Ammon, C.J., Ji, C., Thio, H.-K., Robinson, D., Ni, S., Hjorleifsdottir, V., Kanamori, H., Lay, T., Das, S., Helmberger, D., 2005. Rupture process of the 2004 Sumatra-Andaman earthquake. Science 308, 1133-1139.

Duputel, Z., Kanamori, H., Tsai, V.C., Rivera, L., Meng, L., Ampuero, J.-P., Stock, J.M., 2012. The 2012 Sumatra great earthquake sequence. Earth and Planetary Science Letters 351, 247-257.

Ekström, G., Nettles, M., Dziewoński, A., 2012. The global CMT project 2004–2010: Centroid-moment tensors for 13,017 earthquakes. Physics of the Earth and Planetary Interiors 200-201, 1-9.

Frohlich, C., 1989. The nature of deep-focus earthquakes. Annual Review of Earth and Planetary Sciences 17, 227.

Green, H.W., Houston, H., 1995. The mechanics of deep earthquakes. Annual Review of Earth and Planetary Sciences 23, 169-214.

Green II, H., Burnley, P., 1989. A new self-organizing mechanism for deep-focus earthquakes. Nature 341, 733-737.

Griggs, D., Baker, D., 1969. The origin of deep-focus earthquakes, in: Mark, H., Fernbach, S. (Eds.), Properties of Matter Under Unusual Conditions. Wiley, New York, pp. 23-42.

Hayes, G.P., Wald, D.J., Johnson, R.L., 2012. Slab1. 0: A three-dimensional model of global subduction zone geometries. Journal of Geophysical Research 117, B01302.

Houston, H., 2007. Deep earthquakes. Treatise on Geophysics, edited by G. Schubert, 321-350.

Ihmlé, P.F., 1998. On the interpretation of subevents in teleseismic waveforms: the 1994 Bolivia deep earthquake revisited. Journal of Geophysical Research 103, 17919-17932.

Ishii, M., Shearer, P.M., Houston, H., Vidale, J.E., 2005. Extent, duration and speed of the 2004 Sumatra–Andaman earthquake imaged by the Hi-Net array. Nature 435, 933-936.

Kanamori, H., Anderson, D.L., Heaton, T.H., 1998. Frictional melting during the rupture of the 1994 Bolivian earthquake. Science 279, 839-842.

Karato, S.-i., Riedel, M.R., Yuen, D.A., 2001. Rheological structure and deformation of subducted slabs in the mantle transition zone: implications for mantle circulation and deep earthquakes. Physics of the Earth and Planetary Interiors 127, 83-108.

Kikuchi, M., Kanamori, H., 1991. Inversion of complex body waves—III. Bulletin of the Seismological Society of America 81, 2335-2350.

Kikuchi, M., Kanamori, H., 1994. The mechanism of the deep Bolivia earthquake of June 9, 1994. Geophysical Research Letters 21, 2341-2344.

Kirby, S.H., Durham, W.B., Stern, L.A., 1991. Mantle Phase Changes and Deep-Earthquake Faulting in Subducting Lithosphere. Science 252, 216-225.

Kirby, S.H., Okal, E.A., Engdahl, E.R., 1995. The 9 June 94 Bolivian deep earthquake: An exceptional event in an extraordinary subduction zone. Geophysical Research Letters 22, 2233-2236.

Kirby, S.H., Stein, S., Okal, E.A., Rubie, D.C., 1996. Metastable mantle phase transformations and deep earthquakes in subducting oceanic lithosphere. Reviews of Geophysics 34, 261-306.

Meade, C., Jeanloz, R., 1991. Deep-focus earthquakes and recycling of water into the Earth's mantle. Science 252, 68-72.

Ogawa, M., 1987. Shear instability in a viscoelastic material as the cause of deep focus earthquakes. Journal of Geophysical Research 92, 13801-13810.

Persh, S.E., Houston, H., 2004a. Deep earthquake rupture histories determined by global stacking of broadband P waveforms. Journal of Geophysical Research 109, B04311.

Persh, S.E., Houston, H., 2004b. Strongly depth-dependent aftershock production in deep earthquakes. Bulletin of the Seismological Society of America 94, 1808-1816.

Silver, P.G., Beck, S.L., Wallace, T.C., Meade, C., Myers, S.C., James, D.E., Kuehnel, R., 1995. Rupture characteristics of the deep Bolivian earthquake of 9 June 1994 and the mechanism of deep-focus earthquakes. Science 268, 69-69.

Suzuki, M., Yagi, Y., 2011. Depth dependence of rupture velocity in deep earthquakes. Geophysical Research Letters 38, L05308.

Tibi, R., Bock, G., Wiens, D.A., 2003. Source characteristics of large deep earthquakes: Constraint on the faulting mechanism at great depths. Journal of Geophysical Research 108, 2091.

Tocheport, A., Rivera, L., Chevrot, S., 2007. A systematic study of source time functions and moment tensors of intermediate and deep earthquakes. Journal of Geophysical Research 112, B07311.

Tsai, V.C., Nettles, M., Ekström, G., Dziewonski, A.M., 2005. Multiple CMT source analysis of the 2004 Sumatra earthquake. Geophysical Research Letters 32, L17304.

Wiens, D.A., 2001. Seismological constraints on the mechanism of deep earthquakes: Temperature dependence of deep earthquake source properties. Physics of the Earth and Planetary Interiors 127, 145-163.

Wiens, D.A., Gilbert, H.J., 1996. Effect of slab temperature on deep-earthquake aftershock productivity and magnitude-frequency relations. Nature 384, 153-156.

Wiens, D.A., McGuire, J.J., 1995. The 1994 Bolivia and Tonga events: Fundamentally different types of deep earthquakes? Geophysical Research Letters 22, 2245-2248.

# Chapter 8

# Imaging subducted slab structure beneath the Sea of Okhotsk with teleseismic waveforms

## 8.1 Introduction

Seismic images have revealed a complicated fate of subducted slabs, including penetrating into the lower mantle, stagnating in the transition zone, flat subducting and tearing. Approaches to derive these slab images are based mostly on travel times, and have evolved in the last decades with increasing data sets and progress in methodology (see Lay (1994) for a review). In the 1960s and 70s, teleseismic P-wave travel-times from shallow nuclear explosions and earthquakes suggested the existence of subducted slabs as dipping high-velocity layers (e.g., Davies and Julian, 1972; Sleep, 1973). To test the hypothesis of whole-mantle convection, numerous studies applied the residual sphere method to teleseismic travel times from deep earthquakes, and found high-velocity (3-5%) slabs penetrating into the lower mantle in most of the west and northwest Pacific subduction zones (e.g., Jordan, 1977; Creager and Jordan, 1984, 1986; Fischer et al., 1988; Fischer et al., 1991). To avoid biases from lower-mantle and station-side structures (e.g., Zhou et al., 1990; Ding and Grand, 1994) applied the residual sphere method to differential travel times from shallow and deep earthquakes in the Kuril subduction zone. They reported high-velocity (~5%) slab in the upper mantle, but complicated structure in the lower mantle. From the 1990s, with increasing quantity and quality of seismic data, global and regional travel-time tomography has been providing increasingly detailed images of subducted slabs (e.g., Zhou, 1990; van der Hilst et al., 1991; Zhao et al., 1992; Li et al., 2008; Simmons et al., 2012). Tomography models show that subducted slabs could have complex morphology (e.g., flat subduction, tearing), and could penetrate into the lower mantle or become stagnant in the transition zone. However, resolution of tomography is limited by data coverage, damping and accuracy of earthquake locations. For example, in most tomography models, the velocity perturbations of slabs are on the order of 1%, much smaller than the earlier results (~5%) from travel-time modeling mentioned above or waveform modeling discussed in this paper.

Seismic waveforms have better sensitivities to velocity perturbations and sharpness than travel time alone. For example, Silver and Chan (1986) observed multipathing of teleseismic S waves from deep earthquakes beneath the Sea of Okhotsk, and explained them as evidence for slab extension in lower mantle. Using the Cagniard-de Hoop method, Mellman and Helmberger (1974) demonstrated that a thin high-velocity layer has similar effect as attenuation (elastic-wave tunneling effect). Vidale (1987) coupled 2D finite-difference method near the source with Kirchhoff method in the far field, and predicted waveform broadening at take-off angles sub-parallel with the slab. This broadening was confirmed latter by Cormier (1989) using the Gaussian beam theory. However, these predicted teleseismic waveform effects from earthquakes close to or within subducted slab have not been systematically tested due to the sparse global networks at that time (e.g., Vidale and Garcia-Gonzalez, 1988; Cormier, 1989). Furthermore, Beck and Lay (1986) and Cormier (1989) pointed out another major difficulty with teleseismic waveform modeling that other deep-mantle heterogeneities or station-side structures could cause similar waveform distortions as subducted slabs.

In this paper, we demonstrate that the difficulties with slab waveform modeling can be overcome given the much denser global network and the better numerical methods now available. In particular, with examples in the Kuril subduction zone, we find that the P wave velocity in the slab center is about 5% higher than the ambient mantle, and we also test the waveform sensitivity to slab sharpness and depth extension of subducted oceanic crust.

Before going to the details of our teleseismic waveform modeling, we wish to acknowledge that waveform modeling of slab has been performed in subduction zones with regional networks (e.g., Abers, 2000; Chen et al., 2007; Savage, 2012). For example, by modeling two deep earthquakes' up-going waveforms recorded by Hi-Net, Chen et al. (2007) refined the slab model beneath Japan with about 4.5% high-velocity in the slab, and an elongated strong low-velocity layer on top to large depth. However, for many subduction zones without dense regional networks (e.g., Kuril), the teleseismic waveform modeling is still sufficient to refine slab models.

In the following, we first introduce the waveform effects of a high-velocity slab using our 2D finite-difference method. Then, we analyze the teleseismic waveforms from two earthquakes in the Kuril subduction zone and invert for slab velocity perturbation and sharpness.

## 8.2 Waveform effects of a high-velocity slab

The waveform effects of a high-velocity slab have been studied by different methods. In this paper, we use an efficient GPU-based 2D finite-difference (FD) method to simulate the full global wavefield with a high-velocity slab (Li et al., 2013). It takes only about 30 minutes to simulate the teleseismic wavefield to 1 Hz with 2 GPUs. This fast speed allows the testing of many different kinds of slab models efficiently. In the following we will demonstrate slab's waveform effects with four examples of high-velocity slab within homogeneous background.

The first example model consists of a homogeneous background with Vp=8 km/s, and a 60 km thick, 500 km long slab (the black solid rectangle in Figure 8.1A) with uniform velocity perturbation of 3%. An isotropic explosion source is placed in the left end of the slab (the red star in Figure 8.1A). The snapshot of the velocity field shows distorted P waves along directions sub-parallel with the slab, outlined by the wedge between the two red lines. In the right panel of Figure 8.1A, we plot the synthetic P waveforms at a line of stations (small triangles in left panel of Figure 8.1A) and align them on the theoretical travel times without the high-velocity slab. Waves arriving before the theoretical travel times (filled with red) have been speed up by the slab, and display waveform complexities (double arrivals). The first arrivals travel along the slab, and the second broader arrivals diffract around the slab (Vidale, 1987). Based on geometrical ray theory, the angular range of distorted waveforms can be approximated by $\sin(\frac{\pi}{2} - \theta) \approx \frac{1}{1+\delta}$, where $\theta$ is the angle between the red lines and slab in Figure 8.1A, $\delta$ is the velocity perturbation of the slab. Therefore, larger velocity perturbation $\delta$ causes wider range of waveform distortion (large $\theta$ angle), which is confirmed by our second example in Figure 8.1B with increased slab velocity perturbation (6%). On the other hand, sharpness of slab controls the waveform shapes. In Figure 8.1C, we set a triangular velocity profile across the slab with the highest perturbation in the slab center (6%), and drops in constant gradient to the background velocity on both edges. The average velocity perturbation is 3%, similar to the first example in Figure 8.1A. The simulated waveforms display distortions within similar range as in Figure 8.1A, but are smoother without double pulses. This is because the waves traveling along or diffracted around the slab are not as distinct as in Figure 8.1A. In Figure 8.1D, slab with triangular velocity profile and 12% perturbation in the center produces smooth waveforms as in Figure 8.1C, but wide range of distortions as in Figure 8.1B due to the similar average perturbation.

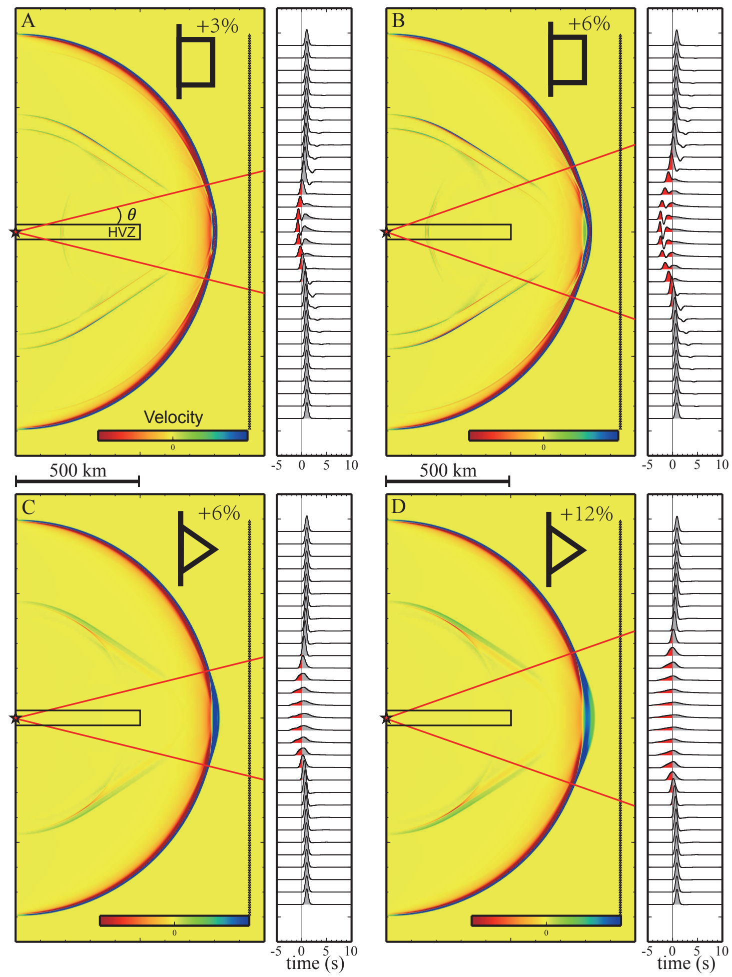


Figure 8.1: Examples of waveform complexity caused by a high-velocity slab. The finite-difference simulations of the full wavefield from an explosion source (star) at the left end of various high velocity slabs (black rectangle) are displayed assuming a grid-size of 1 km. In (A), the velocity profile across the slab is uniformly 3% higher than the homogeneous ambient material (Vp=8 km/s) as shown by the inset. The background shows a snapshot of the velocity wavefield with strong P waves and weak P-to-S converted phases from slab edges. The right panel displays the synthetic seismograms recorded on the linear array (small triangles) in the right part of the model. The seismograms are aligned by predicted travel times without the slab, and the earlier arrivals are filled by the red color. The wedge defined by the two red lines displays the range of stations with waveform distortions. (B) Similar to (A) but with a 6% uniform velocity perturbation within the slab. (C) Similar to (A) but with triangular velocity profile across the slab as shown by the inset. (D) Similar to (C) but with a 12% velocity perturbation in the slab core.

In summary, the four examples demonstrate consistent waveform effects of slab as in previous studies (e.g., Vidale, 1987). In particular, we find that slab sharpness and perturbation control the waveform shapes and the angular range of distortions, respectively. In the next section, we will present similar phenomena observed for earthquakes close to or within subducted slabs, and model slab velocity perturbations and sharpness.

## 8.3 Data

Our study region is the middle section of the Kuril subduction zone (Figure 8.2A). In this area, the relocated EHB catalog (Engdahl et al., 1998) shows that seismicity continues down to ~600 km depth, and has relatively little variation along strike (Figure 8.2B). Therefore, the slab structure is close to a 2D problem along the down-dip direction, suitable for 2D waveform modeling (thick black line in Figure 8.2A). We study two earthquakes (red beachballs in Figure 8.2A), one on each side of the Kuril trench. The 2009/09/10, Mw5.9 earthquake is a shallow-angle thrust event at a depth of 37 km located on the plate interface, while the 2007/01/13 Mw6.0 earthquake is a shallow outer-rise event. Both earthquakes have relatively simple source processes without obvious directivity. Figure 8.3A shows the teleseismic P wave record-section of the 2009 interplate earthquake within 45° of the downdip azimuth (315°), aligned by the hand-picked P onsets. While the P and sP pulses have durations of ~2s at distances larger than 65°, the waveforms are significantly broader at distances less than 65°. The transition from narrow to broad pulses occurs between 70° and 60°, which correspond to only a ~3° difference in the take-off angles. Therefore, the observed distance-dependence of waveforms is too sharp to be explained by any source directivity, but requires structural anomalies near the source or in the deep mantle. Station-side structures are less likely because stations with similar distances record

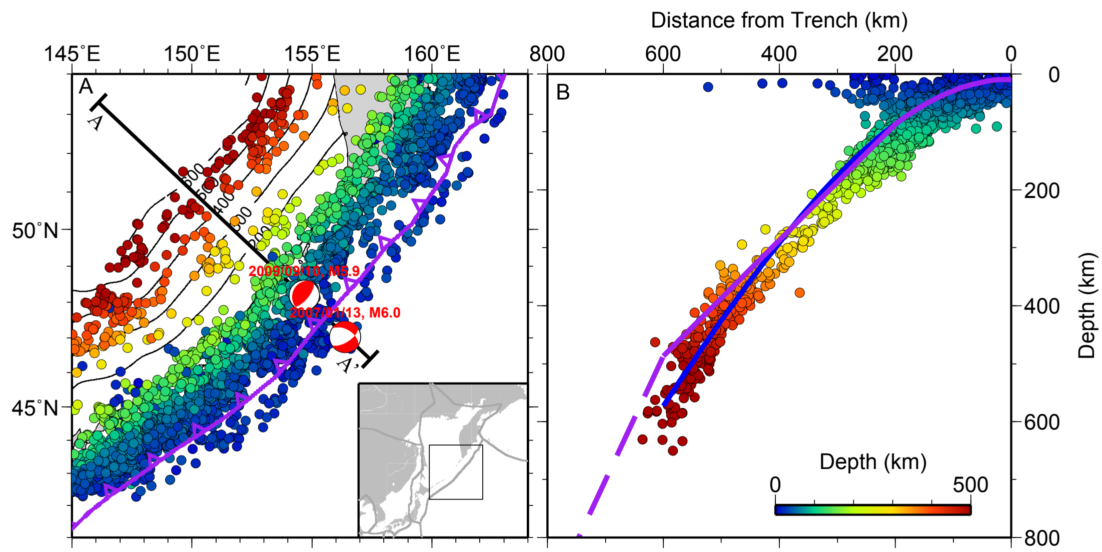


Figure 8.2: (A) Map and relocated seismicity of the Kuril subduction zone. Box in the inset shows the location of our study area. The dots are the earthquakes in the EHB catalog from 1961 to 2008, colored by their depths. The slab depth contours are from Slab 1.0 (Hayes et al., 2010). The two red beachballs show the two earthquakes studied in this paper, one on each side of the trench (purple barbed line). AA' displays the location of cross-sections in Figure 8.3. (B) Plot of seismicity versus distance from trench and depth. The thick blue line is the slab geometry from the Slab 1.0, while the purple line is the modified geometry used in this paper. The dashed purple line shows the lower mantle slab extension tested in this paper.

similar waveform broadenings even though they are far apart in locations. On contrary, similar P record-section for the nearby 2007 outer-rise earthquake (Figure 8.3B) does not show any waveform broadening, even though it samples almost the same lower-mantle and station-side structures. Therefore, we conclude that the observed waveform broadening of the 2009 earthquake is caused by near-source structures.

The major differences in the ray paths between the 2007 and the 2009 earthquakes are whether they sample the subducted slab. Here we use a slab geometry constrained by the relocated seismicity to illustrate this point. Hayes et al. (2012) obtained a smooth slab model for this region (Slab 1.0), as shown by the thick blue line in Figure 8.2B. Note that at depths larger than 400 km, the slab geometry fits through the middle of the deep seismicity. Since deep earthquakes occur in the cold core

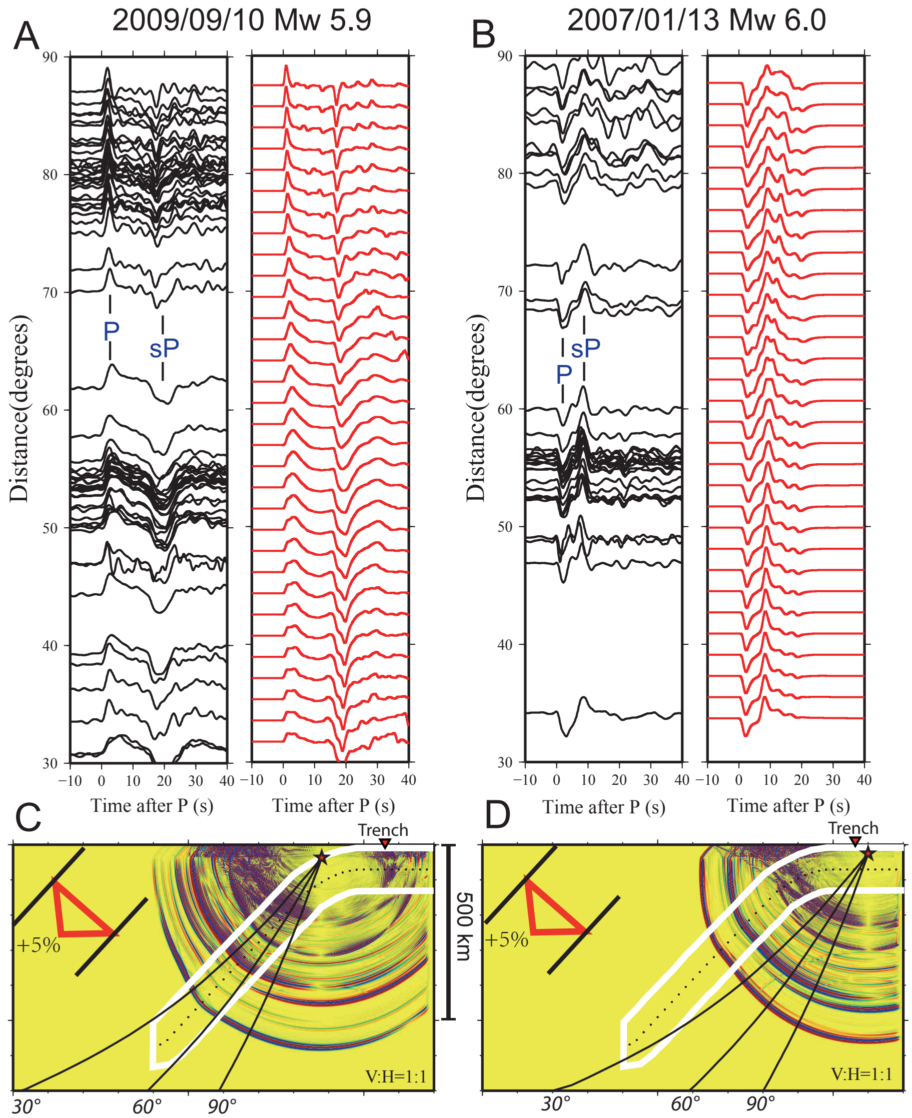


Figure 8.3: Waveform observations and simulations for the 2009/09/10 Mw5.9 interplate earthquake and the 2007/01/13 Mw6.0 outer-rise earthquake. (A) Distance record-sections of observed (left panel, black) and synthetic (right panel, red) seismograms for the 2009 interplate earthquake, aligned by the first P arrivals. (B) Similar to (A) but for the 2007 outer-rise earthquake. Figure 8.4 shows the comparisons of observed and synthetic full waveforms. (C) 2D finite-difference simulation of the 2009 interplate earthquake (red star) with a high-velocity slab (outlined by the white line). The inset shows the triangular velocity profile across the slab, with 5% perturbation in the slab center. Black lines display the P wave ray paths to teleseismic distances of 30°, 60° and 90°, respectively. (D) Similar to (C) but for the 2007 outer-rise earthquake.

of subducted slabs, we modify the slab geometry to fit the top of the seismicity (thick purple line in Figure 8.2B). Given the modified slab geometry, we outline the subducted slab as white lines in a vertical cross-section (Figure 8.3C and 8.3D) along line AA' in Figure 8.2A. As shown in Figure 8.3D, the 2007 outer-rise earthquake (red star) occurred to the east of the trench, and its teleseismic ray paths to 30°, 60° and 90° have little interaction with the subducted slab. In contrast, teleseismic ray paths of the 2009 interplate earthquake travel along the slab to 30° and 60°, but avoid the slab at larger ranges (90°) (Figure 8.3C). This dependence of slab sampling with take-off angles coincides with the observed distance-dependent waveform broadening, and is very similar to the synthetic examples shown in Figure 8.1. Therefore, we conclude that the observed waveform broadening of the 2009 earthquake is caused by the subducted slab structure. In the next section, we will invert the observed waveform broadening for slab perturbation and sharpness in the 2D vertical cross-section along line AA' in Figure 8.2A.

## 8.4 Slab velocity model

### 8.4.1 Velocity perturbation

The synthetic examples in Figure 8.1 demonstrate that velocity perturbation controls the transition from simple to distorted waveforms. Similarly, the observed transition around 65° for the 2009 interplate earthquake is also sensitive to slab velocity perturbations. Here we search for the best-fitting models by testing a variety of slab thickness-perturbation-sharpness combinations, using the fast GPU-based 2D FD method. We simulate the full global wavefield with PREM as the background model. Our preferred slab model has a triangular velocity profile across a 120km thick slab, with a maximum perturbation of 5% in the slab core (insets in Figure 8.3C and 8.3D). The velocity snapshots of the simulated wavefields (colored back-

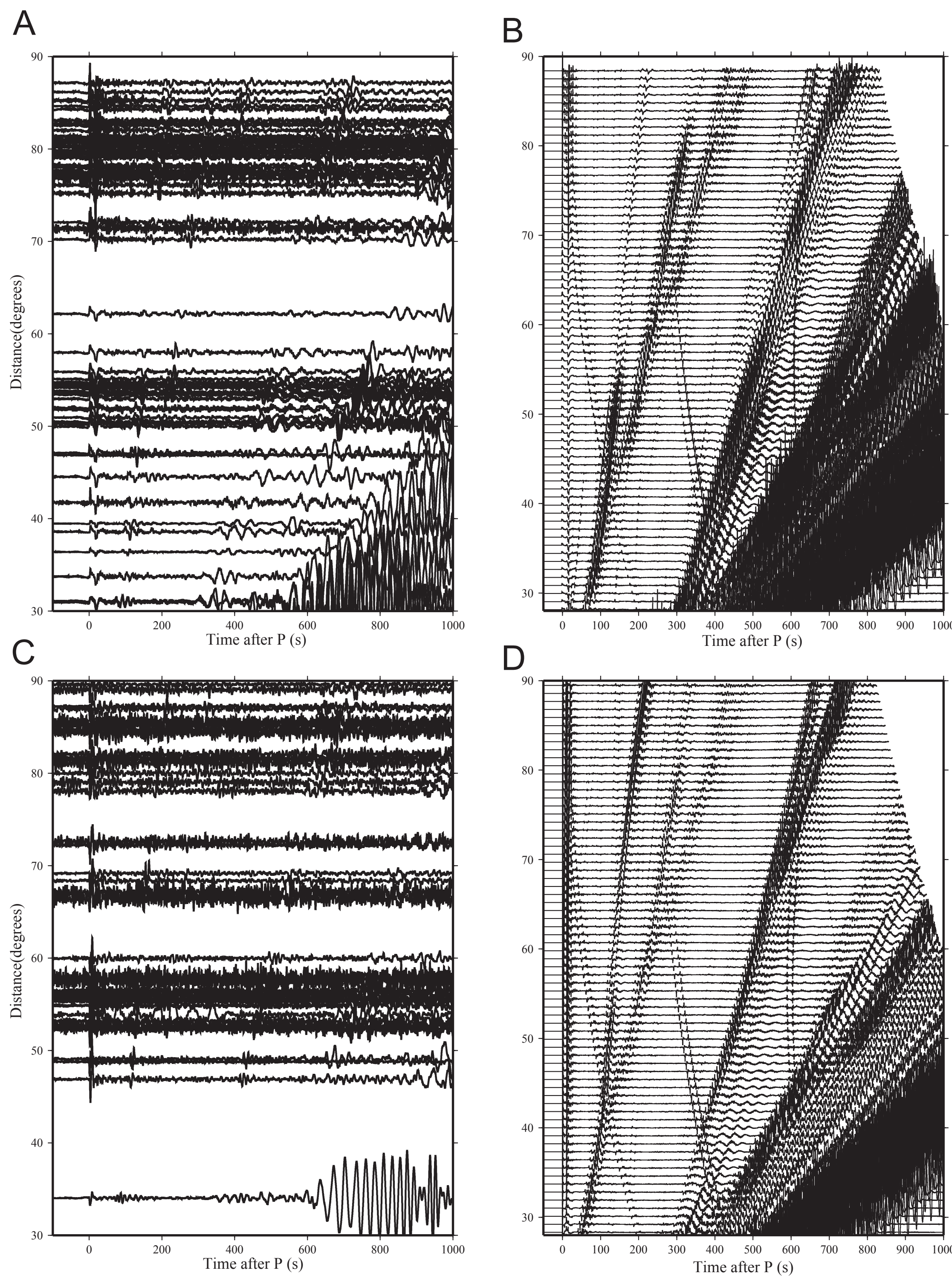


Figure 8.4: Complete record sections of the 2009 and 2007 earthquakes. (A) and (B) are the data and synthetics for the 2009 interplate earthquake, respectively. (C) and (D) are the data and synthetics for the 2007 outer-rise earthquake, respectively.

grounds in Figure 8.3C and 8.3D) show obvious speed-up of the wavefronts occurs along the slab. The synthetic seismograms for the 2009 interplate earthquake plotted side-by-side with the observations in Figure 8.3A reproduce the sharp transition from simple to broad waveforms between 70° and 60°. With the same slab model, the synthetics for the 2007 outer-rise event do not have any waveform distortion due to the slab, consistent with the observed waveforms (Figure 8.3B). Note that the 5% perturbation is significantly higher than previous travel-time tomography results for this region (~1%, e.g., Li et al., 2008; Simmons et al., 2012).

### 8.4.2 Slab sharpness

After explaining the transition from simple to broad waveforms around 65° distance, we turn to the waveform details to constrain the slab sharpness. As a reference, we show the waveform fitting for the preferred model with triangular velocity profile in Figure 8.5A. On tops of Figure 8.5B and 8.5C, we modify the velocity profile across the slab to have either sharp edges on both sides, or only sharp top but smooth bottom. The synthetic seismograms for each case are compared with the observations. In Figure 8.5B, the sharp edges on both sides produce distinct early arrivals (marked by the blue dashed line), which are not observed in real data. These distinct arrivals due to the sharp slab are similar to the double pulses in the synthetic examples in Figure 8.1A and 8.1B. The slab model with only sharp top (Figure 8.5C) provides similar waveform fitting as the preferred model, therefore we cannot distinguish the models in Figure 8.5A and 8.5C using the current dataset.

### 8.4.3 Low-velocity oceanic crust

How far does the low-velocity oceanic crust persist into the mantle is another major question for slab structures. As reviewed by Bostock (2012), the low-velocity zone (LVZ) starts to fade in seismic images between 40 km and 120 km, depending on

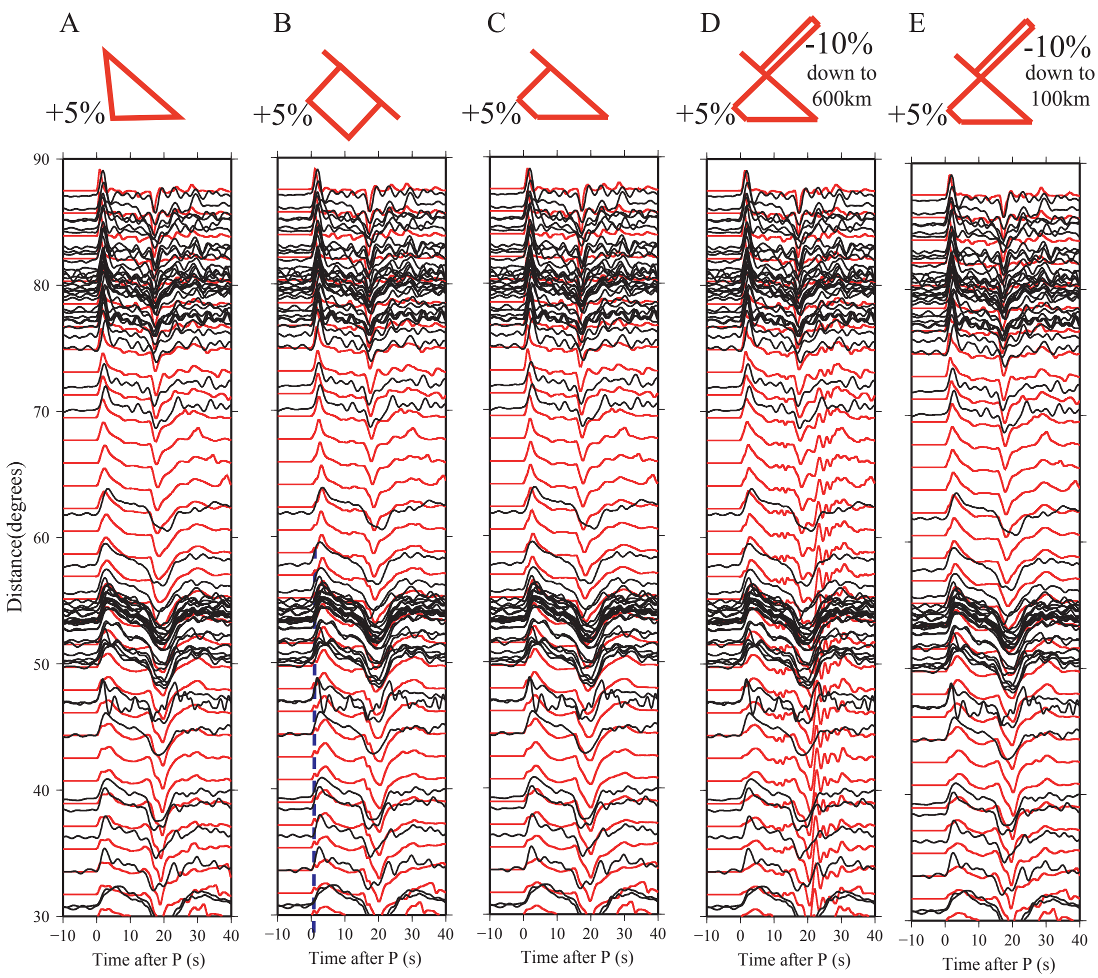


Figure 8.5: Tests of waveform sensitivities to slab sharpness. For each panel, the observed seismograms are shown as black, and the synthetics using different velocity profiles across the slab (displayed on top) are in red. (A) has smooth edge on each side, (B) has sharp edges on both sides, (C) has sharp top but smooth bottom. (D) and (E) are modified from (C) with a low-velocity layer on top, to 600 km and 100 km, respectively.

the thermal states. This fading is usually associated with the basalt-to-eclogite transition. However, there are also examples in which the LVZ persists to much larger depths (e.g., Abers, 2000; Chen et al., 2007). Here for the Kuril subduction zone, we test the teleseismic waveform sensitivity to the depth extent of LVZ using two end-member models, one with a 10 km thick, -10% LVZ down to 600 km depth, another with the same LVZ but only to 100 km depth, as shown in Figure 8.5D and 8.5E, respectively. In Figure 8.5D, the long LVZ serves as a strong wave-guide and produces strong high-frequency teleseismic coda waves in the synthetics, which are not observed in the real data. On contrary, the synthetics with LVZ down to 100 km fit the observations better (Figure 8.5E). Therefore, it is unlikely to have a coherent LVZ down to large depth beneath the Sea of Okhotsk, consistent with the basalt-to-eclogite transition. However, we cannot rule out a low-velocity layer to large depth with irregular geometries or strong scatterers inside to break the wave-guide effect (e.g., Savage, 2012).

### 8.4.4 Depth sensitivity and slab extension in the lower mantle

Due to limited depth resolution using only shallow earthquakes, in the models above we assume that the slab structure is uniform along the length direction and truncate the slab at depth of 600 km. However, we believe this approximation does not significantly affect the results in this paper because the thermally controlled velocity structure varies slowly along the slab. We also test models with high-velocity slab extension into the lower mantle (dashed purple line in Figure 8.2B) and find little difference in data fitting. Waveform modeling of earthquakes at different depths will provide better depth sensitivity to resolve any sharp velocity variations along the slab length direction due to phase changes. In particular, to separate the effects from the upper- and lower-mantle slab, we will need to model waveforms from deep earthquakes near the 660 km discontinuity. With the global full-wavefield simulation method, our waveform modeling approach applies to earthquakes at all depths.

## 8.5 Conclusion and future work

In this paper, we have studied the teleseismic P waveforms from two shallow earthquakes in the Kuril subduction zone to constrain the subducted slab structures. We observed strong distance-dependent waveform broadening and inverted for a high-velocity subducted slab with a triangular velocity profile. The maximum velocity perturbation in the slab core is 5%, significantly higher than most previous travel-time tomography models for this region (Li et al., 2008; Simmons et al., 2012), but consistent with earlier results from residual sphere method (Ding and Grand, 1994). We rule out slab models with both sharp top and bottom, suggesting that the slab structure is thermally controlled to the first order. The data also rejects a coherent low-velocity layer down to large depth, consistent with the model of basalt-to-eclogite transition at about 100 km depth (Bostock, 2012).

As pointed out by earlier investigators, teleseismic waveforms from subduction zone earthquakes have great potential in determining better images of subducted slabs, especially for areas without dense regional network. However, teleseismic waveform modeling has ambiguities with deep-mantle heterogeneities or station-side structures. In this paper, we have shown that we can overcome this ambiguity with the dense global seismic network and fast numerical methods. To resolve more details of slab structure, such as variations along the length direction and lower mantle slab extension, we need to include more earthquakes at different depths. Furthermore, since we use a full wavefield method, we can include many other teleseismic phases (e.g., PcP, PP, S, ScS, SS, see Figure 8.6) which have different sensitivities to the slab structures. 3D waveform modeling could incorporate more data off the downdip azimuth, but requires a lot more computational power in simulations of global wave-field to 1 Hz. One possible solution would be hybrid methods which couple expensive 3D methods near the source region and cheaper 1D approaches in the far field (e.g., Zhan et al., 2012).

# References

Abers, G.A., 2000. Hydrated subducted crust at 100-250 km depth. Earth Planet Sc Lett 176, 323-330.

Beck, S.L., Lay, T., 1986. Test of the Lower Mantle Slab Penetration Hypothesis Using Broad-Band S-Waves. Geophys Res Lett 13, 1007-1010.

Bostock, M., 2012. The Moho in subduction zones. Tectonophysics in press.

Chen, M., Tromp, J., Helmberger, D., Kanamori, H., 2007. Waveform modeling of the slab beneath Japan. Journal of Geophysical Research 112.

Cormier, V.F., 1989. Slab Diffraction of S-Waves. Journal of Geophysical Research 94, 3006-3024.

Creager, K.C., Jordan, T.H., 1984. Slab Penetration into the Lower Mantle. Journal of Geophysical Research 89, 3031-3049.

Creager, K.C., Jordan, T.H., 1986. Slab Penetration into the Lower Mantle beneath the Mariana and Other Island Arcs of the Northwest Pacific. Journal of Geophysical Research 91, 3573-&.

Davies, D., Julian, B.R., 1972. A Study of Short Period P-wave Signals from Long-shot. Geophysical Journal of the Royal Astronomical Society 29, 185-202.

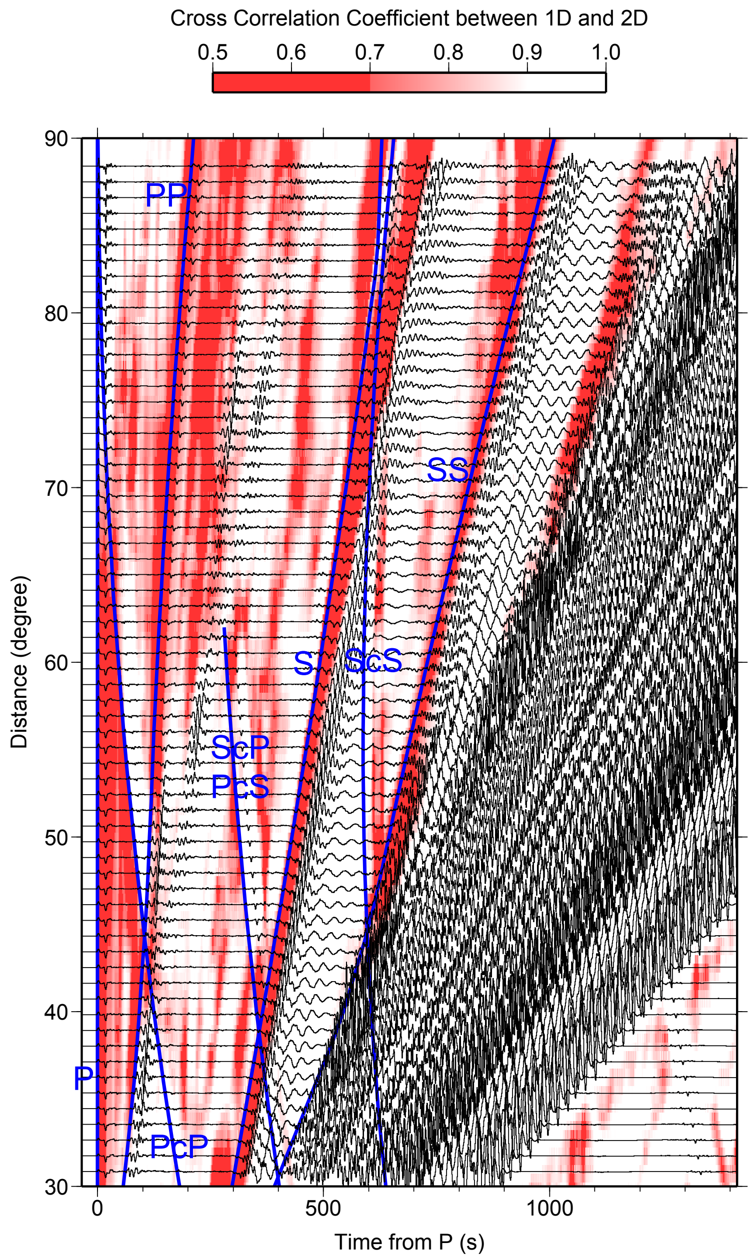


Figure 8.6: Complete synthetic record section of the 2009 earthquake with the preferred slab model. The blue lines mark the major teleseismic body wave phases. The wave packages with largest amplitudes are the surface waves. To high-light the effect of the subducted slab, we compare the synthetic seismograms from models with/without the slab by cross-correlation. The background color shows the maximum cross-correlation coefficients allowing 5s shift. High cross-correlation (>0.9, white) means little waveform effect from slab, and low cross-correlation (<0.7, red color) highlights strongly distorted waveforms. Note that the surface waves with large amplitudes are not affected by the slab structure.

Ding, X.Y., Grand, S.P., 1994. Seismic Structure of the Deep Kurile Subduction Zone. Journal of Geophysical Research 99, 23767-23786.

Engdahl, E.R., van der Hilst, R., Buland, R., 1998. Global teleseismic earthquake relocation with improved travel times and procedures for depth determination. B Seismol Soc Am 88, 722-743.

Fischer, K.M., Creager, K.C., Jordan, T.H., 1991. Mapping the Tonga Slab. Journal of Geophysical Research 96, 14403-14427.

Fischer, K.M., Jordan, T.H., Creager, K.C., 1988. Seismic Constraints on the Morphology of Deep Slabs. Journal of Geophysical Research 93, 4773-4783.

Hayes, G.P., Wald, D.J., Johnson, R.L., 2012. Slab1. 0: A three-dimensional model of global subduction zone geometries. Journal of Geophysical Research 117.

Jordan, T., 1977. Lithospheric slab penetration into the lower mantle beneath the Sea of Okhotsk. J. Geophys 43, l977.

Lay, T., 1994. The Fate of Descending Slabs. Annu Rev Earth Pl Sc 22, 33-61.

Li, C., van der Hilst, R.D., Engdahl, E.R., Burdick, S., 2008. A new global model for P wave speed variations in Earth's mantle. Geochemistry, Geophysics, Geosystems 9.

Li, D., Helmberger, D., Clayton, R., and Sun, D., 2013. Global synthetic seismograms using 2D Finite Difference, Geophysical Journal International, submitted.

Mellman, G.R., Helmberger, D.V., 1974. High-frequency attenuation by a thin high-velocity layer. B Seismol Soc Am 64, 1383-1388.

Savage, B., 2012. Seismic constraints on the water flux delivered to the deep Earth by subduction. Geology 40, 235-238.

Silver, P.G., Chan, W.W., 1986. Observations of body wave multipathing from broadband seismograms: Evidence for lower mantle slab penetration beneath the Sea of Okhotsk. Journal of Geophysical Research 91, 13787-13713,13802.

Simmons, N.A., Myers, S.C., Johannesson, G., Matzel, E., 2012. LLNL-G3Dv3: Global P wave tomography model for improved regional and teleseismic travel time prediction. Journal of Geophysical Research 117.

Sleep, N.H., 1973. Teleseismic P-Wave Transmission through Slabs. B Seismol Soc Am 63, 1349-1373.

van der Hilst, R., Engdahl, E., Spakman, W., Nolet, G., 1991. Tomographic imaging of subducted lithosphere below northwest Pacific island arcs. Nature 353, 37-42.

Vidale, J.E., 1987. Waveform effects of a high-velocity, subducted slab. Geophys Res Lett 14, 542-545.

Vidale, J.E., Garcia-Gonzalez, D., 1988. Seismic observation of a high-velocity slab 1200–1600 km in depth. Geophys Res Lett 15, 369-372.

Zhan, Z., Helmberger, D., Simons, M., Kanamori, H., Wu, W., Cubas, N., Duputel, Z., Chu, R., Tsai, V.C., Avouac, J.-P., 2012. Anomalously steep dips of earthquakes in the 2011 Tohoku-Oki source region and possible explanations. Earth Planet Sc Lett 353, 121-133.

Zhao, D.P., Hasegawa, A., Horiuchi, S., 1992. Tomographic Imaging of P-Wave and S-Wave Velocity Structure beneath Northeastern Japan. Journal of Geophysical Research 97, 19909-19928.

Zhou, H.-W., Anderson, D.L., Clayton, R.W., 1990. Modeling of residual spheres for subduction zone earthquakes: 1. Apparent slab penetration signatures in the NW

Pacific caused by deep diffuse mantle anomalies. Journal of Geophysical Research 95, 6799-6827.

Zhou, H.W., 1990. Mapping of P-Wave Slab Anomalies beneath the Tonga, Kermadec and New Hebrides Arcs. Phys Earth Planet In 61, 199-229.

# Chapter 9

# Conclusions

In this thesis, I present a wide range of studies in observational seismology. The results span interpretations of noise correlations in different environments, source parameters of intermediate to great earthquakes, and seismic velocity structure. Although the individual problems are relatively independent, the philosophy behind my approaches is to bring observational insights from seismic waveforms in critical and simple ways. The results can be summarized in the following.

In Part I, I first present two successful applications of the noise correlation method, in calibrating earthquake centroid and retrieving crustal body waves. I also present examples in which the noise correlations do not yield Green's functions, yet the results are still interesting and useful after case-by-case analyses. I use array technique to locate uneven distribution of noise sources and show their effects on weaker body-wave phases. I demonstrate that temporal variability of noise frequency content can cause spurious velocity changes when noise correlations are used to monitor velocity changes. For the Amery Ice Shelf, I find that the noise field is not diffuse, but dominated by energy trapped in a low velocity waveguide caused by the water layer below the ice. In summary, the noise correlation method, as a very useful tool in many cases, does not guarantee a correct or efficient interpretation of the noise data because it assumes a diffuse noise field. Thinking outside the box of retrieving Green's function from noise may be valuable for understanding ambient noise better.

In Part II, I present studies using earthquake waveforms to constrain earthquake source parameters and seismic velocity structure. This is the classical field of waveform seismology. By incorporating new dataset and improved methodologies, I am able to bring new information to the problems. I find that earthquakes in the Tohoku-Oki region have steeper dip angles than the previously imaged plate interface and explain this discrepancy as evidence for a complex plate interface. I obtain sub-event models for the two largest deep earthquakes, the Great 2013 Sea of Okhotsk earthquake and the Great 1994 Bolivia earthquake and attribute their differences to different slab thermal states. I model teleseismic waveforms from earthquakes in the Kuril subduction zone and obtain a ~5% velocity perturbation in the slab, significantly higher than most tomographic models. These results show the great vitality of the classical waveform modeling method.

Research usually brings forward more questions than answers. For example, what is next about ambient seismic noise? What can interplate earthquakes tell us about the plate boundaries and how are they related to great earthquakes? Can seismic waveforms finally resolve the problem of slab penetration into the lower mantle? What is the physical mechanism(s) of deep earthquakes? I do not have answers to these questions. However, I also have no doubt that seismograms will be a critical piece of the puzzle.